jpl

JET PROPULSION LABORATORY

CALIFORNIA INSTITUTE OF TECHNOLOGY

PASADENA, CALIFORNIA

.750-8

PHOTOHELIOGRAPH OPTICAL SYSTEM

August 12, 1968

Randolph A. Becker

Approved by:

J. Denton Allen, Task Leader,
Photoheliograph Task

JET PROPULSION LABORATORY
CALIFORNIA INSTITUTE OF TECHNOLOGY
PASADENA, CALIFORNIA

FOREWORD

This report covers work on one phase of the photoheliograph development task, NASA Code 945-84-00-01-00, for the period November 1967 through June 1968. The photoheliograph has been proposed to NASA for the Apollo telescope mount (ATM) by Caltech, with Professor Harold Zirin as the principal investigator and Dr. Robert Howard of Mt. Wilson and Palomar Observatories the co-investigator (see TM 33-369, November 1967). The objective of the investigation is to obtain high resolution cinematographs in white light near ultraviolet and narrow band hydrogen alpha. Because of the ATM program uncertainties, emphasis has been placed on areas of technology that are somewhat mission-independent, but the ATM spacecraft has been used to establish design constraints.

ACKNOWLEDGMENTS

The author wishes to express his appreciation to the following JPL personnel who have made vaulable contributions to this report:

C. J. Chocol	optical computer studies and optical consulting
R. F. Freeman	primary mirror materials study and OPD calculations
H. H. Mu	primary mirror distortion analysis
C. D. Porter	primary mirror thermal analysis
L. M. Rosenberg	alignment system
L. M. Snyder	optical filter study

CONTENTS

TABLES

ILLUSTRATIONS

ILLUSTRATIONS (contd)

ILLUSTRATIONS (contd)

ABSTRACT

A modified Gregorian optical design has been chosen for the ATM Photoheliograph on the basis of thermal considerations. The primary mirror clear aperture for the f/50 design is 65 cm. The secondary obscuration ratio is only 0.2 of the diameter. Assuming no surface or alignment errors, the telescope would give essentially diffraction-limited performance across the 3.2 arc-minute field. Coma and astigmatism across this small field of view are negligible. Alignment errors and surface errors are expected to reduce performance to a Strehl ratio of 0.8. In-orbit realignment of the optical system is mandatory; therefore, an alignment subsystem, capable of being operated while the telescope is observing the sun, has been designed as an integral part of the optical system. The telescope will utilize 3 recorders; a UV camera (1500-3000Å), a visible-light camera, and a hydrogen-alpha camera. A system resolution of approximately 0.2 arc seconds is expected at 5000 Angstroms. Lyot and Fabry-Perot filters have been investigated for the hydrogen-alpha camera. While the Lyot type filter possesses tunability, it is quite sensitive to thermal and vibration environments. The new, solid-type Fabry-Perot filters are very insensitive to the environment but, at present, are not obtainable with a tuning capability. The ultraviolet camera filter will probably be a metal-dielectric reflection-type interference filter unless a filter of somewhat broader band capability can be found.

CONCLUSIONS

The requirements of covering a very broad spectral range (1500-6600Å) and of folding a 32.5-meter focal length into a 3-meter telescope tube necessitate the use of a reflecting-type optical system for the ATM Photoheliograph. Since the total field of view is very small (3.2 arc minutes), the simple Cassegrain or Gregorian classical designs totally

satisfy the imaging requirements (i. e., the Seidel aberrations are negligible). Analysis of the Cassegrain design indicate acute thermal problems will occur at both the primary and secondary mirrors. A hybrid Cassegrain-Gregorian design will suffer from very high heating loads at the secondary mirror and an excessive secondary obscuration ratio. Through the use of a Gregorian design modified by placing a field stop at the prime focus, the major problems of the Cassegrain and the hybrid designs can be eliminated. This is possible by using the prime focus field stop to reflect out of the optical system nearly all of the non-image-forming solar flux — a significant amount since the final image comprises only one percent of the solar disk. The use of the prime focus heat stop introduces a requirement for the addition of two flat mirrors to the standard Gregorian design. These two flats form a "periscope" to bend the return beam from the secondary mirror around the field stop which, of course, obstructs the normal return beam path. The Gregorian focus is conveniently located near the rear of the telescope and outside the primary aperture.

Heat transfer restrictions imposed by the spacecraft design necessitate that the primary mirror be cooled rather than letting it come to equilibrium temperature under the one-solar-constant incident radiation. Studies have indicated the feasibility of extracting the heat from within the mirror itself through the use of internal cooling coils. This results in less thermal warpage of the mirror than if the heat is extracted from the back side. Two 26-inch diameter ultra-low-expansion fused silica primary mirror blanks with internal cooling channels are being ordered from Corning Glass Works. Interferometric testing of these mirrors in a thermal-vacuum chamber as they are irradiated with one solar constant will indicate the amount of warpage to be expected in earth-orbital flight and will serve as a check on the computer calculations on expected warpage.

Spectral intervals of interest for the solar telescope include ultraviolet in the 1500-3000Å wavelength region, white light centered at 5000Å and the hydrogen-alpha line at 6563Å. A system of beam splitters in the exit beam of the telescope will direct light simultaneously through separate filters to the appropriate cameras.

Commercial versions of the Lyot hydrogen-alpha filter are available from Zeiss and Bernhard Halle in Germany. Certain features such as electronic temperature control and shock mounted calcite crystals make the latter attractive for space flight application – although the useful shift range is only +1Å. Transmission of the Halle is 10-14% and, of the Zeiss, approximately 10%. The solid etalon Fabry-Perot filter is also being considered for isolation of the hydrogen-alpha line. It is relatively simple, very rugged and exhibits little drift with temperature. A commercially available Fabry-Perot filter developed by Perkin Elmer has a 0.55Å bandwidth with 88% transmission in an f/40 optical system. Certain modifications, however, must be added to provide for tunability.

Both transmitting and reflectance type interference filters have been investigated for the ultraviolet region. Several varieties of this type of filter have been described in the literature. W. G. Tifft at the University of Arizona has constructed a simple three-layer coating consisting of opaque aluminum, MgF_2 and semi-transparent aluminum. This produces a filter with high (80%) reflectivity bands centered at 1300 and 2600Å. They are approximately 250Å and 700Å wide respectively. Through the use of a thinner layer of MgF_2, it should be possible to shift the broader peak to a more applicable wavelength, say 1800Å.

The theoretical performance of the Gregorian telescope will be 0.19 arc seconds of resolution with no image motion and 0.22 arc seconds with the ATM specified jitter rate of

one arc-second/second (exposure time = 0.025 seconds). Surface errors of the mirrors will further degrade the performance of the optical system. This effect is particularly important since there are four mirrors in the image-forming portion of the telescope. However, two of these mirrors are small flats, and it is felt that the random surface errors of these flats can be held to perhaps a 1/100th wave thus opening up the tolerance on the random surface errors on the two curved mirrors (primary and secondary mirrors). The manufacturing tolerance systematic wavefront error of the optical system should be held to approximately 1/15th to 1/20th wave. Thermal-induced wavefront errors of approximately 1/20th wave are anticipated which, combined with the manufacturing tolerance, should lead to approximately 1/10th wave performance (95 percent perfect system on the basis of systematic wave errors). It appears possible through tight control on random and systematic surface errors to achieve a Strehl ratio in the order of 0.8 or better (a Strehl ratio of 0.8 is equivalent to the Rayleigh quarter-wave criteria).

Alignment error tolerances are quite tight for this system. It will be necessary to hold alignment to approximately 0.003 in. decentration and 0.0125 degrees tilt of the secondary mirror with respect to the primary mirror. These tolerances yield an almost negligible loss in the MTF of the system and reduce the Strehl ratio by about 0.1. To stay within the alignment tolerances, it will be necessary to realign the optical system in orbit. An alignment system has been designed which is to be built into the optical system to allow the astronaut to realign the telescope at any time even when observing the sun. This system is described in a different document.

Since the earth-orbiting spacecraft will not be in sunlight continually, thermal cycling of the telescope will occur resulting in focal shifts at the final image plane. Although the f/50 system has considerable depth of focus, it will be

necessary to refocus the camera on each orbit. Due to the high magnification of the secondary mirror (m = 13), positioning of the secondary is very critical; hence focusing will be done by moving the camera cluster rather than the secondary. Focusing will be monitored by a television camera. Spectrum analysis of the video signal will be used to determine when the condition of best optical focus is achieved.

PHOTOHELIOGRAPH OPTICAL SYSTEM

INTRODUCTION

After careful consideration of a number of reflecting optical designs, the Gregorian design has been chosen for the photoheliograph experiment. This report lists the requirements imposed on the optical system by the experiment and describes briefly the considerations leading to the choice of the Gregorian design. The actual optical design, as modified to meet the solar heating problem is shown. Also, the method of manufacturing an internally-cooled primary mirror is illustrated. Filter problems and approaches to filtering ultraviolet light and the hydrogen-alpha line are discussed. The optical performance expected of the optical system including effects of image motion, mirror surface errors, and optical misalignment is examined and the need for an in-flight alignment system noted. Lastly, the requirement for and approach to an in-flight focus capability is presented.

Supplemental information pertaining to the photoheliograph optical system may be found in the following concurrent reports:

1. Photoheliograph Alignment System, 750-11
2. Photoheliograph Primary Mirror Development, 750-7
3. Photoheliograph Optical Testing, 750-10

The cut-off date of this report is 30 June 1968.

REQUIREMENTS

The optical requirements of the photoheliograph solar imaging experiment are as follows:

Resolution – It is desired to realize the diffraction-limit resolution obtainable with the maximum possible aperture that can be accommodated by the spacecraft structure. Due to spacecraft size limitations, it will not be possible to utilize an aperture yielding an order of magnitude better resolution than the best obtainable from the earth's surface. The maximum aperture obtainable within the ATM cannister is 65 cm (25.6 in.) which yields a diffraction-limited resolution of 0.19 arc sec. However, it will be possible to obtain observations

of solar phenomena continuing for long periods of time at better resolution than obtainable from earth. For example, during a 40-day earth-orbiting mission, it should be possible to observe the sun for something like $0.5\text{-}1.0 \times 10^6$ seconds at a resolution approximating 0.2 arc sec.

Spectral Range – Images of the sun are to be photographed simultaneously in three spectral regions; i.e., ultraviolet (1500-3000 Angstroms), visible light (4000-6000 Angstroms), and the hydrogen-alpha line (6563 Angstroms). The resolution and modulation transfer functions (MTF) quoted in this report will assume a wavelength of 5000 Angstroms. It is necessary that the hydrogen-alpha filter be tunable by approximately five Angstroms on either side of the central wavelength.

Field of View – There is no stringent requirement on the field of view of the photoheliograph other than it be large enough to study and follow dynamic surface and atmospheric phenomena. A field size of 1/10th the solar diameter is satisfactory.

Focal Ratio – The two factors affecting the focal ratio are the plate scale (number of arc-sec/mm in the final focal plane) and the incompatibility of hydrogen-alphas filters with large or moderate beam convergence angles. A focal ratio of f/50 satisfies the plate scale and the beam convergence requirements. For a 65-cm aperture, the f/50 focal ratio yields a plate scale of 6.3 arc-sec/mm which is suitable for either vidicon of film recording.

DESCRIPTION

Configuration – To obtain the maximum possible resolution, the largest aperture commensurate with spacecraft physical constraints is to be used. For the ATM-B mission, this aperture is 65 cm (25.6 in.). At f/50, the focal length will be 32.5 meters. The spacecraft, however, constrains the total length of the telescope to 3.0 meters. Thus, it is seen that considerable compression of the optical path is required. This, coupled to the requirement for a very broad spectral range, led to consideration of reflector-type designs for the optical system. Because of the small field angle requirement (several arc-minutes), field-correcting lenses are not required, and the system can be a pure reflector for maximum ultraviolet transmission. (Light for the visible-light and H-alpha

cameras will be transmitted through beam-splitters, but light to the ultraviolet camera will not be transmitted through absorbing media.)

Figure 1 shows the three major subdivisions of reflecting optical designs considered for the photoheliograph. The Cassegrain is a very popular design due to the fact that it provides maximum focal length for minimum tube length. The Gregorian system shown here is a classical Gregorian design modified to provide means of "dumping" the unused portion of the solar image upstream from the secondary mirror. (It should be noticed that the solar diameter subtends approximately 32 arc-minutes whereas the image size required for the experiment is approximately 1/10th the diameter; hence, 99 percent of the solar image is unused.) The tertiary system is an approach to obtaining high magnification through a series of two low-magnification steps. It might be called a Cassegrain-Gregorian system since it combines the features of both designs (parabolic primary mirror, hyperbolic secondary mirror, and elliptical tertiary mirror).

Due to the high magnification required of the Cassegrain secondary mirror, a large, out-of-focus image of the sun is intercepted by the primary mirror. This out-of-focus image moves about on the primary mirror as the telescope is pointed to various portions of the solar disk (see Figure 2). This results in large thermal discontinuities on the primary mirror — a very difficult thermal situation to contend with.

Figure 3 shows that, except for that portion of the primary mirror in the shadow of the secondary cage, the primary mirror of the Gregorian design is evenly illuminated at a level of one solar constant. Also, very important is the fact that 313 watts (70 percent of the total flux incident on the primary mirror) is reflected back into space by the heat shield and heat dump mirrors. Only 2.1 percent of the solar flux reflected by the primary mirror reaches the secondary. Table 1 summarizes the advantages and disadvantages of the three reflecting designs. Although the Gregorian design will have greater sensitivity to misalignment than a Cassegrain system if constricted to the same tube length (faster primary focal ratio and greater secondary magnification required by the Gregorian), the Gregorian design modified to include a prime-focus heat dump has been chosen for the photoheliograph because of the thermal considerations discussed above. The optical performance of the Gregorian will be completely

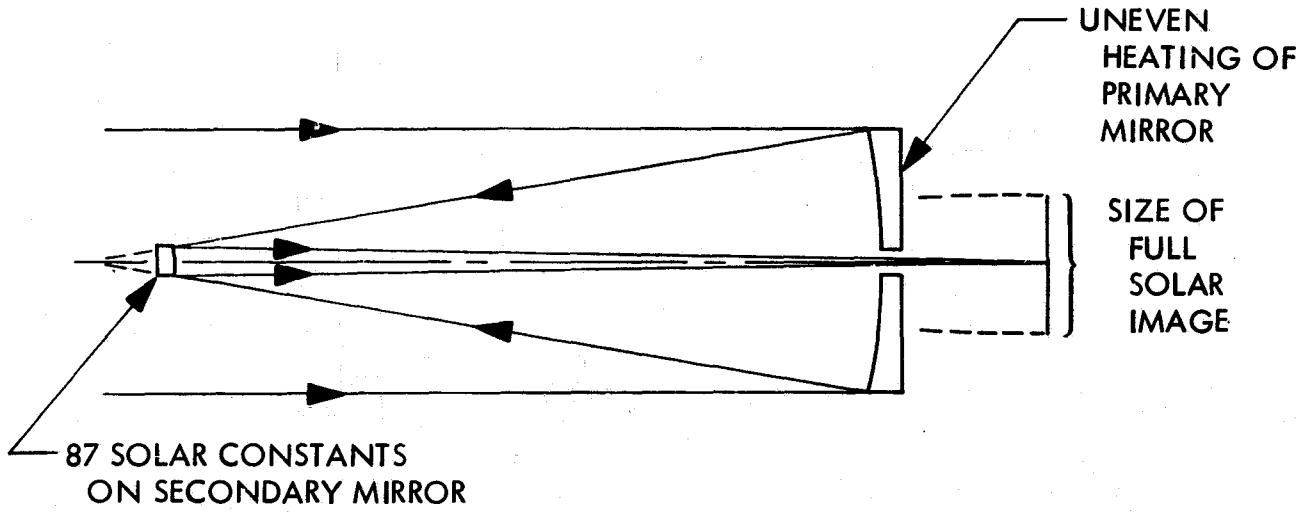

HIGH-MAGNIFICATION CASSEGRAIN

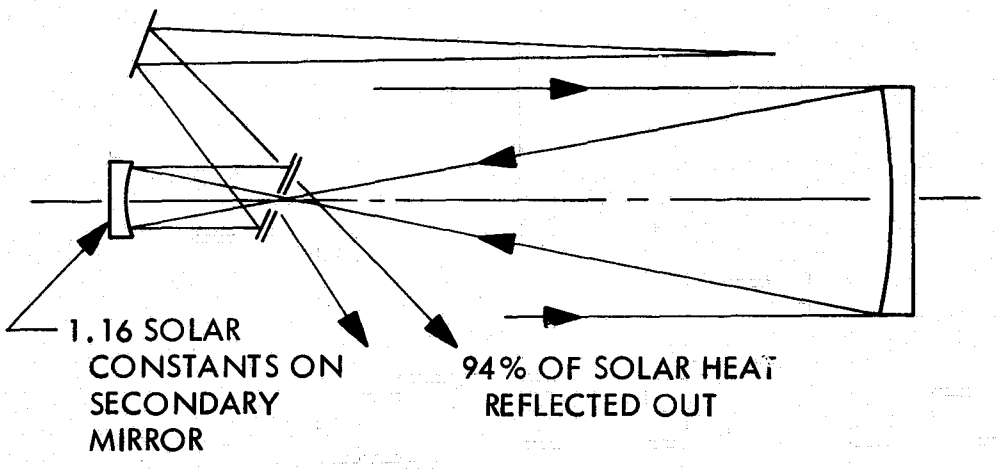

HIGH-MAGNIFICATION GREGORIAN WITH HEAT DUMP

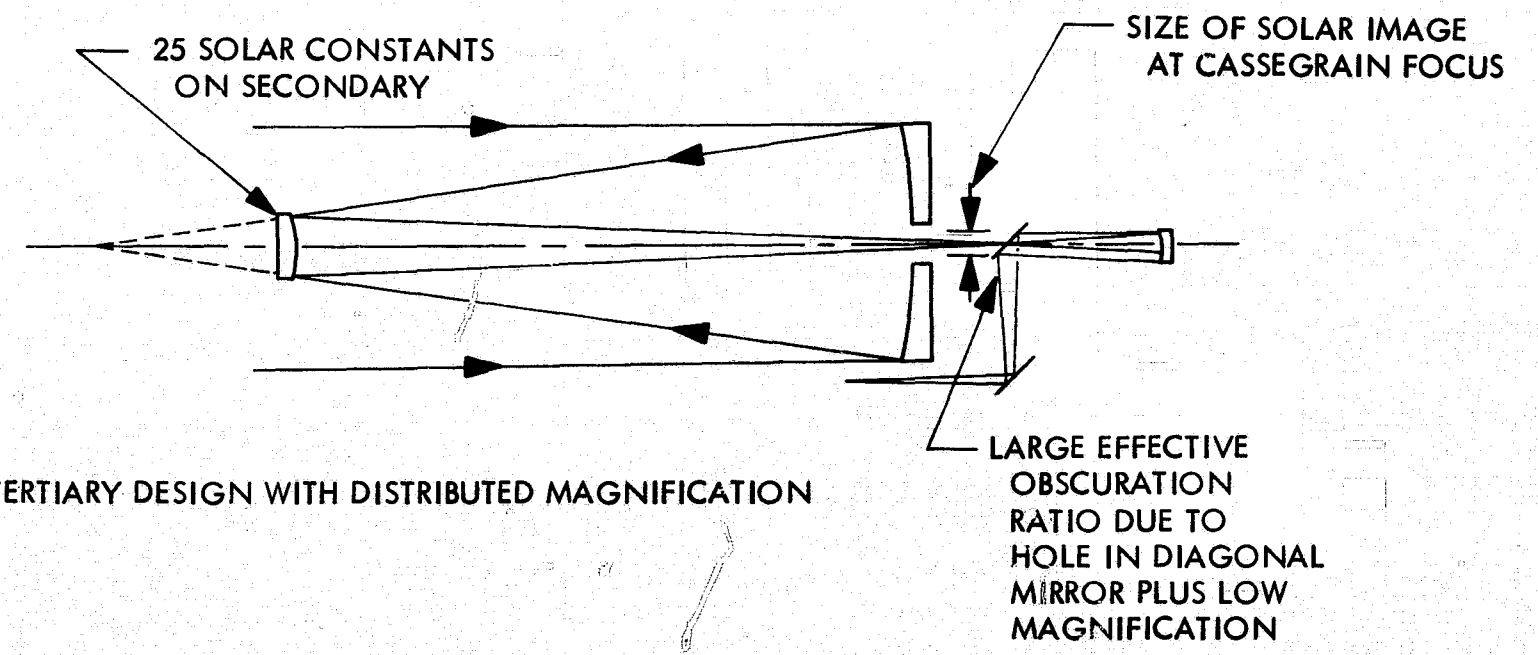

TERTIARY DESIGN WITH DISTRIBUTED MAGNIFICATION

Figure 1. Three Reflecting Designs Considered

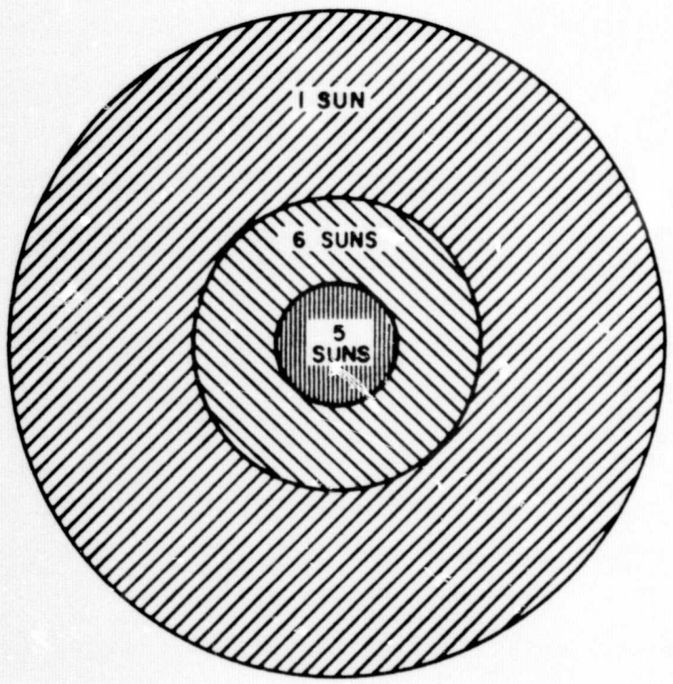

OBSERVATION OF CENTER OF THE SUN

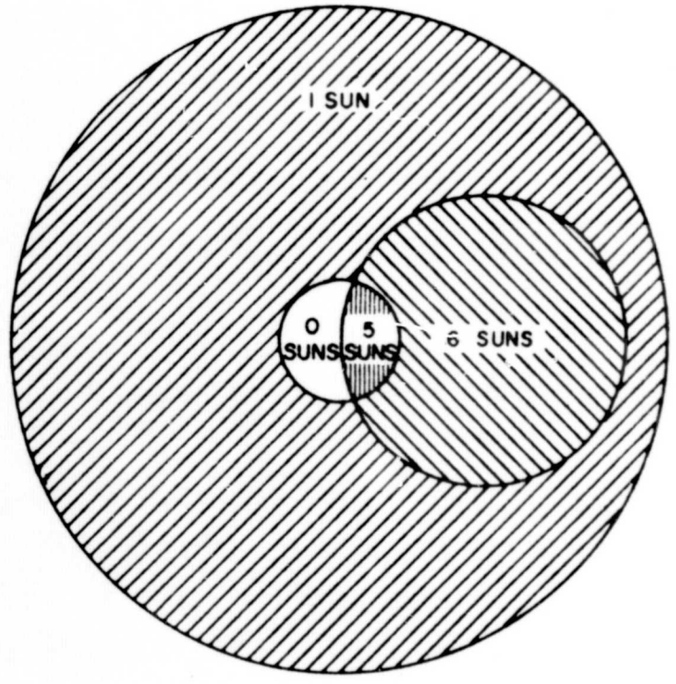

OBSERVATION OF LIMB OF THE SUN

Figure 2. Out-of-Focus Solar Image on Cassegrain Primary Mirror

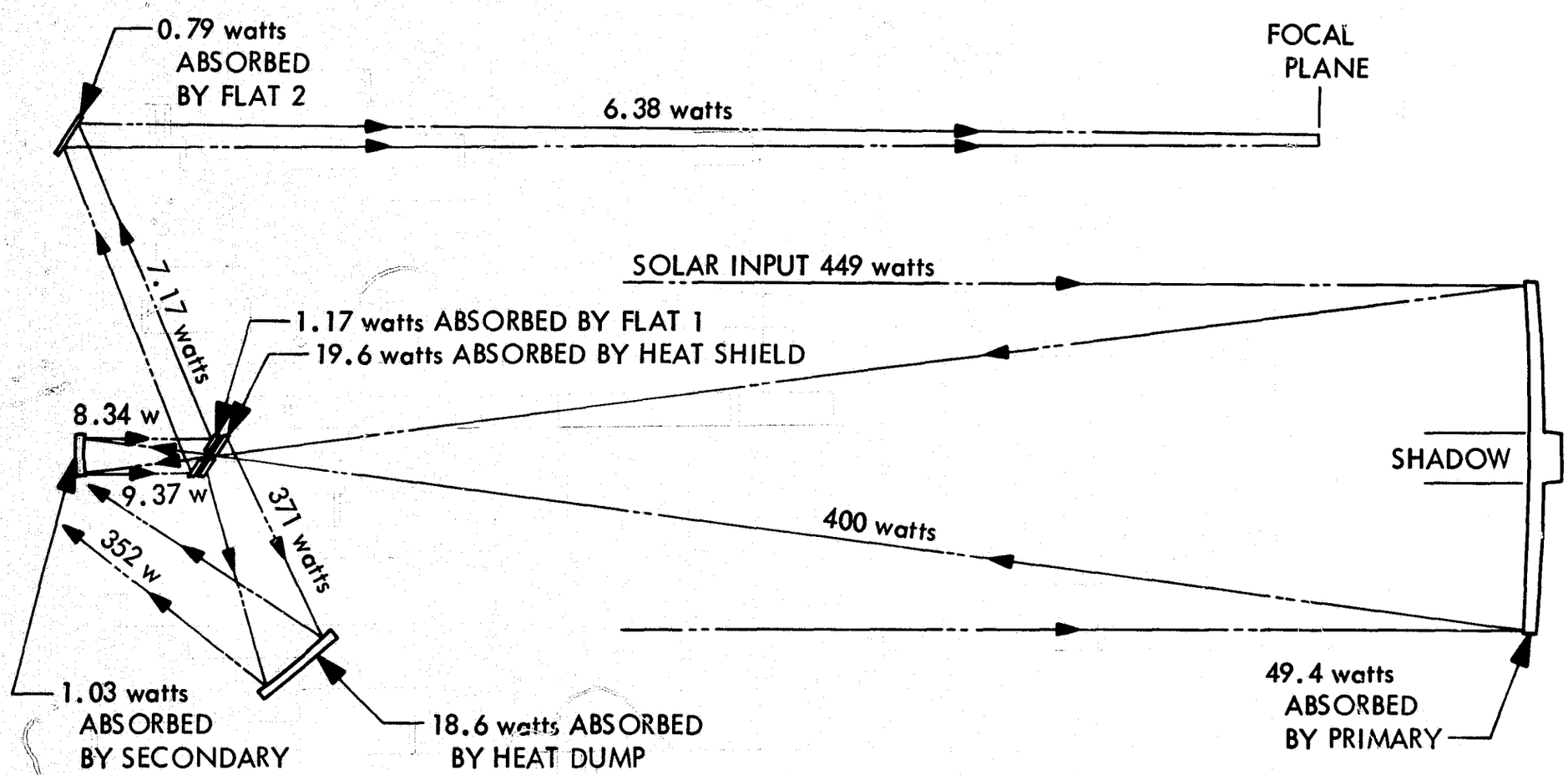

Figure 3. Heat-Flow Diagram, Gregorian Optical System

Table 1. Comparison of Three Reflecting Designs

System	Advantages	Disadvantages
Cassegrain	For a given tube length, can utilize primary mirror with larger f/no. resulting in less coma and astigmatism.	Large heat flux on secondary mirror (87 suns) Uneven heating of primary mirror
Gregorian	Approximately 70% of solar flux falling on primary mirror is dumped overboard. Solar flux is approximately one solar constant on all optical imaging surfaces. Eliminates uneven heating of the primary mirror.	For a given tube length, must utilize primary mirror with smaller f/no. resulting in more coma and astigmatism
Tertiary	Eliminates uneven heating of the primary mirror. For a given tube length, can utilize primary mirror with larger f/no. resulting in less coma and astigmatism.	Still has large heat flux on secondary mirror (25 suns) Large effective obscuration ratio results from combination of low-magnification third stage and hole in heat-stop mirror

adequate for the experiment if the system is kept aligned within rather tight tolerances. The alignment tolerances of the Cassegrain system will not be as tight; however, the thermal problems associated with the Cassegrain outweigh any optical advantages it may have in regard to alignment sensitivity. If properly aligned, the performance of the Gregorian will be essentially identical to that of the Cassegrain over the small field of view required.

The tertiary design, while relieving the thermal problem on the primary mirror still suffers from a large solar flux on the secondary mirror as well as a large inherent effective obscuration ratio. The large value for the minimum obscuration ratio is not due to the secondary mirror, but to the beam-folding mirror (or prism) following the secondary mirror as shown in Figure 4. The

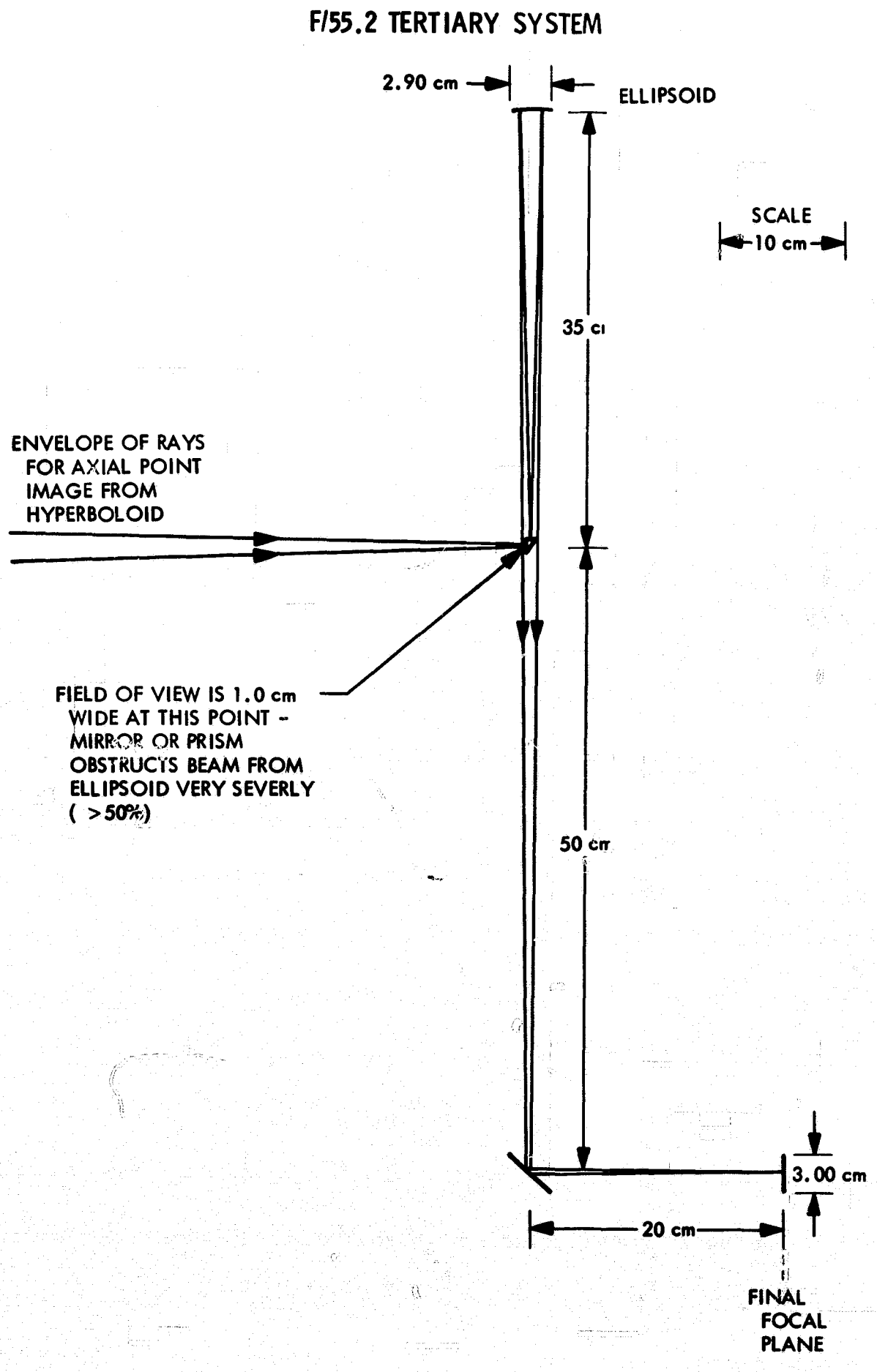

Figure 4. Effective Central Obscuration in Tertiary Section of Tertiary Design

example shown in the figure suffers from an obscuration ratio of greater than 0.5. The minimum value which can be achieved is about 0.3. The obscuration due to the beam-folding mirror can be avoided by using the ellipse in an off-axis situation so that the beam reflected by the ellipse passes just to one side of the beam-folding mirror. However, it is necessary to work at an angle of approximately four degrees off axis which is much too large for a conic section mirror. The other alternative is to use an off-axis segment of an on-axis ellipse. This approach also is questionable. An attempt to use this method for eliminating the two folding flats in the modified Gregorian design (see Figure 5) was unsuccessful as the computed image size became unacceptably large at field angles of one arc minute.

A list of design considerations and trade-offs are listed in Table 2. The design considerations apply to any of the types of reflecting systems considered for this application. Assuming that the system focal ratio is frozen at approximately f/50, only considerations 2-4 need be given attention. Spacecraft size limitations require that the primary focal ratio be low. Mirrors of low focal ratio are more difficult to build and to test than mirrors of higher focal ratio. For lower primary focal ratios, higher secondary magnifications are required resulting in less tolerance to mirror spacing and misalignment errors. One advantage, however, of the high secondary magnification is the small central obscuration of the primary aperture due to the smaller size of secondary mirrors associated with higher magnification. The effect of large obscuration ratios (ratio of diameter of obscuration caused by secondary mirror cell to diameter of primary mirror aperture) is to diffract energy out of the central Airy disk into the diffraction rings, thus reducing contrast. This is shown in Figure 6 where the energy distribution in the central Airy disk and the first diffraction ring is shown for various obscuration ratios. To reduce this effect to a practical minimum, a maximum obscuration ratio of 0.2 has been specified for the photoheliograph.

In the design of reflecting optical systems, it is advantageous to minimize the number of reflecting surfaces. Figure 7 shows the loss of system transmission as a function of number of mirror surfaces. The image quality as measured by the Strehl ratio* is listed as a function of the

*For definition and method of calculating the Strehl ratio, see Appendix A. A Strehl ratio of 1.0 represents a perfect optical system.

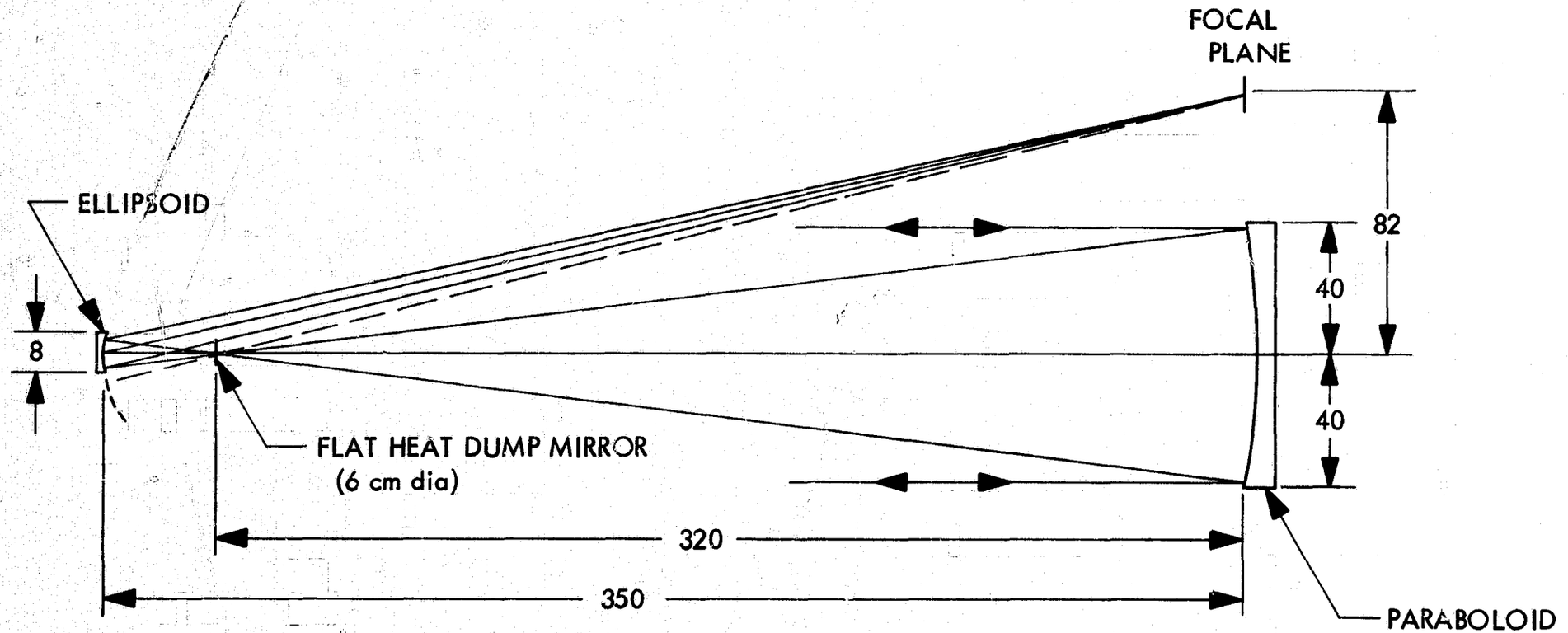

NOTE:

a. FLAT HEAT-DUMP MIRROR AT PRIME FOCUS REFLECTS UNUSED PORTION OF SOLAR IMAGE BACK TO PRIMARY MIRROR WHERE IT IS RE-COLLIMATED AND REFLECTED BACK INTO SPACE

b. ELLIPSOIDAL MIRROR IS USED OFF-AXIS (AXIS SHOWN BY DOTTED LINE)

c. ALL DIMENSIONS ARE IN CENTIMETERS

d. SCALE = 1:20

F/48.3 GREGORIAN WITH m = 12.5

Figure 5. Tilt-Axis Gregorian Design

Table 2. Design Considerations

1. System Focal Ratio
   a. plate scale proportional to system focal ratio
   b. depth of focus increases with focal ratio
   c. coma and astigmatism inversely proportional to focal ratio
   d. hydrogen-alpha filter requires low-convergence beam (i. e., high focal ratio)
2. Primary mirror focal ratio limited by spacecraft size
3. Secondary mirror magnification
   a. high magnification results in less central obscuration
   b. low magnification yields higher tolerance to mirror spacing and mis-alignment for a given system focal ratio
4. Number of reflecting surfaces
   a. system transmission decreases with increase in number of mirrors
   b. random surface errors add statistically
   c. symmetrical systematic errors in one mirror surface may be cancelled through compensating systematic error in another mirror

number of mirrors in an optical system in Table 3. For this table it has been assumed that all mirrors surfaces have 1/50th wave rms random surface errors.

The optical schematic for the Gregorian design chosen for the photoheliograph is shown in Figure 8. The primary mirror focal length of 250 cm is chosen as being essentially as long a focal length as is practical to fit into the 275-cm (108-in.) optical working length. Since the total distance allowed by spacecraft constraints for the telescope is 120 in. we see that 12 in. (120-108 in.) remains for accommodating mirror thickness, mirror mounts, and structure behind the mirrors. Not shown in this drawing are the two dichroic beam splitters and several filters associated with the three cameras located at the Gregorian focus.

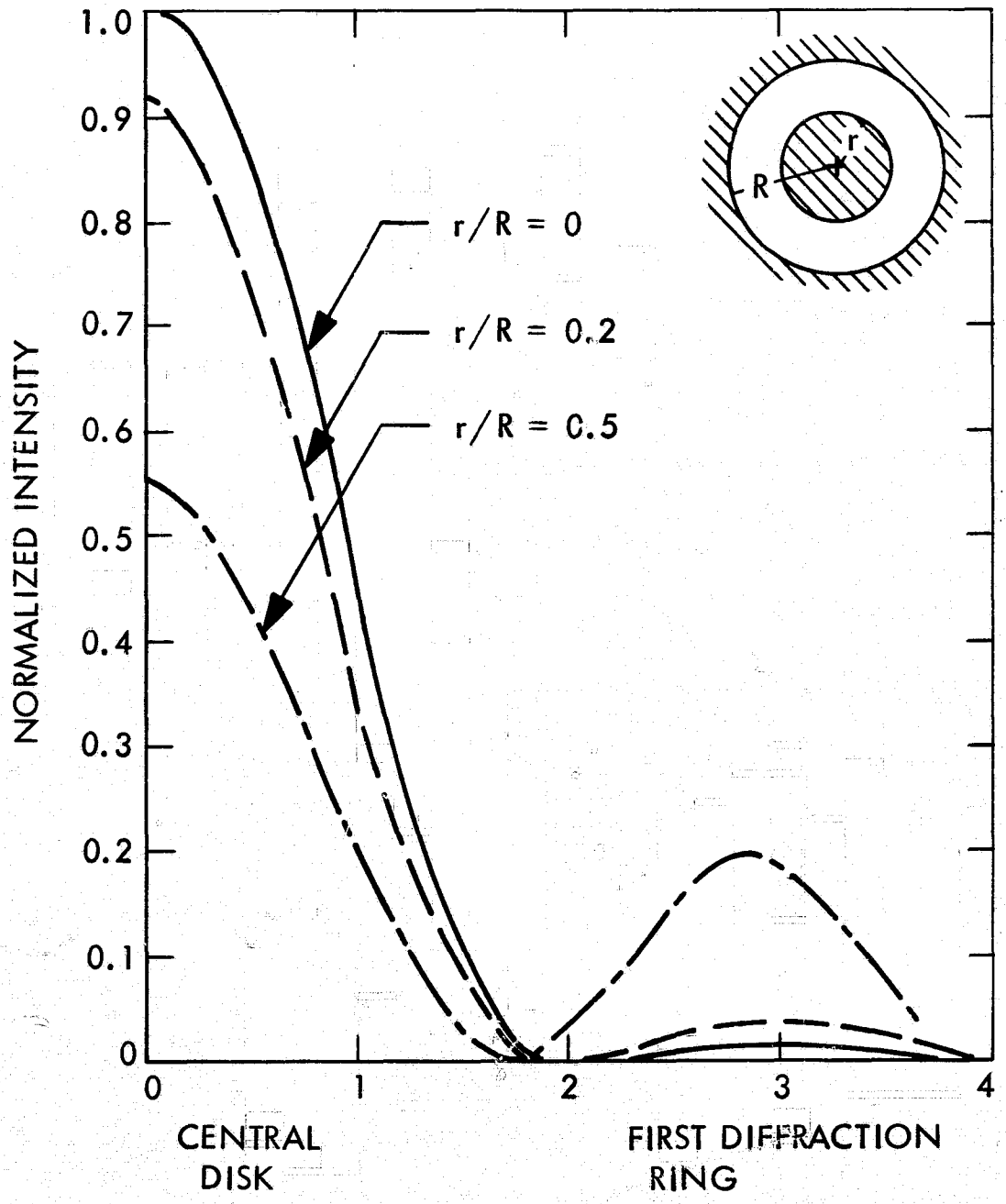

Figure 6. Effect of Central Obscuration on Diffraction Pattern

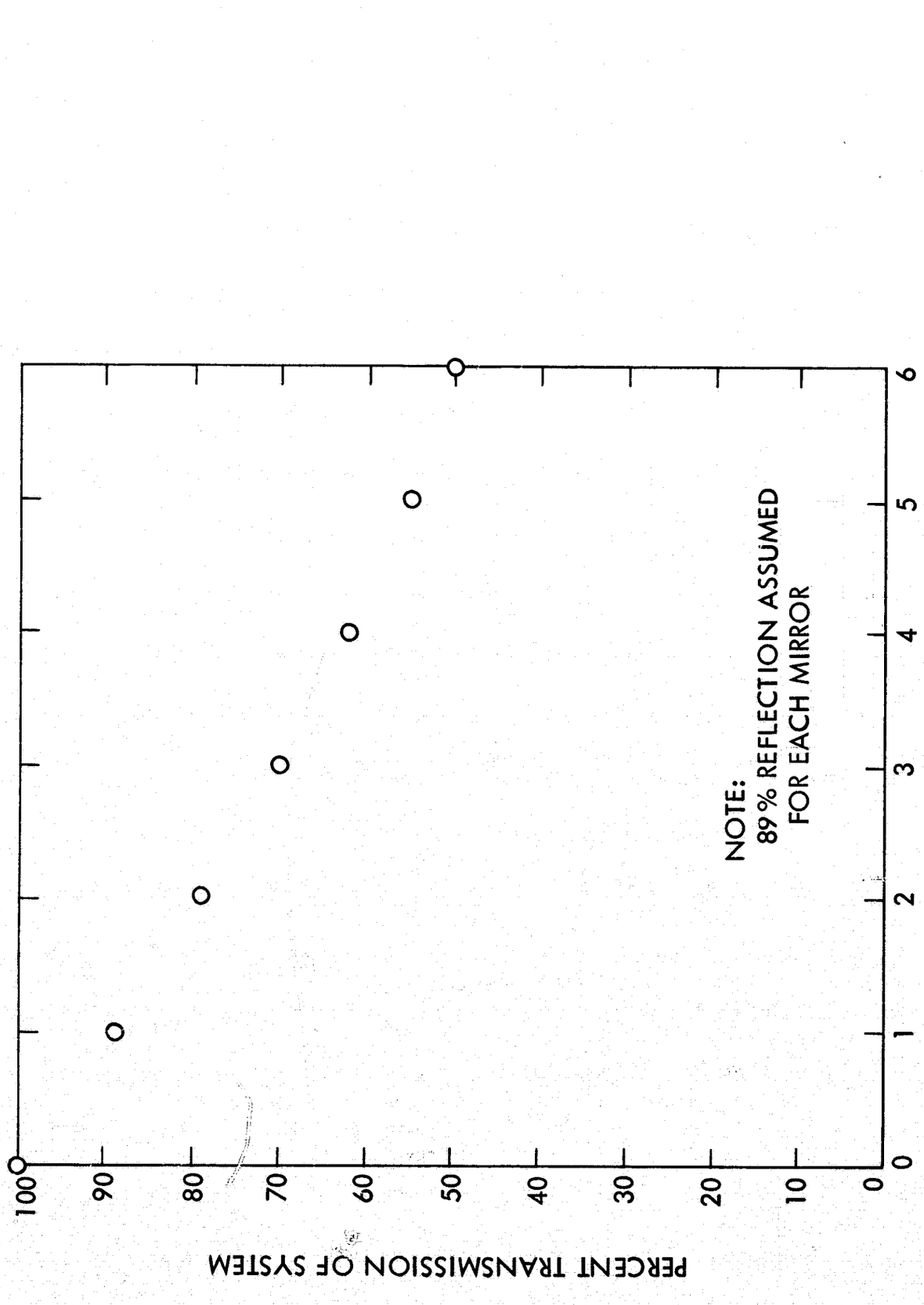

Figure 7. System Transmission vs Number of Mirrors

Table 3. Effect of Number of Mirrors on Image Quality

Number of Mirrors in Series	Strehl Ratio
1	0.94
2	0.88
3	0.82
4	0.76
(for 1/50th wave rms surface accuracy)	

The function of the heat-stop mirror is primarily that of diverting unwanted solar flux out of the optical imaging system.* Since the cameras will be recording a field of view having a maximum dimension of 3.2 arc minutes (diagonal dimension of image recording format), only that light coming from 1/100th of the solar disk (disk diameter = 32 arc minutes) is required in the Gregorian focal plane. Thus it would seem that the hole in the heat-stop mirror should be 0.1 of the prime-focus image diameter (2.33 cm); i.e., 0.233 cm. However, due to tolerances which must be allowed for misalignment of the secondary mirror support structure and the Gregorian focal-plane image apertures, the hole diameter is enlarged to 0.36 cm. Therefore, 0.024 ($= 0.36^2/2.33^2$) of the solar energy in the prime focus passes through the hole into the secondary system of the telescope. It should be noted that although the heat-stop mirror acts as a field stop in the prime-focus image plane, it does not constitute the actual field stop for the total instrument. The hole is made large purposely so that it does not accidentally act as a field stop for the instrument. The true field stop is defined either by a film-gate aperture in the case of film cameras or by the size of the scan raster in the event vidicon cameras are used.

*The photoheliograph contains three optical systems all of which are interrelated. The optical imaging system is that which forms an image of a portion of the solar disk at the Gregorian focus. The other optical systems are the heat removal system (heat-stop and heat-dump mirrors) and the alignment system which is described in a separate report.

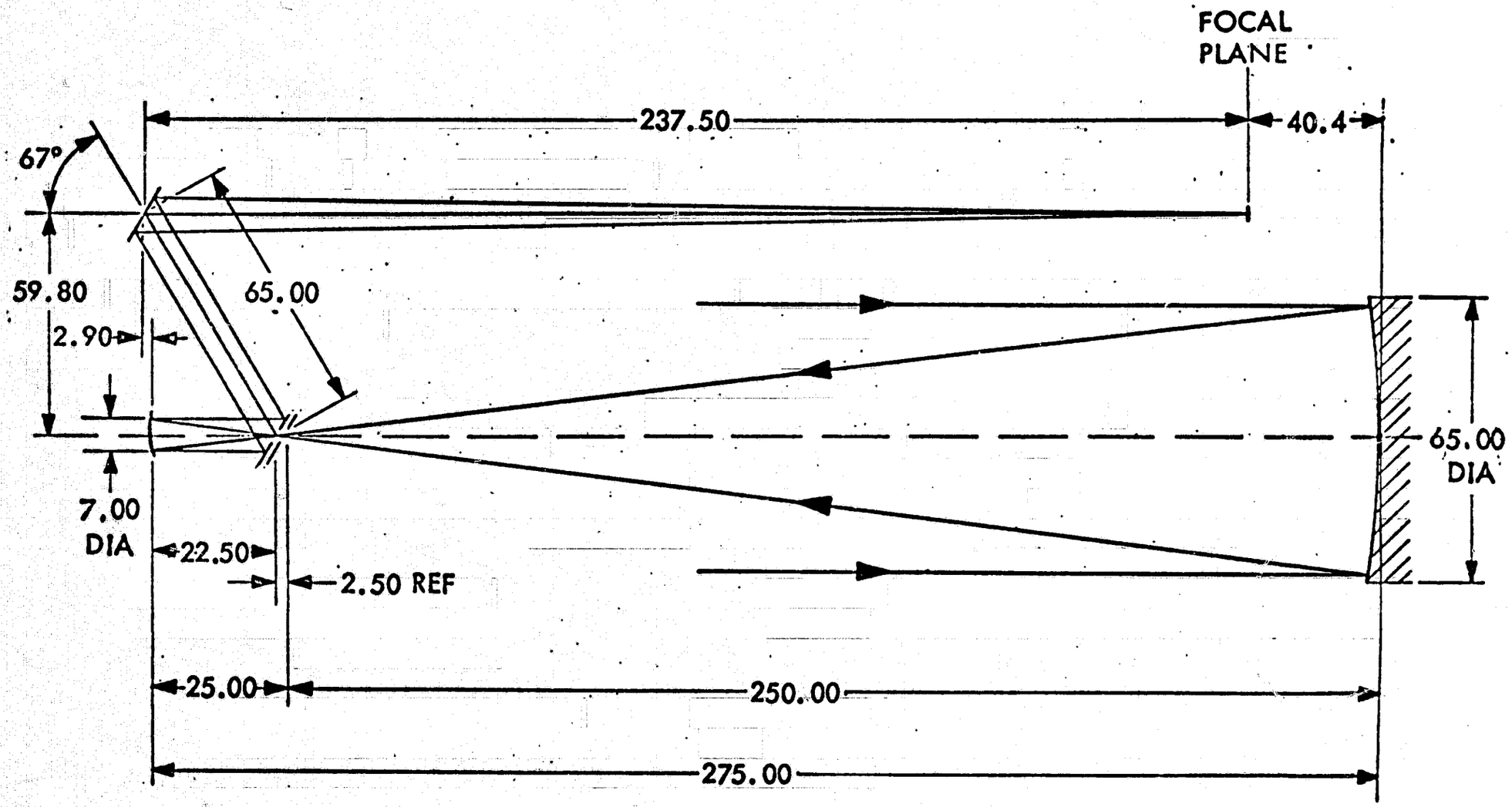

ALL DIMENSIONS
IN cm

PRIMARY F-RATIO = 3.85
E.F.L. = 3250 cm
ECCENTRICITY OF SECONDARY = 0.8571428
CURVATURE OF SECONDARY = 0.021538461 cm^{-1}

Figure 8. f/50 Gregorian Telescope with Magnification = 13

Table 2 indicates that a low magnification is desired in order to have greater tolerance to primary-secondary mirror spacing and misalignment. Now, system focal ratio = magnification x primary focal ratio = 50,

$$(f/no.)sys = m \times (f/no.)_{pri} = 50$$

The maximum $(f/no.)_{pri}$ that can be accommodated within the space constraints is approximately f/4. Actually, f/3.85 has been used for this design in order to allow for a 10-in. spacing between the prime focus and the secondary mirror. This spacing cannot be reduced significantly due to the "periscope" section of the optical system; i.e., that portion of the optical system lying between the two diagonal flats. The beam reflected from the secondary experiences an effective central obscuration caused by the hole in the center of the first diagonal flat (not to be confused with the heat-stop mirror) as shown in Figure 9. Ideally, this should not be greater than the obscuration caused by the secondary-mirror cell in the beam incident on the primary mirror. The effective obscuration is proportional to the angle between the normal to the first diagonal mirror and the optical axis of the secondary mirror (see Appendix B). To minimize the effective obscuration it is desirable to keep this angle as small as possible. A value of 67/2 degrees, as used in the photoheliograph design, keeps the effective obscuration very close to the value of 0.2, the limit chosen on the basis of diffraction considerations. This angle has a direct bearing on the minimum distance allowable between the end of the telescope structure (approximately the plane of the secondary mirror) and the first diagonal flat mirror, the heat dump mirror, and consequently the prime focus. If one wishes to keep the vertical height of the periscope section essentially as shown in Figure 10 (i.e., 59.80 cm), then decreasing the angle increases the distance between the secondary mirror and the prime focus thereby decreasing the focal ratio of the primary mirror. As the focal ratio is decreased, the magnification goes up, however, not sharply. But the object distance for the secondary mirror (distance from secondary mirror to prime focus) increases and must be multiplied by the increased magnification to obtain the back focal length of the telescope (optical distance from secondary mirror to Gregorian focus). The increase in the product of the increased magnification times the increased object distance is significant. For example, if the angle were decreased from its present value of

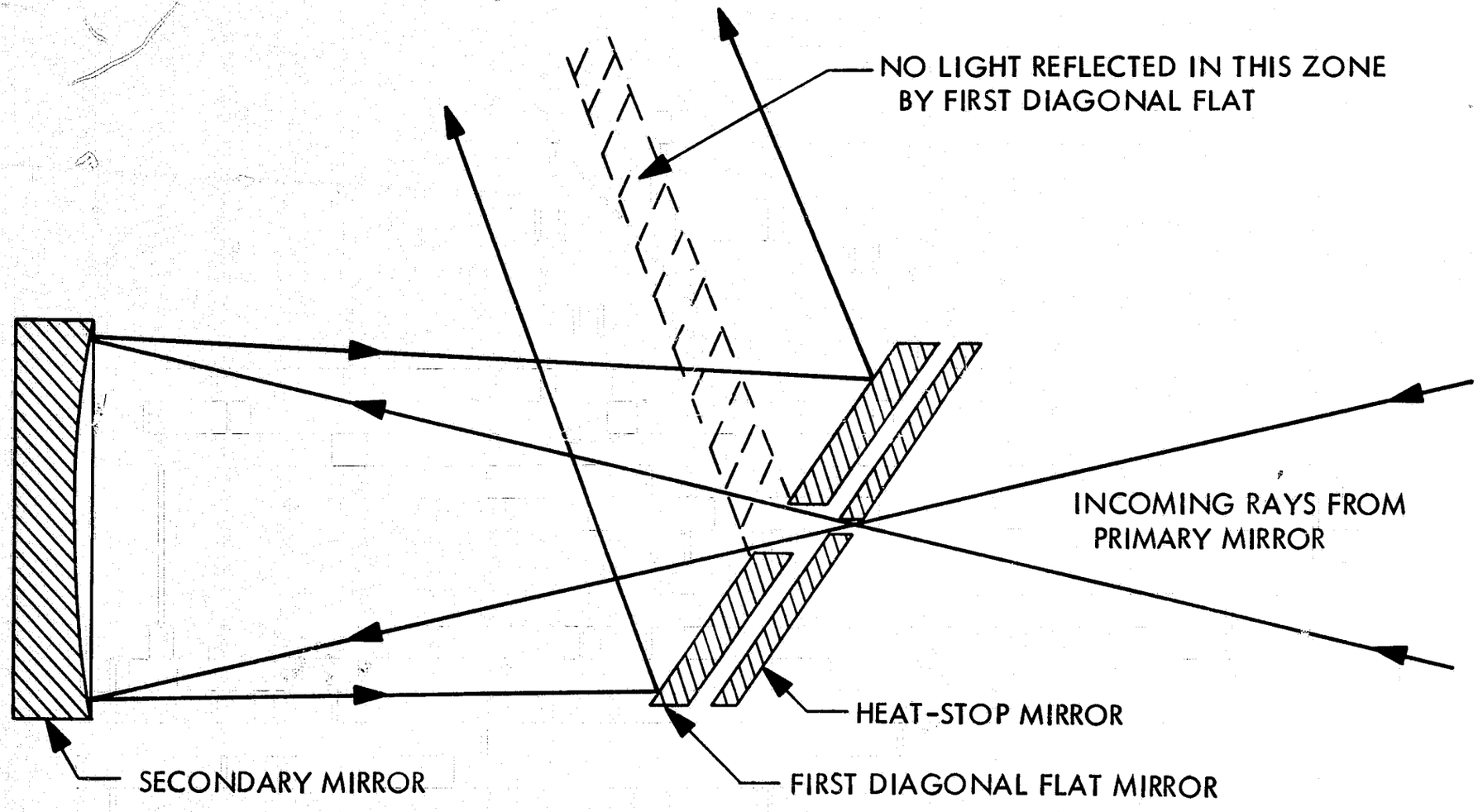

Figure 9. Effective Central Obscuration Caused by Hole in First Diagonal Flat

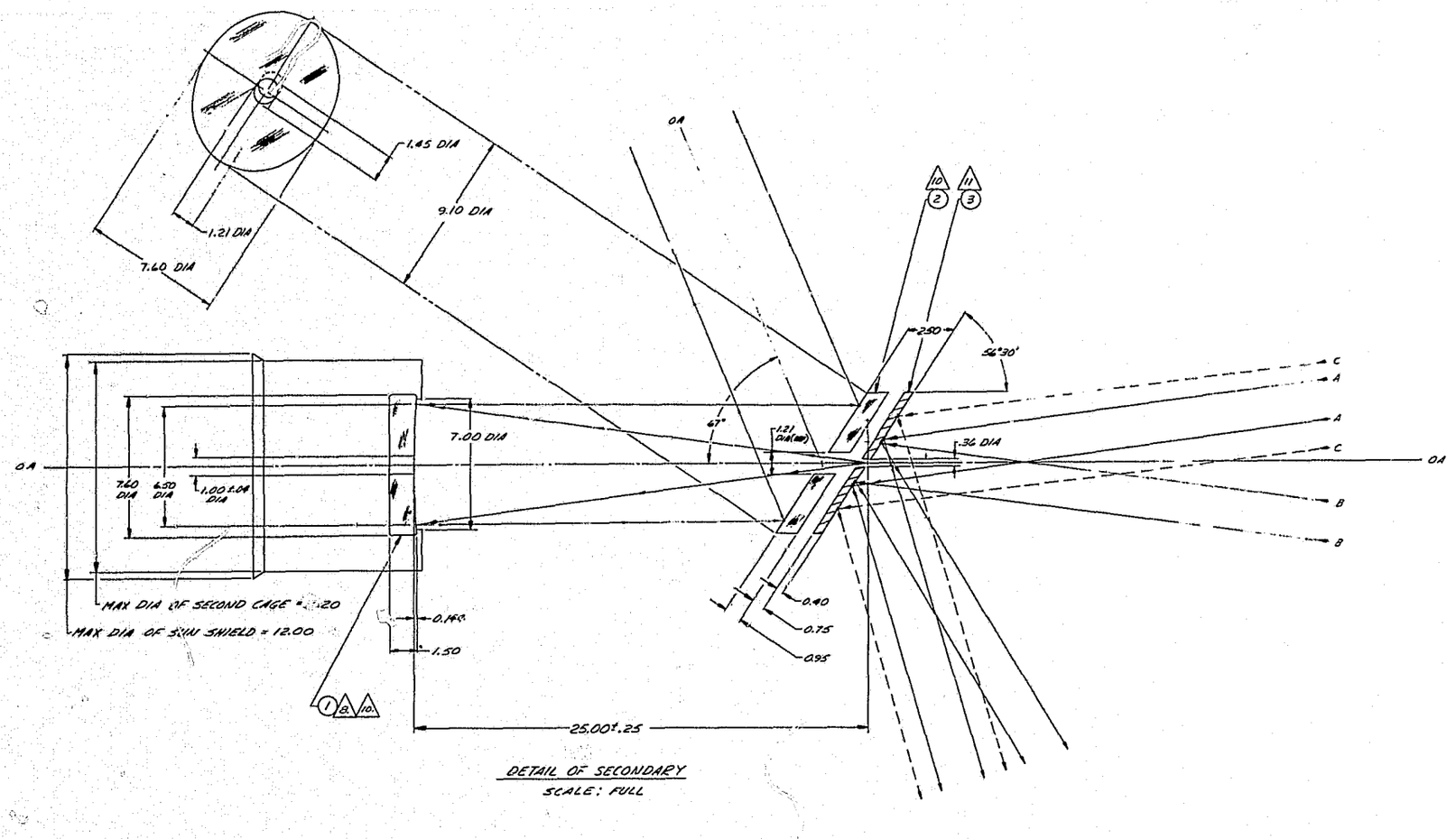

DETAIL OF SECONDARY
SCALE: FULL

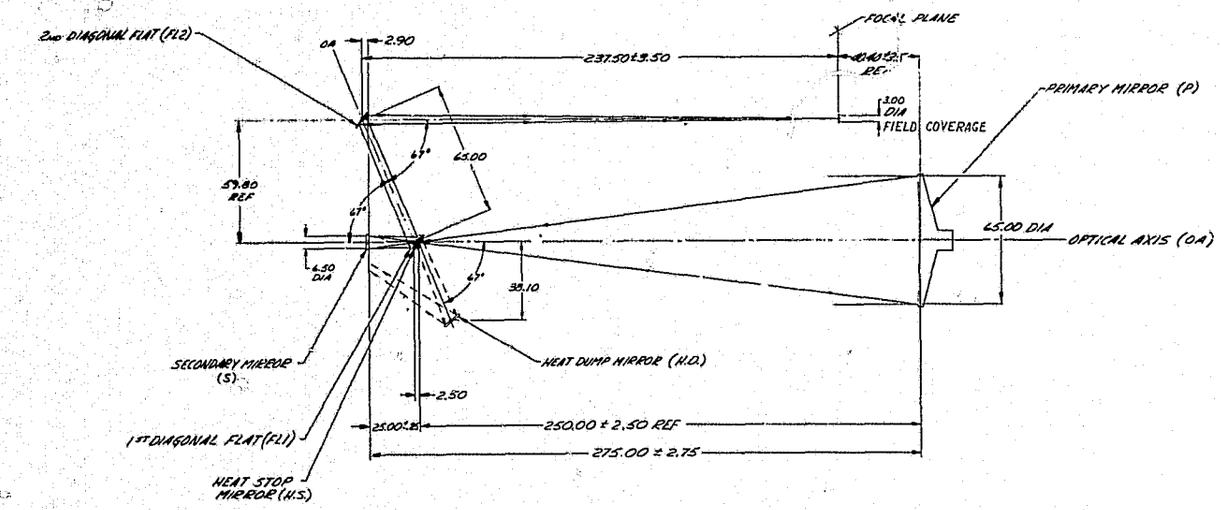

OPTICAL SCHEMATIC DIAGRAM F/50 GREGORIAN, 65 cm APERTURE
SCALE: 1/10

11. MATERIAL: ALUMINUM, SILVERED.
10. MATERIAL: CER-VIT, ALUMINIZED.
9. A & B ARE MARGINAL RAYS DEFINING PRIME-FOCUS IMAGE OF SOLAR DISK (ON-AXIS IMAGE). C, SIMILAR TO A & B FOR LIMITS OF SOLAR IMAGE ON (3) WHEN OBSERVING SOLAR LIMB.
8. (1) $r_1 = 25$, $r_2 = 325$, $m = 13$, $e = 0.85714$
7. TOLERANCES GIVEN ARE FOR FOCAL LENGTH ERRORS OF 1% (MANUFACTURING TOLERANCE OF MIRROR FIGURE).
6. PRIMARY MIRROR IS F/3.85 PARABOLOID.
5. SYSTEM FOCAL LENGTH = 3250.00 cm.
4. DIA OF SOLAR IMAGE AT PRIME FOCUS = 2.33 cm.
3. EFFECTIVE OBSCURATION RATIO DUE TO HOLE IN (2) IS 0.20.
2. TOLERANCES ON ALL MIRROR DIMENSIONS, ARE ±.01 cm = ±.005 in.
1. ALL DIMENSIONS ARE IN CENTIMETERS.

NOTES: UNLESS OTHERWISE SPECIFIED

Figure 10. Optical Schematic Diagram

67 degrees to 57.5 degrees, the object distance of the secondary mirror would increase 50 percent to a value of 37.50 cm, the primary mirror focal ratio would decrease from 3.85 to 3.65, the magnification required would be 50/3.65 = 13.7 which, when multiplied by the 37.50-cm secondary-mirror object distance yields a back focal length of 514 cm. This new back focal length is 189 cm (58 percent) longer than the present design value of 325 cm. To accommodate this increase, an extra folding mirror would be required. As mentioned previously, it is desirable to keep the number of mirrors to a minimum.

The configuration chosen, as shown in Figure 10, represents an optimization of the Gregorian design modified to reject unrequired solar radiation in the following ways:

1. It utilizes the least number of mirrors possible for obtaining an f/50 system focal ratio.
2. The effective obscuration ratio is kept down to a value of 0.2, a very acceptable value.
3. It makes efficient use of all the space available.

Primary Mirror – The evolution of the primary mirror is described in another report (Photoheliograph Primary Mirror Development, 750-7) and will only be summarized here. The thermal constraint of the ATM spacecraft specifies that no more than 0.6 BTU/hr. shall be transferred to the ATM cannister spar at each attachment point from instruments at a temperature different than the spar. This led to the design philosophy that it is necessary to cool the primary mirror and not permit it to come to a hot equilibrium temperature due to incident solar radiation. Computer thermal and stress analysis of three widely variant primary mirror configurations being illuminated with one solar constant of energy led to the relative distortion curves of Figure 11. The hypothetical mirrors in the figure were of fused silica coated with aluminum. A fairly high absorptance of 0.14 was assumed. It is noticed that the mirror which is tapered toward the center (the top curve) suffers the greatest distortion as a result of solar heating. The data of Figure 11 are re-plotted in Figure 12 in terms of one half the wavefront error existing between a wave reflected by the distorted mirror and a wave reflected by a perfect mirror having a best-fit paraboloid shape approximating the distorted mirror. The wavefront error

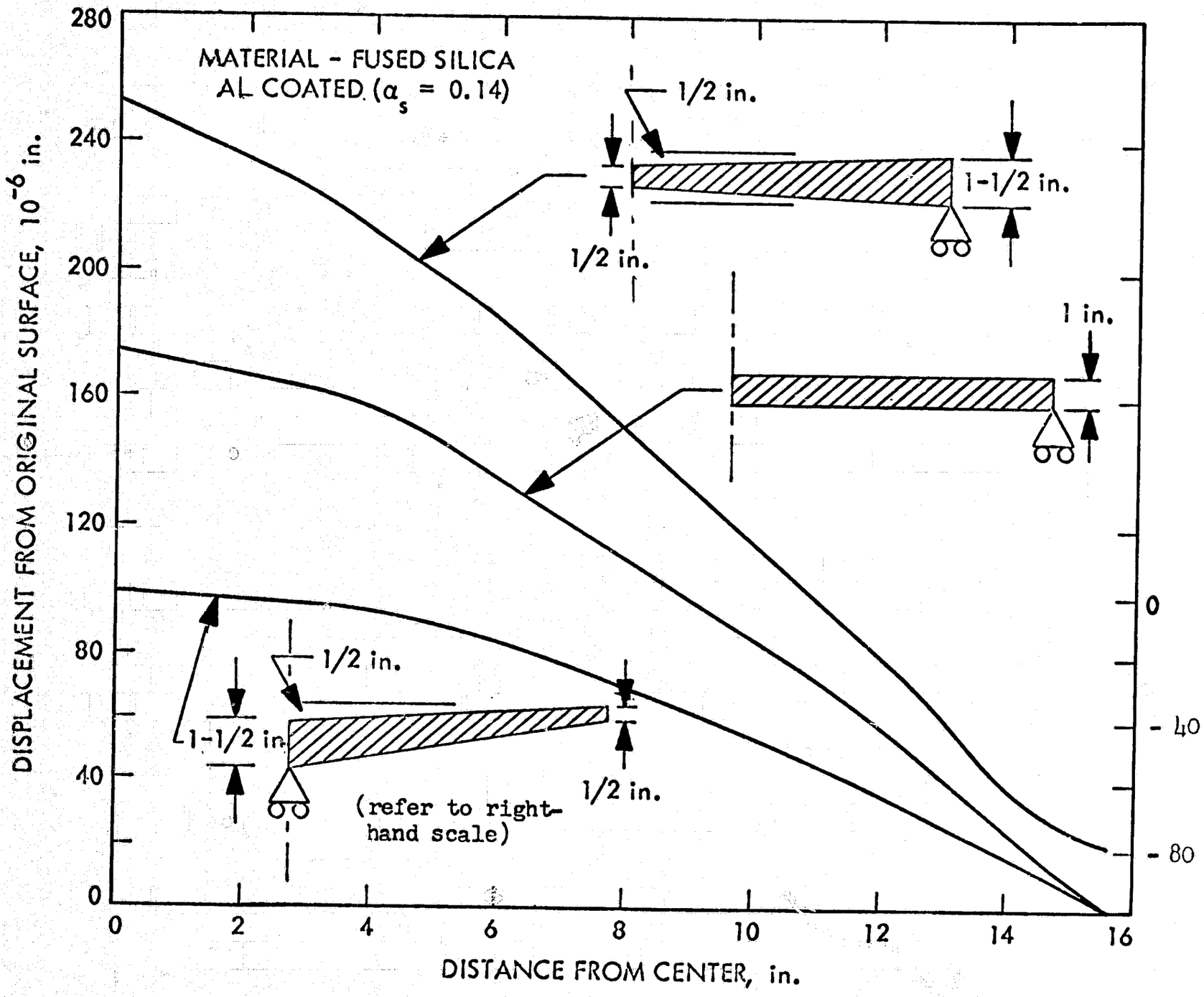

Figure 11. Thermal Distortion Curves for Three Types of Fused-Silica Mirrors

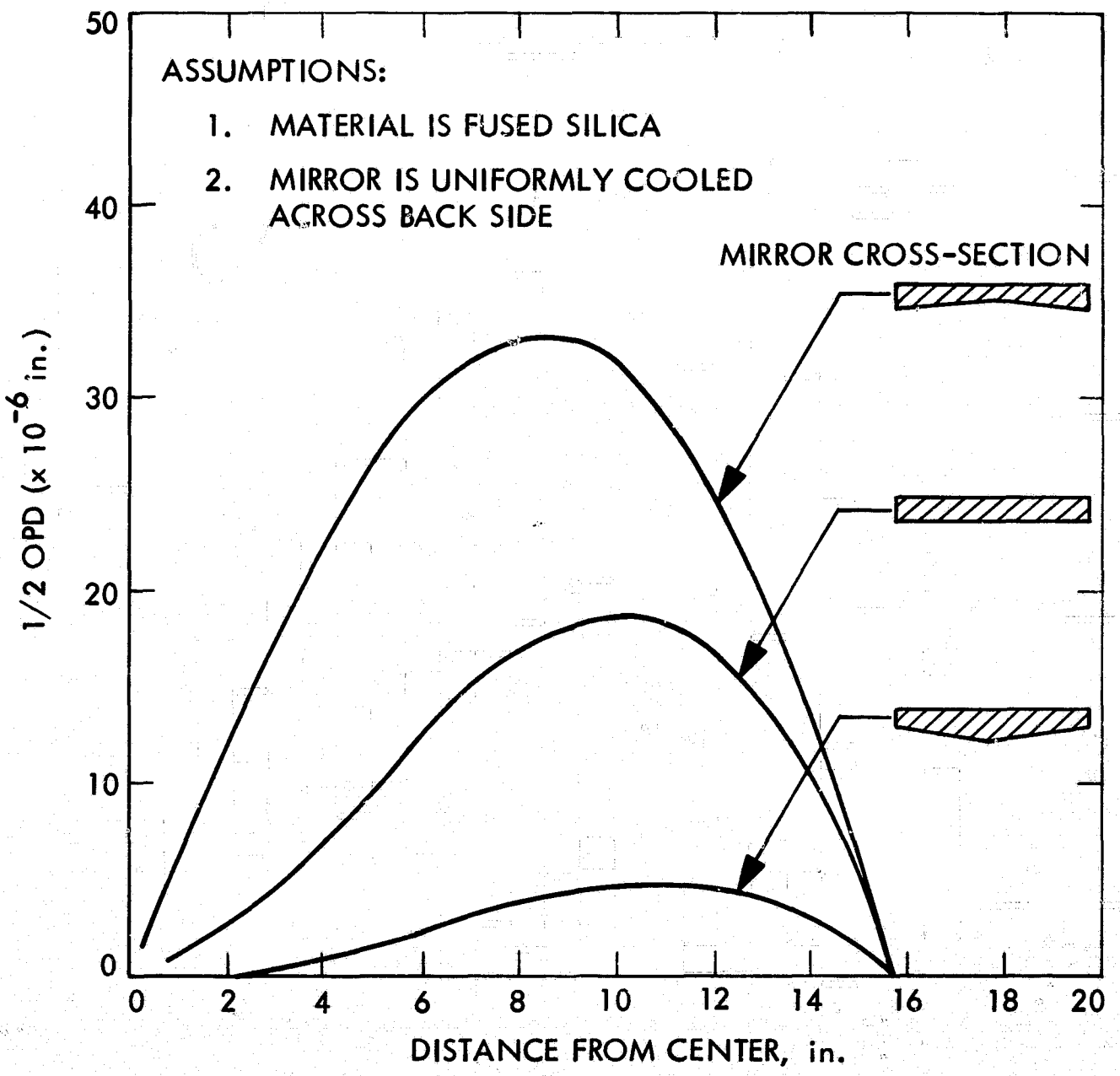

Figure 12. Thermal Distortion of Mirror as a Function of Mirror Blank Shape

is called the Optical Path Difference (OPD) and, due to the nature of reflection, is exactly twice the surface error. The surface error is defined as the displacement between the surface of the distorted mirror at any given distance from the center and the surface, at the same distance from center, of a best-fit paraboloid. The best fit paraboloid is a paraboloid whose focal length is chosen such that the surface errors are minimized. Its use is justified if a refocusing capability is available. Since the surface error is exactly one-half the OPD, we refer to it as the 1/2 OPD and express it in terms of fractional wavelength (λ/n) where λ = 5000 Angstroms.*

Similar curves are plotted for two configurations of Cer-Vit mirrors in Figure 13. We see that the 1/2 OPD of the plane Cer-Vit mirror is nearly $\lambda/20$ which would give an OPD of $\lambda/10$. By itself, a systematic wavefront error of $\lambda/10$ would be quite tolerable. However, if added to wavefront errors due to manufacturing tolerances and misalignment, the thermal-induced $\lambda/10$ wavefront error is intolerable. The tapered mirror yields a thermal-induced surface error of $\lambda/49$ which results in an acceptable wavefront error of $\lambda/24.5$. On this basis, it was decided to use a tapered mirror configuration for all further investigations. It is recognized that the thickness of the mirror must be more than 1.5 inches at the center and 0.5 inches at the edge, as assumed in Figure 13, to give it sufficient stiffness for grinding and polishing and for accurately supporting itself in a gravity field.

The deflection of the mirror due to gravity in a 1-g field is important since the optical system will be manufactured and calibrated in a 1-g field but operated under 0-g conditions in orbit. Therefore, it is very desirable to have sufficient rigidity of the mirror so that its surface does not change significantly when transferred from a 1-g to a 0-g environment. This may be accomplished by designing the mirror so that it is not significantly distorted by a 1-g field. With this in mind, five mirror configurations were analyzed for resistance to distortion by gravity. The five configurations are shown in Figure 14. For this analysis, which was accomplished using a computer stress analysis program and the OPD technique described in Appendix C, the mirror is assumed to be supported at the central hub with the optical axis of the mirror vertical as

*For a more complete definition of 1/2 OPD and a description of the method of calculating the 1/2 OPD see Appendix C.

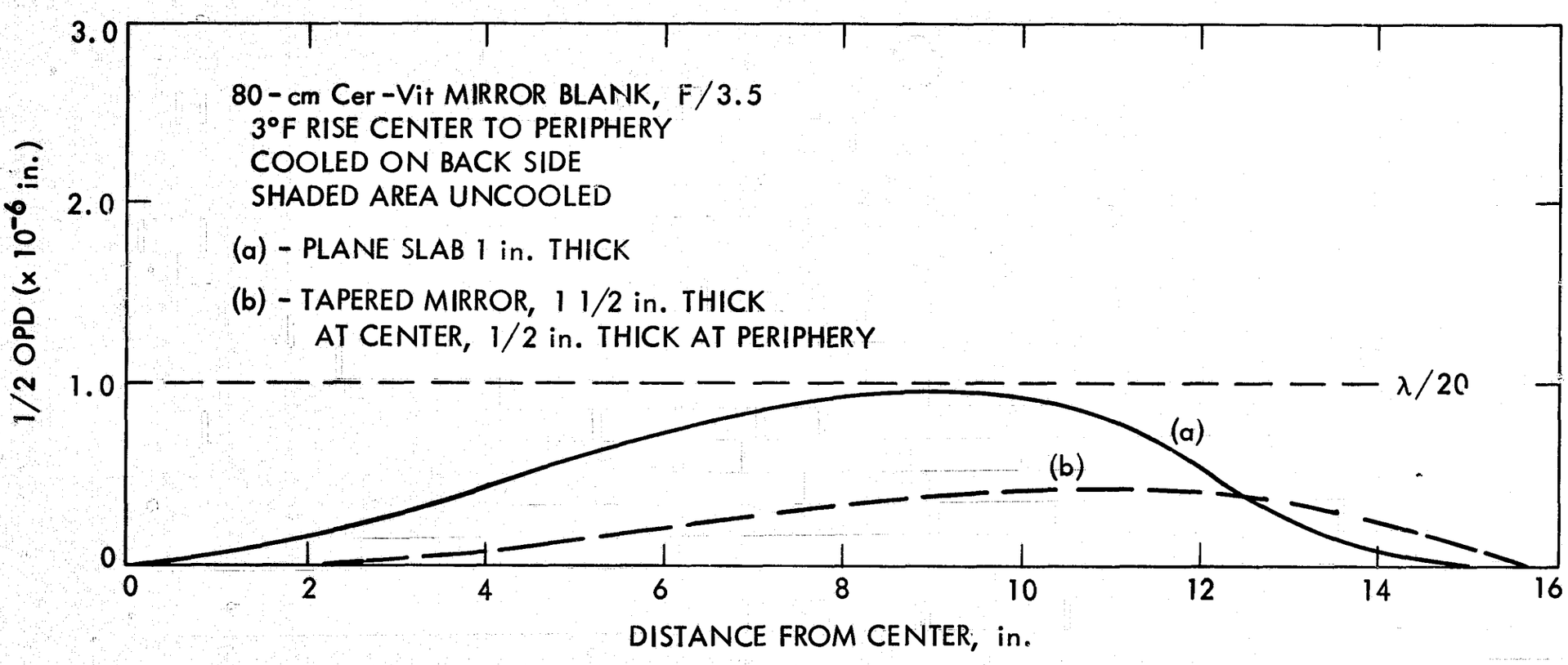

Figure 13. Thermally-Induced Surface Errors From One-Solar-Constant Incident Illumination, Cer-Vit Primary Mirror

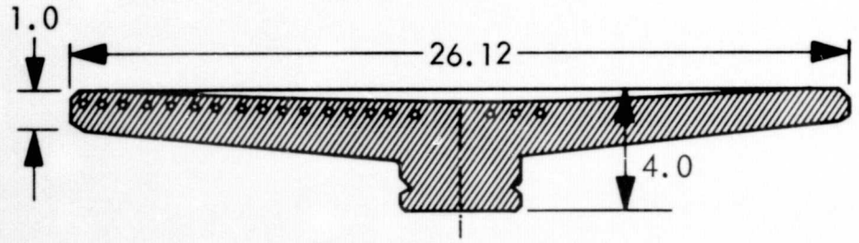

CONFIGURATION No. 1

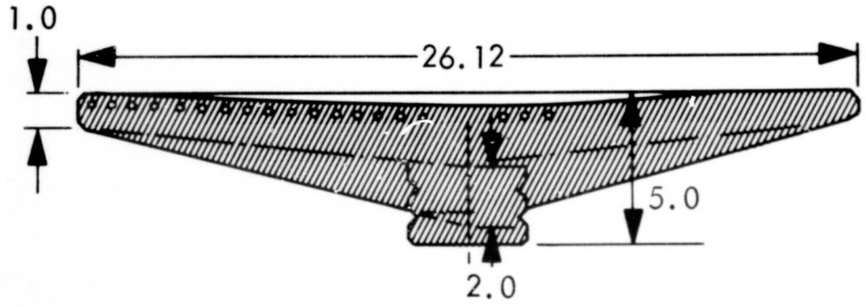

CONFIGURATION No. 4

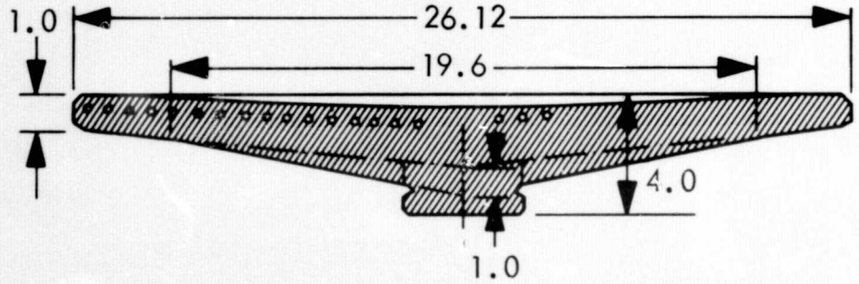

CONFIGURATION No. 2

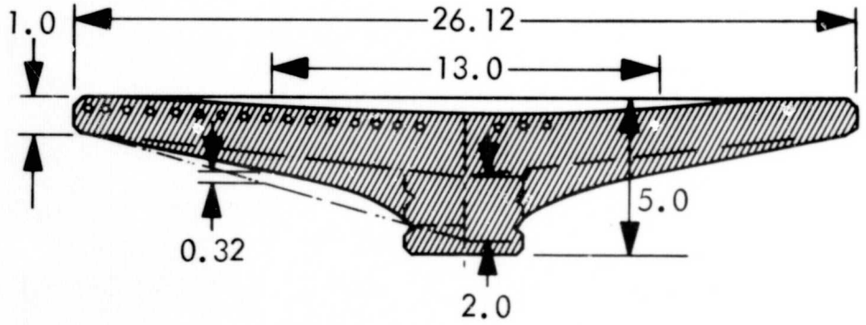

CONFIGURATION No. 5

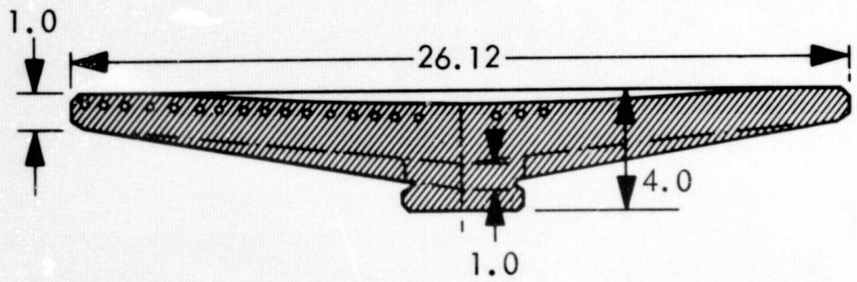

CONFIGURATION No. 3

Figure 14. Five Primary Mirror Configurations Studied

shown in the figure. This is the position the mirror will assume during test and calibration of the telescope on earth. Configuration 1 was analyzed in two positions, with the polished surface up and with the polished surface down. No significant difference in the 1/2 OPD was found. Configuration 5 shows the greatest resistance to gravity distortion (see Table 4). However, very satisfactory results are obtained with configuration 2. It was felt that configuration 2 could be more easily manufactured than configuration 5; therefore, configuration 2 was chosen for the primary mirror design. Since that time it has been pointed out that the sudden change in slope of the back surface of configuration 2 might cause polishing and grinding difficulties as there would exist a discontinuity of stiffness there. Hence, the design has been changed to provide a smooth curve on back of configuration 2 which closely approximates the contour shown.

After selecting a configuration which satisfied the gravity requirements, the next problem approached was that of determining the magnitude of thermal distortion induced into a mirror of this configuration by the incident

Table 4. Distortion Analysis — Gravity SAG

Material	Primary Mirror Configuration	1/2 Optical Path Difference (1/2 OPD)	Focus Change (Inches)
ULE Fused SiO_2	1	$\frac{\lambda}{19}$	0.0051
ULE Fused SiO_2	2	$\frac{\lambda}{185}$	0.0030
ULE Fused SiO_2	3	$\frac{\lambda}{48}$	0.0031
ULE Fused SiO_2	4	$\frac{\lambda}{44}$	0.0023
ULE Fused SiO_2	5	$\frac{\lambda}{250}$	0.0021
Beryllium	5	$\frac{\lambda}{1000}$	0.0005
Beryllium	2	$\frac{\lambda}{909}$	0.0006

solar radiation. Factors affecting the thermal distortion are listed in Table 5.

Item 1 on Table 5, bulk material selection for the primary mirror, was initially approached by computing the thermal distortion index (TDI) for a number of metallic and glass-type materials. The TDI is calculated from

$$\text{TDI} = \frac{\text{thermal coefficient of expansion}}{\text{thermal diffusivity}}$$

where

$$\text{thermal diffusivity} = \frac{\text{thermal conductivity}}{\text{specific heat x density}}$$

The TDI indicates the degree of distortion to be expected from the material under thermal transient conditions. For static thermal conditions, the distortion is simply a function of the thermal coefficient of expansion divided by the thermal conductivity of the material. For the earth-orbiting application intended for the photoheliograph, the thermal transient case is of interest since the source of heat (the sun) will be occulted by the earth during each orbit. The various materials for which the TDI was computed are listed in Table 6. The TDI ranged in value from 4.4 for super invar to 255 for stainless steel. Standard fused silica (Corning 7940) was second highest with a TDI = 49. This high

Table 5. Factors Affecting Thermal Distortion of Primary Mirror

1.	Mirror bulk material selection (thermal expansion coefficient, thermal conductivity, specific heat, density)
2.	Configuration (i. e., mechanical cross-section)
3.	Plane at which heat is extracted from mirror
4.	Direction of flow of coolant in cooling channels (determines radial gradient)
5.	Rate of flow of coolant
6.	Specific heat of coolant

Table 6. Mirror Blank Materials Study

Material	Thermal Distortion			1-g Gravity Distortion Computation
	Thermal Distortion Index Computation	Flat Mirror Blank Thermal Distortion Computation	Complex Mirror Blank Thermal Distortion Computation	
aluminum (5052)	X	X		
beryllium	X	X	X	X
Cer-Vit	X	X	X	(X)
copper	X			
fused silica 7940	X	X		
fused silica 7971 (ULE)	X	X	X	
Invar	X	X		
stainless steel (300 series)	X			
Super Invar	X	X		

Note: X = study performed
(X) = assumed same results as obtained from ULE

value is due to the very low conductivity of glass-like materials. The second lowest TDI value, 7, is shared by Corning Ultra-Low Expansion (ULE) fused silica and Owens-Illinois Cer-Vit, Premium-Select Grade.

The thermal distortions that would be experienced by 31.5-in. diameter,* 1.0-inch thick flat mirror blanks were computed as indicated in column 3 of Table 6. The assumptions for this computation were that the blanks was uniformly illuminated by one solar constant on the front side and that they were uniformly cooled on the back surface. The magnitude of these distortions are shown in Figures 15 and 16. Figure 16 is an enlarged-scale version of the lower part of Figure 15. It is obvious from the figures that ordinary fused silica is not at all satisfactory. Super Invar gives very low thermal distortion, but it has been dropped from consideration because of the large development effort which would be required to qualify it as a suitable mirror material. The distortion for ULE fused silica is not shown in the figures; however, it would closely approximate that of the Premium Select Cer-Vit.

Similar distortion curves were generated for various materials for the secondary mirror (see Figure 17). It is seen that the low-expansion materials, Cer-Vit or ULE fused silica, will give thermal distortions of less than a 1/50th wave.

It will be noted in Table 6 that a number of metals were considered for mirror blank bulk material. Aluminum and stainless steel were eliminated from consideration because of high thermal distortion. Invar and Super Invar both have low thermal distortion characteristics, but are very heavy and of questionable mechanical long-term stability (micro-creep). Beryllium appeared to be the most promising of the metal materials. It is light in weight, and recent work at Batelle Institute indicated that good dimensional stability can be achieved. One serious drawback in the use of beryllium for telescope mirrors is that it must be coated with Kanigen to achieve a suitable amorphous surface for final grinding and polishing. Verbal reports from several optical finishers indicated that Kanigen tends to develop sleeks (small scratches) during the figuring process of aspheric surfaces. (The surface loading by the polishing

*During the early phases of the study, an 80-cm (= 31.5-in.) diameter was assumed for the primary mirror. This was later reduced to a 65-cm (= 25.6-in.) diameter due to space constraints established by the ATM-A cannister configuration.

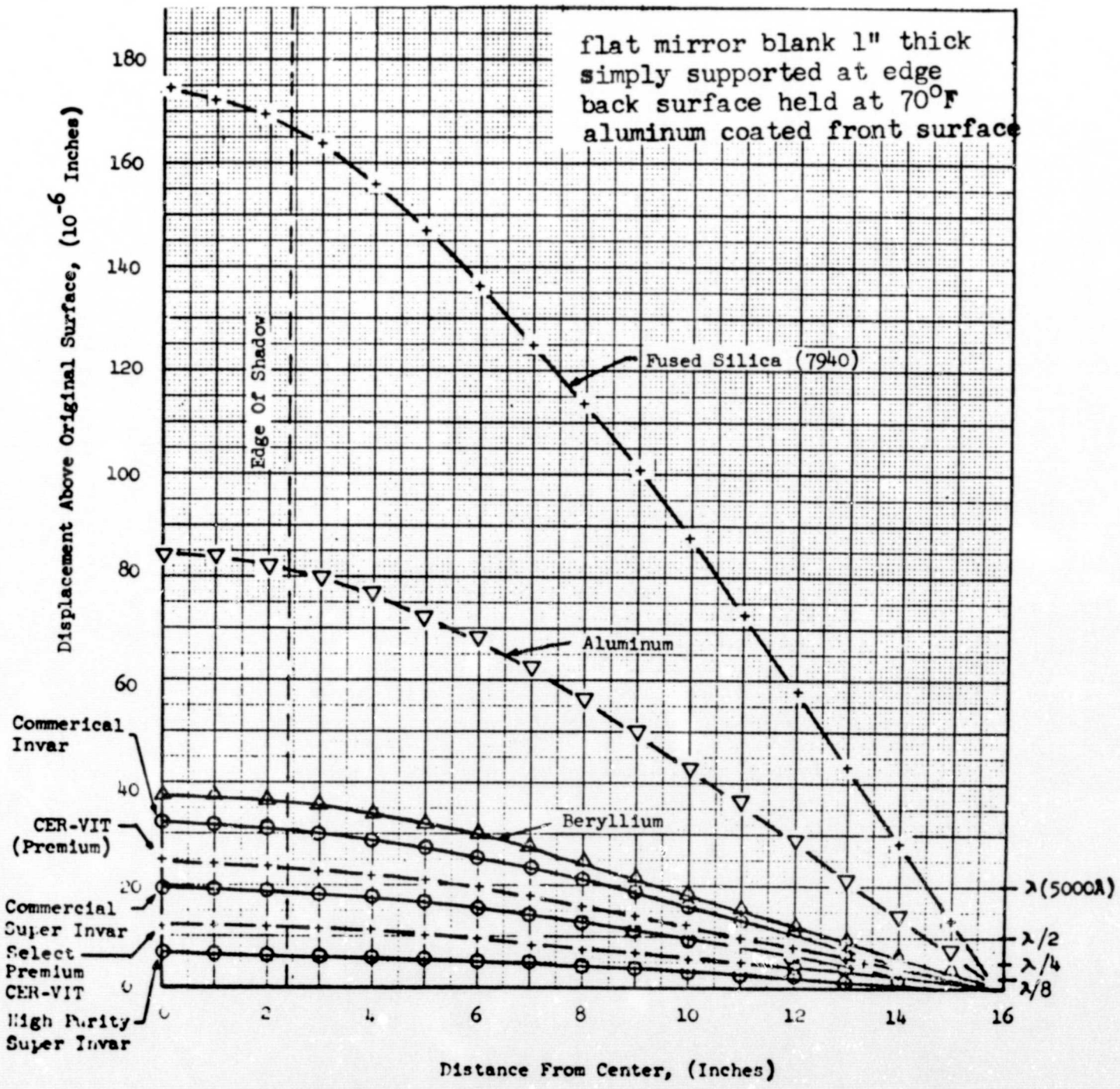

Figure 15. Thermal Distortion of Various Primary Mirror Materials

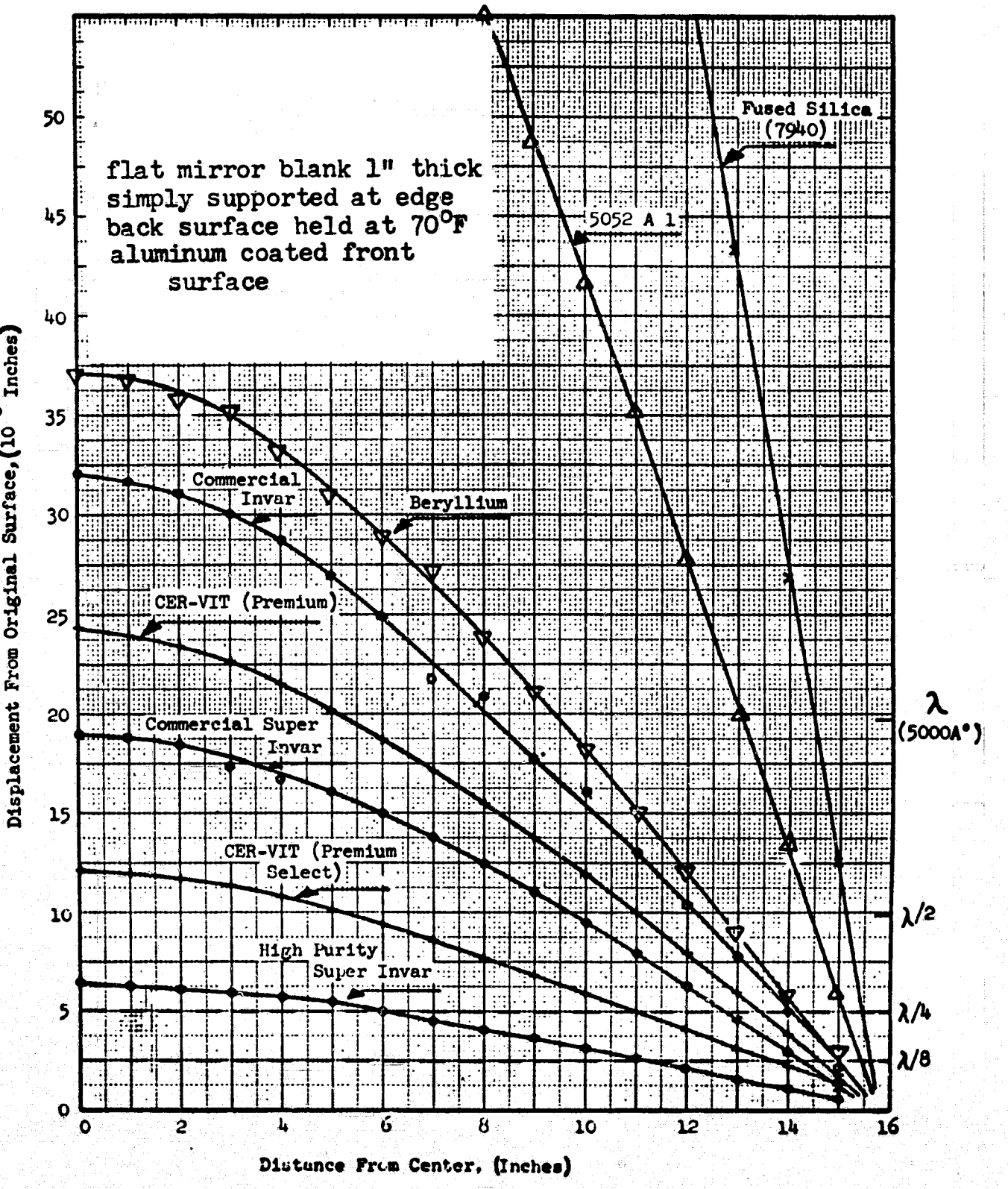

Figure 16. Thermal Distortion of Various Primary Mirror Materials (Enlarged Scale)

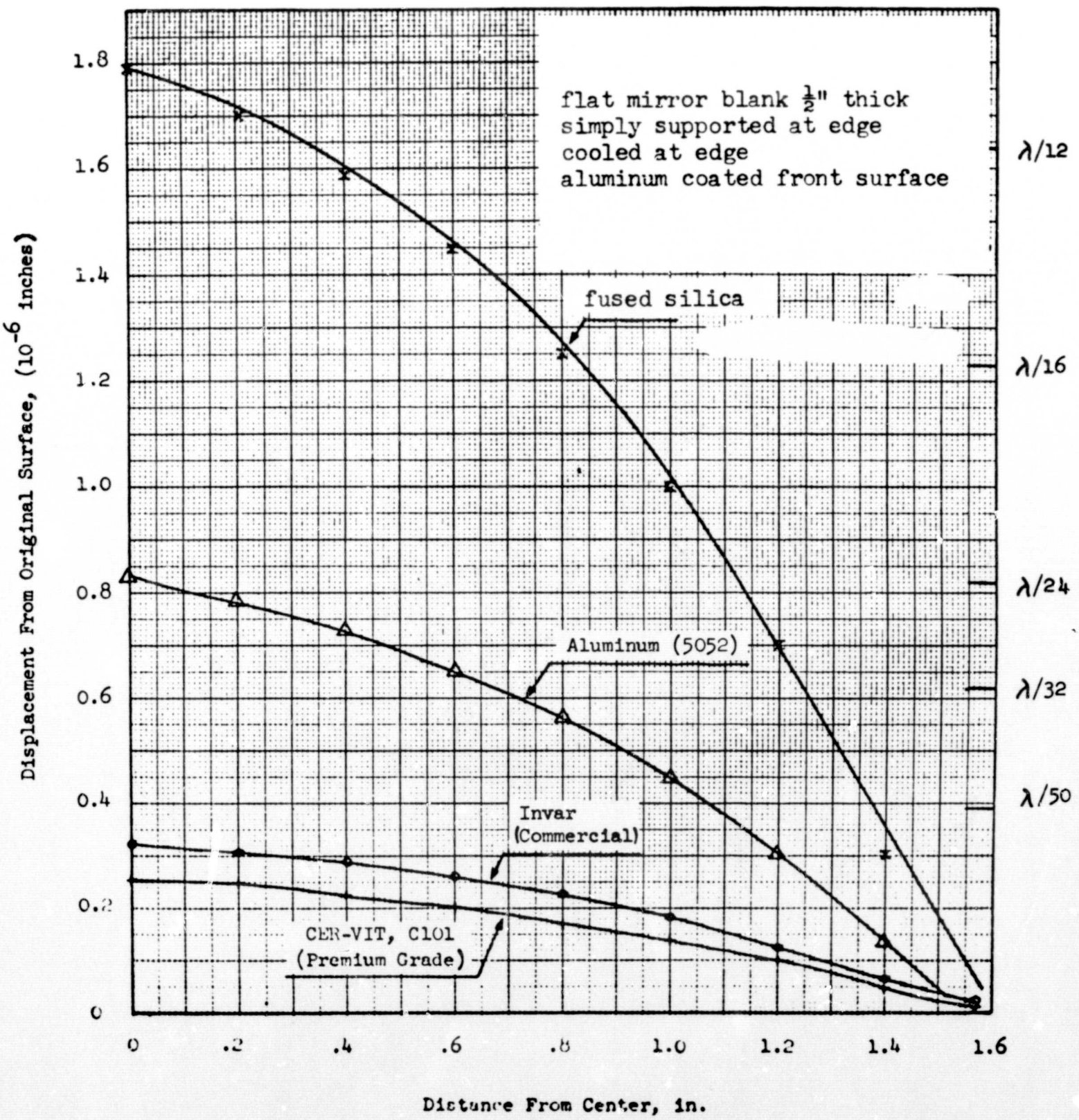

Figure 17. Thermal Distortion of Various Secondary Mirror Materials

tool is smaller for spherical surfaces and the probability of sleeking is less than with aspheric surfaces.) Since the primary mirror is a paraboloid (aspheric), it is felt that the tendency of metal mirrors to develop sleeks is a major problem, especially for an optical system which is intended to work in the ultraviolet region of the spectrum. The optical problem arising from sleeking is that the sleeks scatter light. The degree of scattering is a function of the wavelength of the incident light -- greater scattering at short wavelengths.

Three candidate mirror materials (ULE fused silica, Cer-Vit, and beryllium) were studied in regard to gravity and thermal distortion in a configuration closely approximating the final chosen configuration. The gravity distortion data was presented in Table 4 above for beryllium and ULE fused silica. Cer-Vit, being a glass-like material similar to fused silica will have gravity distortion characteristics similar to that calculated for ULE fused silica.

The thermal distortion for the thermal equilibrium case is given for ULE and beryllium in Table 7. A number of cases of coolant flow conditions were investigated for the ULE mirror in configuration 1 with the result that while turbulent flow yields lower values of 1/2 OPD, laminar flow also gives satisfactory results. Laminar flow requires less pump power and produces less vibration than turbulent flow; therefore, it has been chosen as the flow mode for cooling the mirror. The thermal performance of beryllium in configuration 2 is seen to be unsatisfactory in Table 7.

To determine the thermal distortion characteristics for the transient thermal situation where the mirror is suddenly illuminated by the sun, a computer thermal distortion analysis was conducted for various time periods after the mirror first sees the sun. The resulting data are given in Table 8.

It is seen that the mirror figure appears to remain quite stable during the transient condition, but a focal change of 0.001 in. per 12 minutes occurs. Unless a compensating focal change occurs simultaneously in the secondary mirror, or a compensating expansion of the telescope tube structure occurs, it will be necessary to refocus the telescope approximately every five minutes during operation. A refocusing capability is planned for the telescope.

Table 7. Equilibrium Thermal Distortion Analyses

Material	Primary Mirror Configuration	Thermal Condition	1/2 Optical Path Difference (1/2 OPD)	Focus Change (Inches)
ULE Fused Silica	1	Laminar flow, uniform 70°F coolant temperature	λ/57	0.0008
ULE Fused Silica	1	Turbulent flow, uniform 70°F coolant temperature	λ/78	0.0006
ULE Fused Silica	1	Turbulent flow, 1°F radial gradient rise from outside** to inside*	λ/72	0.0006
ULE Fused Silica	1	Turbulent flow, 1°F radial gradient rise from inside to outside	λ/83	0.0007
ULE Fused Silica	1	Laminar flow, 3°F radial gradient rise from outside to inside	λ/49	0.0007
ULE Fused Silica	1	Laminar flow, 3°F radial gradient rise from inside to outside	λ/67	0.0010
ULE Fused Silica	2	Cooling coils on back surface of mirror back, 3°F rise from inside to outside	λ/20	0.0025
Beryllium	2	Cooling coils on back surface of mirror back, 3°F rise from inside to outside	λ/4	0.0417
ULE Fused Silica	2	Laminar flow, 3°F radial gradient rise from inside to outside	λ/55	0.0007

*Inside – central region of mirror blank

**Outside – peripheral region of mirror blank

Table 8. Transient, Thermal Distortion Analysis

Assumptions: mirror bulk material - ULE fused silica primary mirror configuration #2 3 °F thermal radial gradient from inside to outside		
Minutes of Direct Solar Illumination	Distortion (1/2 OPD)	Change in Focal Length
12	λ/49	0.0011 in.
24	λ/59	0.0010
36	λ/61	0.0009

One of the analyses listed in Table 7 is for the case of a ULE fused silica mirror cooled on the back surface. All of the other analyses for ULE mirrors in the table assume the coolant channels are centered 0.5 inch behind the optical surface. For the ULE mirror in configuration No. 2, laminar flow case, 3 °F rise from inside to outside, the 1/2 OPD is shown by the table to be 1/55th wave for internal cooling channels and 1/20th wave for cooling at the back surface of the mirror. Thus we see that for the thermal equilibrium case, at least, the thermal distortion is approximately only one-third as great when internal cooling is utilized as compared to external cooling on the back of the mirror. For this reason, the mirror blanks are designed to be made from fused silica so that internal coolant channels may be fabricated in the mirror. The method of fabricating internal channels will be discussed later.

Radiation cooling of the mirror blank was also investigated. It is impossible to do effective radiative cooling in the forward direction from the mirror because of the low emissivity of the aluminum reflecting coating at 10 microns wavelength. Since the back side of the mirror has no view of deep space, it is necessary to introduce a cold plate behind the mirror to accomplish radiative cooling of the mirror. It has been calculated that the temperature of the cold plate must be -40 °F in order to maintain the primary mirror at 70 °F. To achieve this low a temperature in the cold plate, it is necessary to have a space-qualified refrigeration system. It is felt that a refrigeration system which could meet the requirements of this application is not within the state of the art.

The mechanical configuration of the mirror blank as delivered to the optical shop is shown in Figure 18. It is seen that the mirror blank is actually comprised of three pieces which are fused together. These are the front (top) plate, the back (bottom) plate, and the hub. The front and back plates are originally separate plates so that the coolant channels may be sandblasted in the back plate before fusing together. The hub is made independently and then fused on strictly to save raw material and grinding time. A very thick piece of fused silica would be required if the back plate and hub were integral. The JPL mirror blank fabrication specification (JPL specification ES504439) calls for a minimum of 90 percent fusion over the fusion joints (i. e., 90 percent of the area of the fusion joint must be fused). There is some concern as to whether the percentage of fusion will decrease during extensive vibration of the mirror during vibration testing and launch of spacecraft. This will be investigated with closely monitored vibration tests at JPL to determine if the anticipated launch environment will cause any change in percentage of fusion.

The mirror blanks are to be fabricated by Corning Glass Works since they are the only source of ultra-low expansion fused silica. The only competitive mirror material from thermal expansion and optical finishing considerations is the crystallized glass product of Ownes Illinois, i. e., Cer-Vit. However, since it cannot be fused, Cer-Vit is not applicable to the fabrication of mirror blanks with internal cooling channels approximating a spiral coil. Adhesive bonding of Cer-Vit pieces together to make a mirror of the type shown in Figure 18 is felt to involve considerable and unnecessary risk. The drilling of radial coolant channels in a solid Cer-Vit blank has been considered. This technique becomes quite complicated in assuring a uniform flow of coolant among the various channels which are fed in parallel.

The processes involved in fabricating the ULE fused silica mirror blanks are shown schematically in Figure 19. Since sag-forming to a refractory mold is not a precision technique, the thickness of the front plate may vary on the finished ground mirror blank by 0. 150 in. Analysis with the computer thermal-distortion program indicates that this variation will be tolerable.

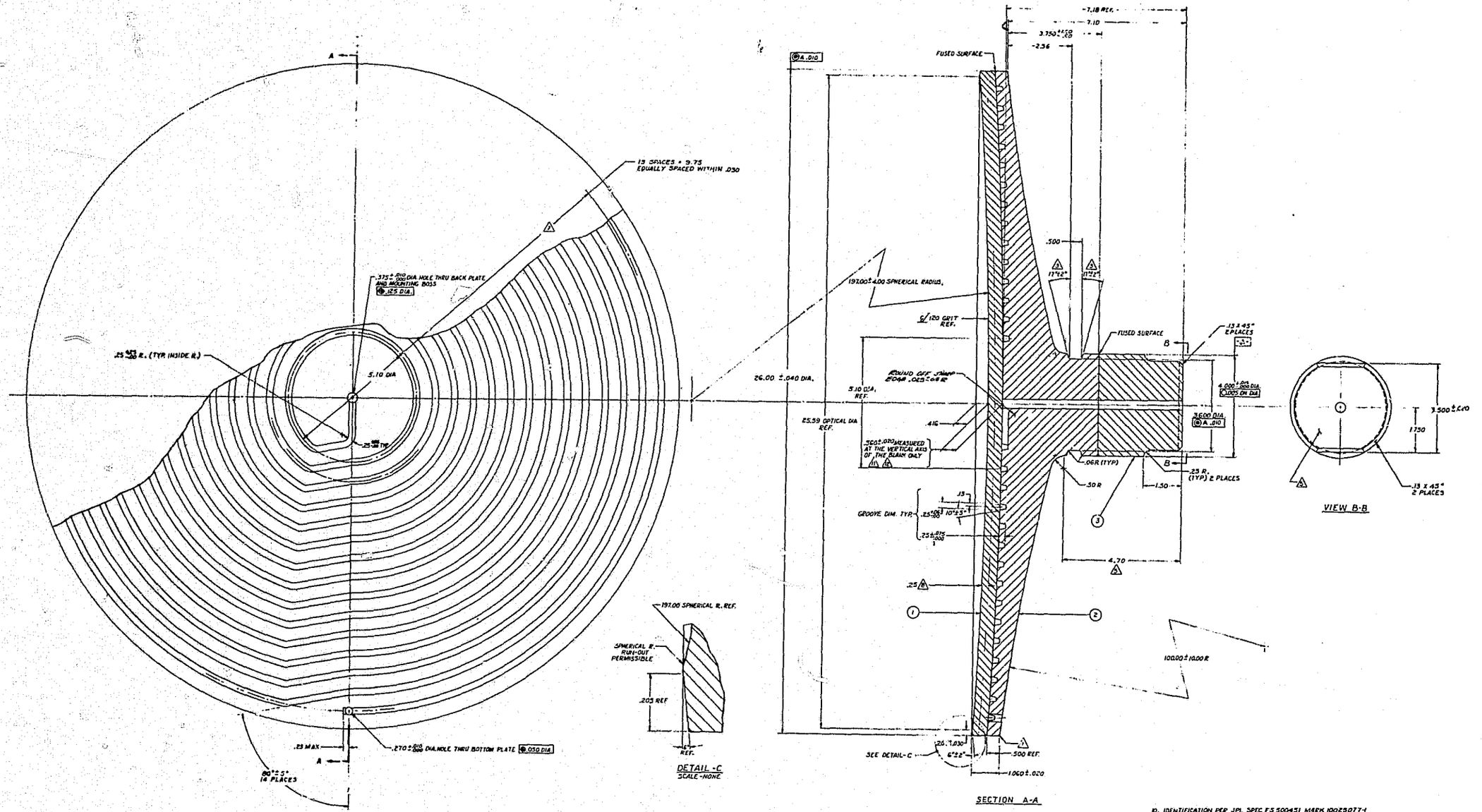

⚠ THE FRONT PLATE THICKNESS VARIATION SHALL NOT EXCEED .150 THROUGHOUT

⚠ THE FRONT CONCAVE SURFACE WILL BE SMOOTH CONTOURED TO THE SPHERICAL RADIUS SHOWN TO WITHIN .040 TO .080 STOCK REMOVAL BY THE FINAL FINISHER WITH A 120 GRIT GROUND FINISH OR BETTER

10. IDENTIFICATION PER JPL SPEC ES 504451 MARK 10025077-1
9. AFTER FINAL GRINDING UNIT SHALL BE ANNEALED AT 1000°C.

⚠ THIS AREA INDICATES THE CRITICAL ZONE AS DEFINED IN JPL SPEC ES 504439 B - PAR. 3.3.2.1.

⚠ GROOVES TO BE SAND BLASTED INTO ② AND FIRE POLISHED PRIOR TO FUSION WITH ①

⚠ ALL SURFACES SHALL BE FINISHED TO A 120 GRIT GROUND FINISH

⚠ SURFACE FINISH OF HUB TO HAVE 300 GRIT GROUND FINISH TO GIVEN LENGTH

⚠ FOR MATERIAL, FINISH, ANNEALING, FUSING AND SAG FORMING SEE SPECIFICATION NO. ES 504439 B

⚠ ANGLES SHALL BE CONSTANT TO WITHIN 0°-30'. INDICATED TOLERANCE APPLIES TO FEATURE OF ANGLE ONLY

2. MACHINED FILLET RADIUS .31-.05

⚠ REMOVE ALL BURRS AND SHARP EDGES .010 MAX

NOTES: UNLESS OTHERWISE SPECIFIED:

Figure 18. Mirror, Primary, Blank, Photoheliograph – JPL Drawing 10025077

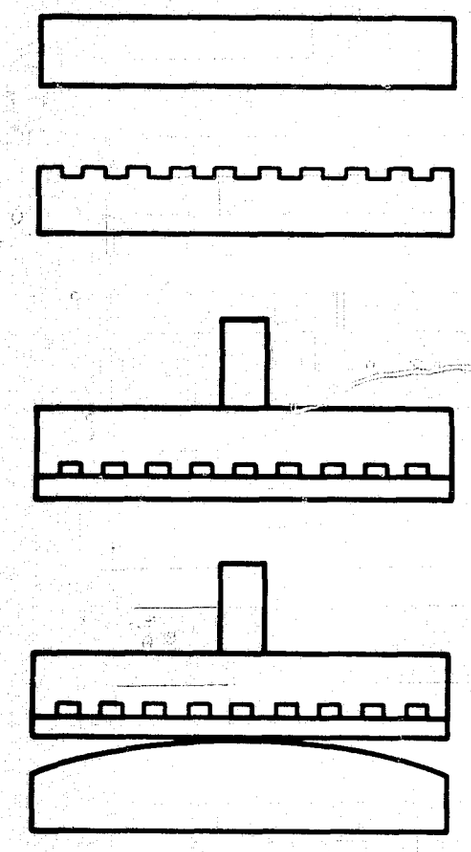

ROUGH BACK PLATE

SANDBLAST CHANNELS IN BACK PLATE

FUSE FRONT PLATE AND HUB TO BACK PLATE
(FUSING TEMPERATURE 1600°C)

SAG TO REFRACTORY MOLD (JUST BELOW 1600°C)

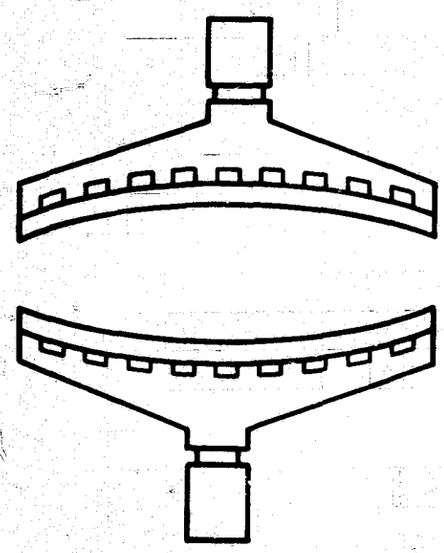

GRIND BACK PLATE AND HUB TO DIMENSIONS

GRIND FRONT PLATE TO PROPER CURVATURE,
ANNEAL AT 1000°C

Figure 19. Fused-Silica Mirror Blank Fabrication Procedure

The surface errors resulting from individual coolant loops have been analyzed. The localized thermal distortion due to the presence of individual loops in the mirror amount to only 1/2000th of a wave. The distortion of the surface resulting from the 16 psi fluid pressure in the coolant channels is computed to be 1/500th of a wave. The coolant fluid will be an 80 percent methanol, 20 percent water solution.

Figure 18 shows a groove around the hub of the mirror. A two-piece, precision-fit Invar ring will be affixed in the groove and will provide the basis for attachment of the mirror mount to the mirror during telescope operation in orbit and on the ground. During launch phase (and vibration testing), a series of "launch locks" will engage the mirror around the periphery to provide additional support. These will be retracted after launch so that no strains are induced into the mirror by the support system.

Filters. Spectral intervals of interest for the solar telescope include ultraviolet in the 1500-2500Å wavelength region, white light centered at 5000Å and the hydrogen-alpha line at 6563Å. A system of beam splitters in the exit beam of the telescope will direct light simultaneously through separate filters to the appropriate cameras (see Figure 20). A brief description of the filters and their operating characteristics is presented in the following paragraphs.

Both the Lyot type birefringent filter and solid Fabry-Perot interference type filter are being considered for the hydrogen-alpha line. It is necessary that the filter have a 0.5Å band pass centered at 6563Å with provision for tuning ±5.0Å.

The Lyot filter consists essentially of a series of birefringent crystal plates separated by blocking polarizers. Only those wavelengths for which the difference in optical path between two polarizers is an even number of half waves will be completely transmitted. Transmission for the entire filter is the product of the transmissions of each polaroid-crystal-polaroid sandwich. Modifications are employed to optimize cone angle and achieve some tunability. Thermal effects are critical and must be carefully controlled. Commercial versions of the Lyot filter are available from the Zeiss and Bernhard Halle firms in Germany. Certain features such as electronic temperature control and shock mounted calcite crystals make the latter attractive for space flight

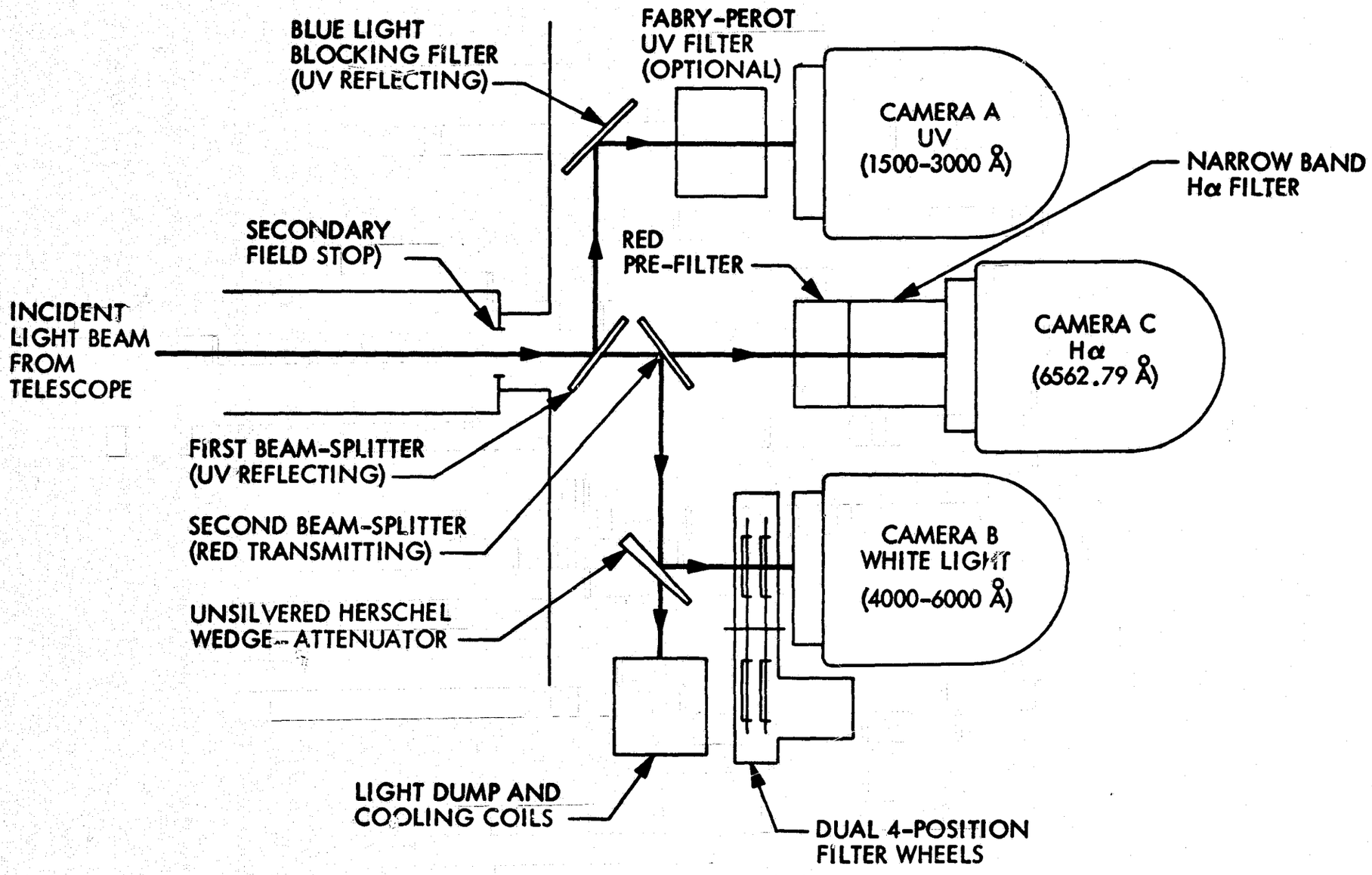

Figure 20. Photoheliograph Camera Cluster

application - although the useful shift range is only +1Å. Peak transmission of the Halle is 10-14% and, of the Zeiss, approximately 10%.

The solid etalon Fabry-Perot filter is also being considered for isolation of the hydrogen-alpha line. It is relatively simple, very rugged and exhibits little drift with temperature. Present Fabry-Perot filters developed by Perkin Elmer have a 0.55Å bandwidth with 88% transmission in an f/40 optical system. Temperature drift is 0.05Å per degree centigrade. Certain modifications, however, must be added to provide for tunability. Pressure and temperature scanning as well as tilting of the filter have been suggested.

Both transmitting and reflectance type interference filters have been investigated for the ultraviolet region. The former is problematical due to the difficulty in finding suitable high-index material which is transparent at short wavelengths. A better possibility is the construction of a simple reflection interference filter on the final diagonal flat directing light into the ultraviolet camera. The filter consists of a transparent layer deposited on a reflecting surface and covered by a semi-reflecting metal film. Several varieties of this type of filter have been described in the literature. W. G. Tifft at the University of Arizona has constructed a simple three-layer coating consisting of opaque aluminum, MgF_2 and semi-transparent aluminum. This produces a filter with high (80%) reflectivity bands centered at 1300 and 2600Å. They are approximately 250Å and 700Å wide respectively. Through the use of a thinner layer of MgF_2, it should be possible to shift the broader peak to a more applicable wavelength, say 1800Å.

OPTICAL PERFORMANCE

This section will discuss the optical performance expected from the telescope design. The ideal performance which would result from the optical system in perfect alignment and condition will be specified. Realizing, however, that nothing is perfect, an attempt is made to describe the anticipated optical performance under practical conditions of the mission.

Unperturbed Optical Performance. The Rayleigh resolution limit for a 65-cm aperture is simply given by

$$\theta = 1.22\ \lambda/D = 9.38 \times 10^{-7} \text{ radian} = 0.193 \text{ arc-second}$$

where

θ = angular subtend of two points just resolved

λ = wavelength of light at which the measurement or calculation is made = 0.5 micron = 5×10^{-8} cm

D = diameter of the aperture = 65 cm

In terms of linear resolution, the Rayleigh limit is

$$\text{linear resolution} = \frac{1 \text{ line-pair}}{\text{focal length} \times \text{angular resolution}}$$

$$= \frac{1 \text{ line-pair}}{(3.250 \times 10^{4} \text{ mm})\ (9.38 \times 10^{-7} \text{ radian})}$$

$$= 32.8 \text{ line-pair/mm}$$

In the event the telescope line of sight moves relative to the scene being photographed during the exposure time, the image will be smeared and a lower resolution value will result. Although the telescope is fairly stable while in orbit, the long focal length (3.250×10^{4} mm) makes it very sensitive to small angular motions. The yaw and pitch jitter rate expected of the ATM cannister in orbit is one arc-second per second of time. The roll jitter rate is expected to be on the order of one arc-minute per second of time. The combined effects of image motion and exposure time upon resolution are discussed in Appendix D and are presented here in Table 9.

The loss of resolution in Table 9 is that due to pitch and yaw jitter. The loss due to roll is only 1/20th as great. The need for fast exposure times is clearly seen. While this may seem a trivial matter when photographing the sun, it must be remembered that there is not a lot of energy available from the sun in the 1500-3000 Angstrom region and in the hydrogen-alpha line. The

Table 9. Loss of Resolution Due to Image Smear

Exposure Time (seconds)	Resolution (line-pair/mm)	Resolution (Arc-seconds)
0	32.8	0.193
0.025	29.0	0.219
0.050	26.2	0.242
0.075	23.6	0.269
0.100	21.7	0.292

ultraviolet output of the sun drops very rapidly below 4000 Angstroms. The shortage of radiation at the hydrogen-alpha line comes not from lack of emission at this wavelength, but from the small band-pass (0.5 Angstroms) or less of the hydrogen-alpha filter.

Since the field of view is very small (3.2 arc-minutes), the Seidel aberrations of the telescope will be very small if the system is in proper alignment. The chromatic aberrations will, of course, be zero since the design is an all-reflecting system with no components having optical dispersion. Tangential coma at the corners of the field will be only about 0.007-arc-second. This will amount to less than 4 percent of the limiting resolution and will certainly be insignificant. Based on computer spot diagrams, the curvature of field has been determined to be about 1.0 mm (0.040 in.) in magnitude and, at the edge of the field, curves away from the secondary mirror. Computer ray tracing also shows the field distortion to be only 6.0×10^{-4} percent (5.7×10^{-4} arc-seconds) at the corners of the field.

If we define the maximum tolerable focal shift as one which produces an optical path difference not exceeding one Rayleigh limit ($\lambda/4$), then the equation for the depth of focus (DOF) may be written after Conrady (Ref. 1) as follows:

$$DOF = \pm \frac{\lambda}{2N' \sin^2 U'_m}$$

where

N' = refractive index of the medium in which the image is formed

U'_m = angle at which the extreme marginal ray arrives at the focus

For a reflecting system working in vacuum (or, for all practical purposes, in air), $N' = 1$. For f-numbers greater than 10, $\sin U'_m = 0.5/\text{f-number}$. At f/50, $\sin^2 U'_m = 10^{-4}$. Thus, for the f/50 Gregorian operating at a wavelength of 5000 Angstroms, the depth of focus will be 2.5 mm on either side of the focus. This is 2.5 times greater than the tolerance required by the field curvature.

Prediction of the optical performance of the photoheliograph is accomplished through the use of the Aerospace Corporation's PAGOS (Program for the Analysis of General Optical Systems) optical computer program. The great value of the PAGOS program lies in its versatility - it will provide the following data on any optical system that is provided as input:

a. The Seidel contributions of each surface and the Seidel sums

b. Full-field ray trace through the system

c. Spot diagrams for points images in or near the focal plane across any specified field of view

d. Diffraction-based modulation transfer function (MTF) data and plots for any specified point in the field of view.

With the exception of the Seidel calculations, these outputs can be provided for the system under conditions of misalignment of the elements and certain types of periodic surface errors. The program is being presently expanded at JPL to include a capability for computing the Strehl ratio for any image point in the field of view. This will be done by computing the MTF volume at an image point and dividing this volume by the MTF volume of a diffraction-limited optical system operating at the same image point. The ratio of these two volumes gives the value of the Strehl ratio (Ref. 2).

$$\text{Strehl ratio} = \frac{\text{volume under 3-dimensional MTF curve}}{\text{volume under 3-dimensional MTF curve of aberration-free system}}$$

The above equation is not the definition of the Strehl ratio, but provides a method of calculating the ratio if the MTF is known.* The advantage of using the Strehl ratio as an evaluation criteria lies in the fact that it provides a single-valued function which can describe the performance of the optical system. It is true that the Strehl ratio does not convey as much information about the optical performance as the MTF. On the other hand, unless the nature of the target is known quite thoroughly in advance, the spatial frequency information contained by the MTF is of little value.

The MTF for a diffraction-limited optical system is given by (Ref. 3)

$$\text{MTF} = \frac{2}{\pi} (\phi - \cos\phi \sin\phi) (\cos\theta)^k$$

where

$\phi = \cos^{-1} (\nu\lambda \text{ f-number})$

ν = spatial frequency in cycles/mm

λ = wavelength in mm

θ = half field angle

k = 1 for radial lines and 3 for tangential lines

This curve is plotted in Figure 21 for the on-axis image of an f/50 system. Also plotted are the MTF curves for an f/50 telescope with a 0.2 and a 0.5 central obscuration. The need for keeping the central obscuration small is obvious. While the central obscuration has the effect of "peaking" the high frequency transmission of the optical system, the loss in the middle frequencies more than offsets the gains except in very specialized applications where only high spatial frequencies are important.

Perturbed Optical Performance. For the purposes of this discussion, perturbed optical performance is defined as that performance given by the optical system in the presence of misalignment of the optical elements and/or imperfections in the contours of the reflecting surfaces (surface errors).

---

*For further discussion on Strehl ratio and MTF, see Appendix A.

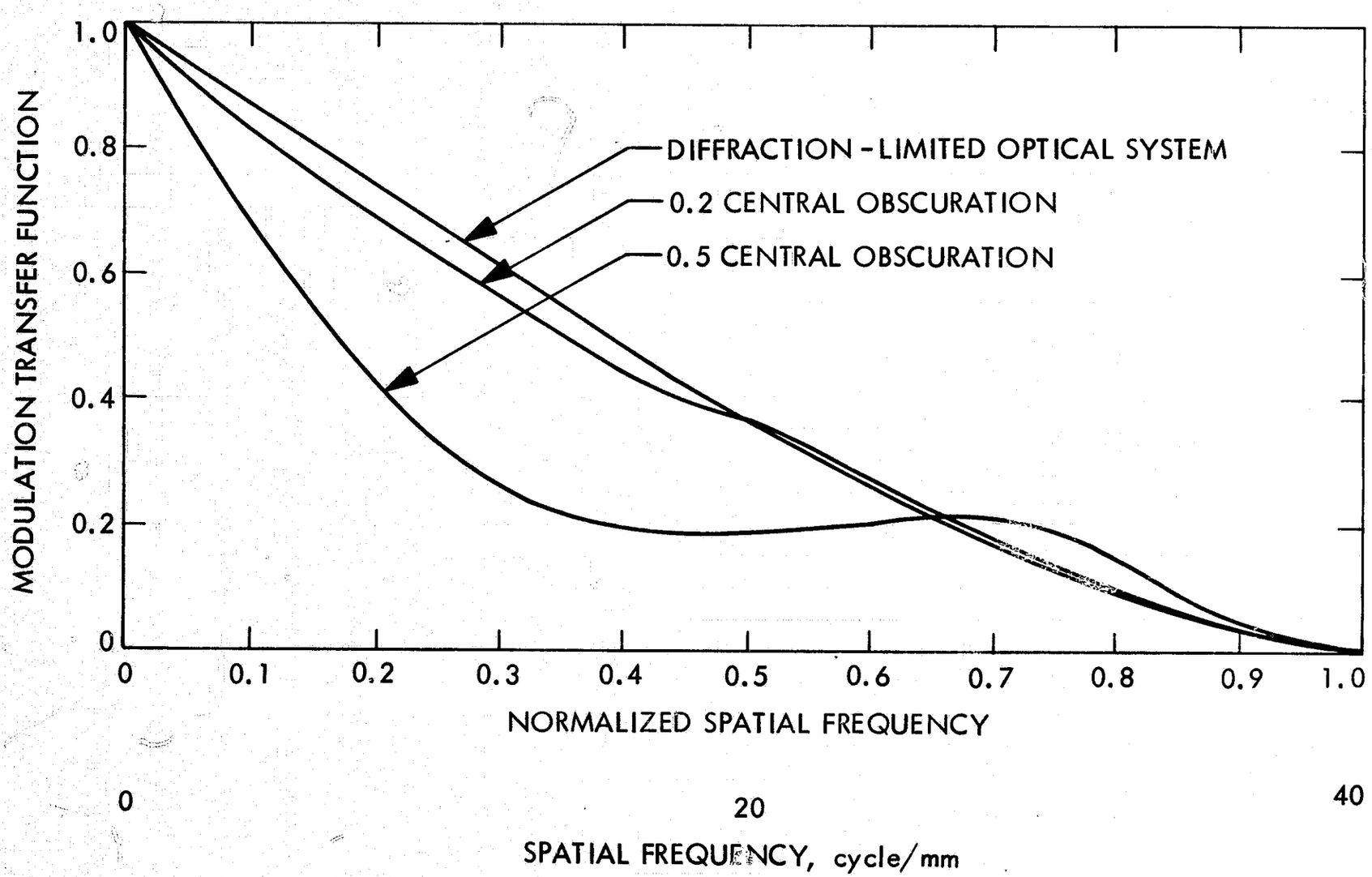

Figure 21. MTF Curves for Diffraction-Limited Optical System and Systems with Central Obscuration

The three types of misalignment are:

a. Spacing – errors in the relative spacing between the primary and secondary mirrors and between the secondary mirror and the image detection plane

b. Translation (decentration) – the condition which exists when the axes of the several optical elements are parallel but not coincident

c. Tilt – nonparallelism of the axes of the optical elements

All of the types of misalignment can be experienced simultaneously to a greater or lesser degree. Indeed, it is impossible to conceive of any of the alignment errors being absolutely zero.

A study has been made on the effects the three types of misalignment have on the optical performance of the Gregorian telescope. The objective of this study is to determine tolerance levels for misalignment. At the beginning of the study it was thought that evaluation of the spot diagram as a function of misalignment would serve as a criteria for establishing tolerance levels. It was felt that a misaligned condition was tolerable as long as the spot diagram size did not exceed the diffraction blur circle diameter (diameter of the central Airy disk) calculated for the instrument; i.e., 61 microns. This proved to be wrong. It was found that, if the spot size was allowed to become as large as the diffraction blur circle diameter, the MTF had degenerated significantly. In retrospect, the reason for this is quite obvious. Computer spot diagrams do not take into account diffraction effects. However, the performance of an essentially diffraction-limited optical system is governed largely by diffraction. Therefore, computer spot diagrams are of little value in analyzing the performance of an optical system operating near the diffraction limit.

A meaningful criteria for the determination of alignment tolerances can be established through the study of the MTF and the Strehl ratio as a function of misalignment. This may be done by computing the Strehl ratio on the basis of the volume under the MTF curve and setting the absolute minimum acceptable value of the Strehl ratio as 0.8 (Appendix A gives 0.793 as the Marechal lower limit on the Strehl ratio). The manner in which the misalignments add together in reducing the Strehl ratio has not yet been determined, but can be investigated with the PAGOS program as modified to compute Strehl ratios. After

this has been done, it will be necessary to assign limits to the contribution each perturbation makes to the degradation of the Strehl ratio.

The effect of spacing error is to defocus the image. To a small extent, spacing errors can be compensated by refocusing the camera. Also, the depth of focus will accommodate a very small spacing error. For the f/50 Gregorian, a spacing error between the primary and secondary mirrors of 0.001 cm can be tolerated without refocusing. If the camera is refocused, a mirror spacing error of 0.1 cm is tolerable. This amounts to changing one spacing (secondary mirror to image recording plane) to accommodate error in another spacing (primary to secondary mirror). These spacing effects were studied through the use of MTF curves generated with the PAGOS program. Using the MTF data from the computer run, the Strehl ratio was hand-calculated to be 0.86. Accepting a lower bound for the Strehl ratio of 0.8 it is seen that the spacing tolerance could be increased somewhat if spacing were the only misalignment. This, of course, is not the case.

Tilt and translation misalignments both produce comatic images in the focal plane. The resultant point spread function is not symmetrical; therefore, a single MTF curve cannot describe the imaging capability of an optical system experiencing either or both of these misalignments. However, MTF curves generated for the comatic image in two orthogonal directions in the image plane do not differ greatly. This is, perhaps, due to the higher concentration of light energy in the small end of the comatic image. If two Strehl ratios are computed, one on the basis of each of the two orthogonal MTF volumes, the average value of these two ratios can be assumed to fairly well represent the Strehl ratio of the comatic image. It will be on this basis that further study of the alignment tolerances of the Gregorian telescope will be pursued.

Estimates of the misalignment tolerances have been made from inspection of the degradation of the MTF curves. An example of the change in MTF as a function of translation (decentering) of the secondary mirror relative to the primary is shown in Figure 22. Preliminary tolerance levels are given in Figure 23. These levels must all be lowered as they do not take into account image degradation arising from other sources. Realistic values can be obtained after the tolerance study based on computer-generated Strehl ratios has been completed.

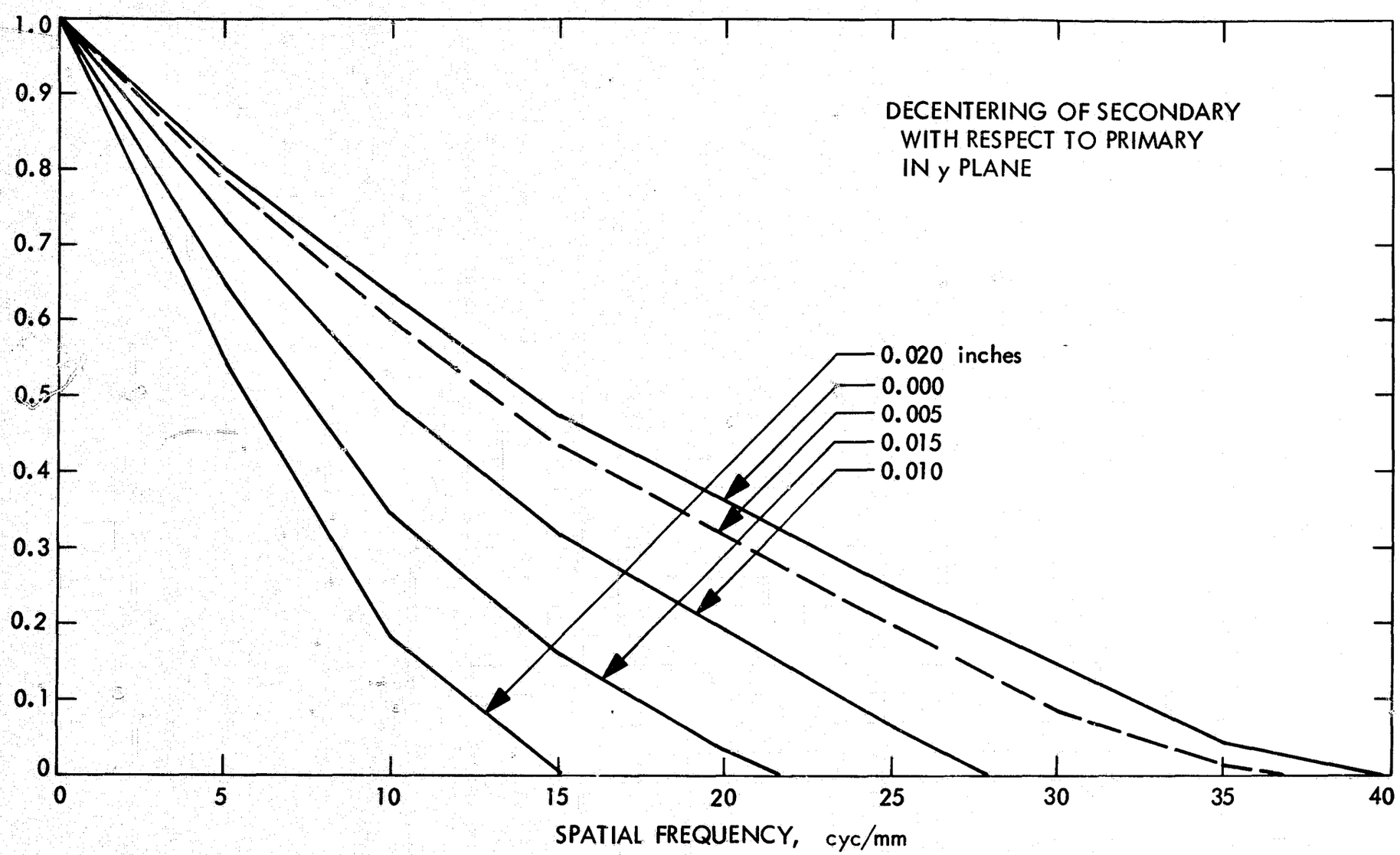

Figure 22. Degradation of MTF as a Function of Decentration

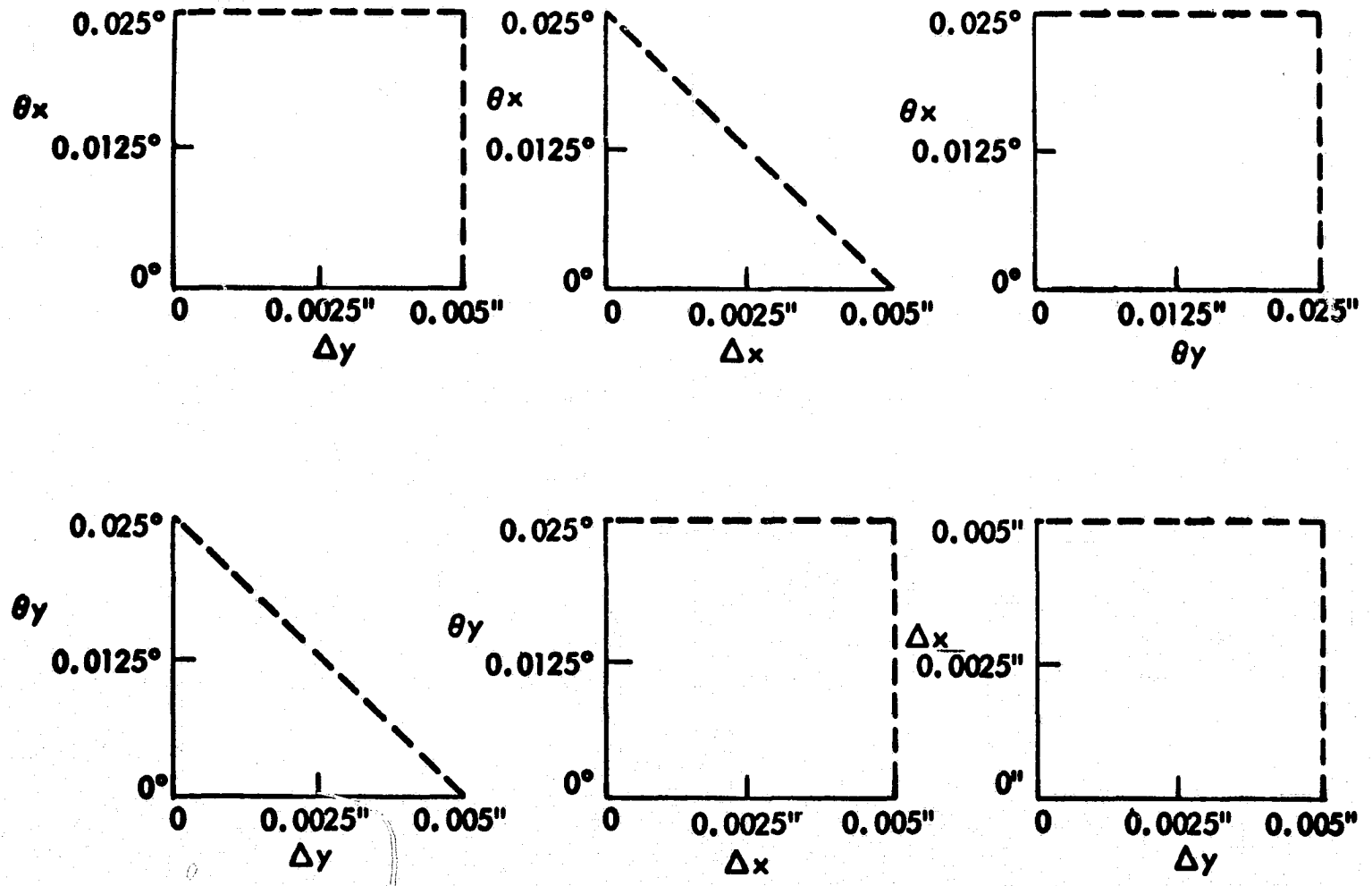

NOTES:

1. Area encompassed represents allowable misalignments (assumes no surface distortion of mirrors or spacing errors).

2. Tolerances are acceptable over a 2-cm radius field and for a defocussing of ±0.18 cm at the focal plane.

3. Thetas represent tilt and deltas represent translation of the secondary mirror axis with respect to that of the primary mirror.

4. X and Y are two arbitrary, orthogonal axes in a plane perpendicular to the primary mirror axis.

Figure 23. Preliminary Misalignment Tolerances Assuming No Other System Perturbations Except Defocusing

In addition to the image degradation introduced by misalignment and defocusing, the telescope will experience further degradation due to surface errors; i.e., the departure of the actual mirror surface from the proper mathematical form. As an example, the primary mirror should be exactly a paraboloid, but may depart from a true paraboloidal form by something like a millionth of an inch. The secondary mirror should be a true ellipsoid and the remaining mirrors, true flat planes. In all cases, the tolerance is in the order of a millionth of an inch or less.

The surface errors may be classified as two types: gross systematic surface errors and small-scale random errors. The first type consists of thermal distortions, gravity distortions, and manufacturing tolerances. The second type result from manufacturing tolerances and inhomogeniety in the mechanical characteristics of the material. The analysis of the image degradation of the two types is performed by different methods (see Appendix E). These methods, unfortunately, yield answers in different units. For the gross systematic error, the analysis yields results in terms of the relative amount of energy which falls into the central disk of the diffraction pattern compared to that which goes into the diffraction rings. In the case of random errors, the effect on the Strehl ratio is analyzed. For wavefront errors of less than 1/4 wavelength, one can argue that the relative amount of energy in the central disk should relate quite directly to the Strehl ratio. The energy is represented by the volume under the diffraction pattern curve whereas the Strehl ratio is a measure of the relative height of the curve. For wavefront errors of 1/2 wave or less, the width of the central disk is essentially constant (Ref. 4). Therefore, to a first approximation, the volume under the diffraction curve will be directly proportional to the height of the peak of the curve for small wavefront errors. That is, the energy relationships derived from systematic wavefront error analysis can be made to relate to the Strehl ratio derived from random wavefront error considerations.

From the data generated in Appendix E, we see that degeneration of the Strehl ratio down to 0.8 (Rayleigh limit) occurs if the gross systematic surface error is 1/8th wave (1/4-wave wavefront error) or if the random surface errors of the four mirrors in series are on the order of 1/54th wave. Only the four mirrors "upstream" in the optical system are considered to contribute seriously to the wavefront error analysis. These are the primary, secondary, and two periscope mirrors near the front end of the telescope. The beam splitters and

optical filters are located near the focal plane (Figure 20) and, consequently, have little optical power. This is because the optical lever from the beam splitters and filters to the focal plane is relatively short. A striking example of the insensitivity of an optical system to wavefront distortions near the focal plane is the effect produced by a piece of ground glass. Such glass is extremely rough on a wavelength scale; yet, if placed at the focal plane of a lens, it will transmit an image. However, when placed distant from the focal plane, no image is passed.

Quantitative data is to be obtained on the actual degradation caused by surface errors of the beam splitters and filters using the PAGOS computer program. Should the effect be significant, 1/100th wave surfaces will be specified for all flat mirrors. Flats of this accuracy and better are available commercially, typically for use in Fabry-Perot resonators.

Optical Performance Budget. Based on practical considerations, it does not seem that the minimum acceptable Strehl ratio for the photoheliograph can be set at a higher limit than 0.8. This corresponds to optical performance at the Rayleigh limit where 32 percent of the light energy is scattered into the diffraction rings and 68 percent enters the central disk. Conrady describes performance at the Rayleigh limit as follows:

> The loss in contrast is thus decidely considerable and may render delicate detail invisible, whilst there is no loss of resolving power for strongly marked detail. (Ref. 5)

Those factors which contribute to the degradation of the Strehl ratio are the tilt and translation misalignments, spacing misalignment, surface errors (including thermal and gravity distortions) and defocusing (inaccurate focusing), Each of these sources of error individually can be kept small enough so that their contribution to Strehl ratio degradation is less than the -0.2 total allowed. It is the sum of their contributions, however, that determines the overall optical performance, and maintaining the sum below the -0.2 level represents a considerable technical challenge but does not seem impossible. At the present it is not known whether or not the contributions from all of these sources of error add linearly. A study of computer generated MTF curves for a single misaligned and two defocused conditions has revealed an interesting phenomenom. The MTF degradation due to the combination of misalignment and defocus is slightly

less than the sum of the loss incurred in going from a properly aligned and focused condition to a misaligned condition plus the loss in going from the proper condition to the defocused condition. Thus, MTF degradation from defocusing and misalignment does not add linearly, but at a somewhat lesser rate.

The summing of image degradation from combinations of the various error sources will be studied in more detail on the basis of Strehl ratio using the PAGOS program. Until the summing characteristics are understood it will not be possible to budget performance degradation allotments to the various error sources. Such budgeting will also have to consider the practical tolerance limits which can be put on the individual error sources.

INFLIGHT ALIGNMENT AND FOCUS CAPABILITY

Because of the nearly linear summation of misalignment and defocusing degradations of the image, it is necessary to keep alignment and focusing errors to an absolute minimum. Alignment tolerances will have to be kept to approximately 0.003 in. of translation and 0.0125 degrees of tilt. A structure the size of the photoheliograph cannot be kept aligned within these tolerances through the launch phase of the mission. It is also quite likely that thermal fluctuations during the orbital phase of the mission may distort the telescope structure beyond these tolerances. The need for inflight alignment and focus capabilities is obvious.

An alignment system has been designed for the photoheliograph and is described in a concurrent report.* It has been determined that it will be necessary for the alignment sensor to work in two modes: one for the detection of translation alignment and one for tilt alignment. Analysis of the design indicates that the sensor will be able to detect alignment errors an order of magnitude smaller than the tolerances given in the previous paragraph.

For the purpose of alignment, the telescope is mechanically divided into two blocks, one of which is to be aligned with the other. Each block is considered to be internally rigid. The reference block contains the primary mirror, the alignment sensor, and the data recording cameras. Mounting rigidity

*See the Introduction section of this report for a list of concurrent reports containing supplemental information.

between the primary mirror and the alignment sensor is very important while the accurate positioning of the cameras is of lesser importance. It matters little whether or not the optical axis intersects exactly the center of the camera format. The movable block contains the secondary mirror, the field stop (heat-stop mirror), and the two periscope mirrors. It is essential that these all be maintained rigidly fixed with respect to each other. The alignment sensor in the reference block detects the translational position of the movable block through the simple expedient of using a bore-sight telescope to observe a tiny light source located near the center of the secondary mirror (see Figure 24). A rotating knife edge in the focal plane of the boresight telescope modulates the amount of light received on a photo tube located behind the focal plane if the image of the light sources is not exactly centered on the axis of rotation. The amplitude and phase of the modulation yield information on the amount and direction of the translation misalignment. This information may be displayed on a PPI indicator for the astronaut to use in realigning the system. Realignment is accomplished by actuating four small motor-screw combinations which determine the transverse locations of the movable block relative to the optical axis of the primary mirror.

Tilt misalignment will be detected using a modified autocollimation technique (Figure 25). A beam of light originating at the alignment sensor will be reflected by a small, off-axis mirror segment located at the center of the secondary mirror. After reflection by the primary mirror, the beam is once again reflected by the off-axis segment back to the alignment sensor. In order to pass the total beam through the small aperture in the heat-stop mirror, spherical reflecting surfaces will be used on the small, off-axis segment of the secondary mirror and the central 2.6 inches of the primary mirror. The autocollimator beam path between the primary and secondary mirrors lies within the shadow zone of the secondary mirror cell. Between the secondary mirror and the alignment sensor, the autocollimator beam as well as the boresight telescope line of sight are three degrees off axis with respect to the photoheliograph optical axis. Thus, the alignment sensor may be used while the telescope is pointed at the sun.

A full-scale model of the alignment system is being built to test the theory and sensitivity of the design. The photoheliograph primary and secondary mirrors

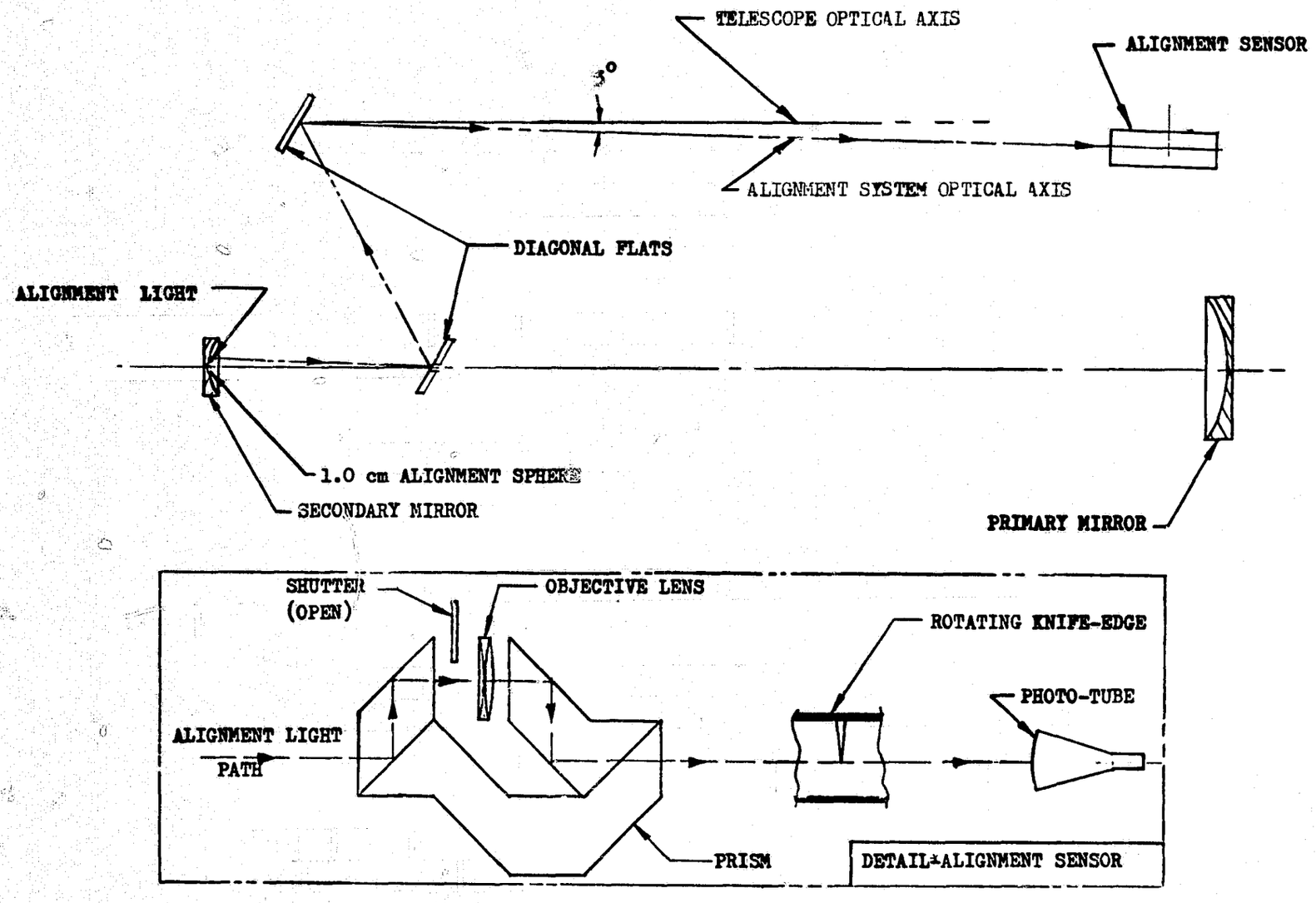

Figure 24. Alignment System - Translation Alignment Mode

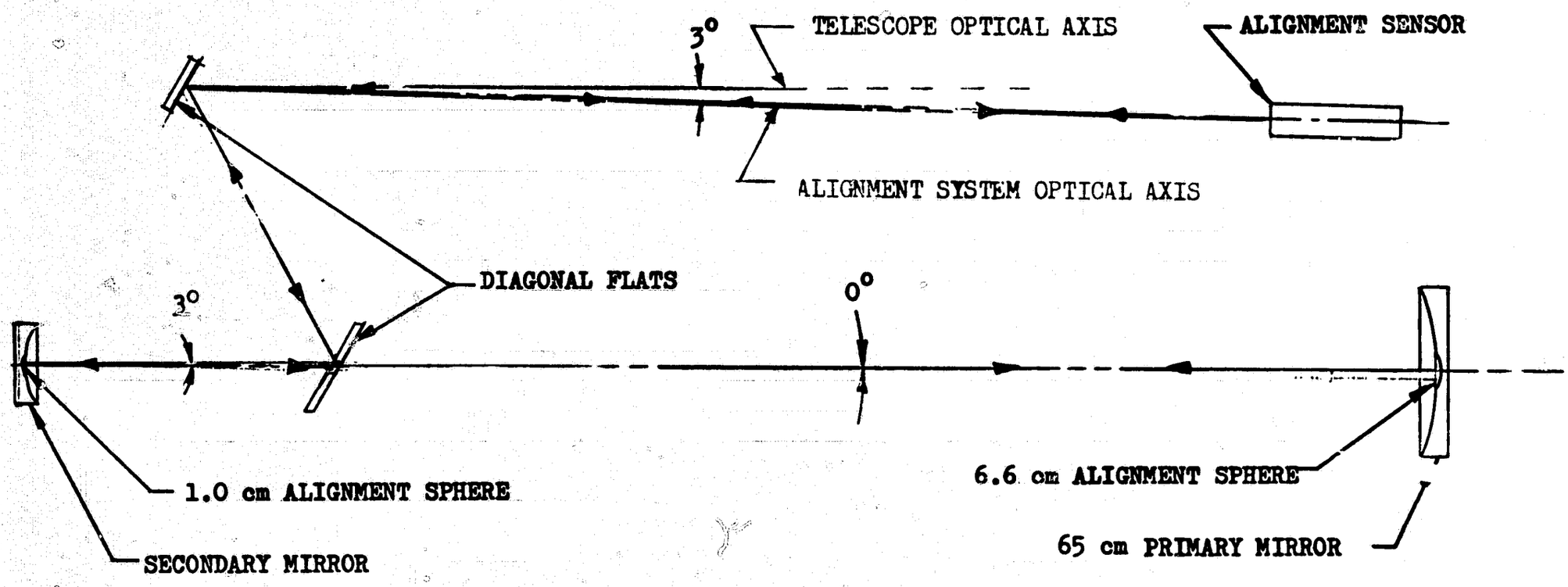

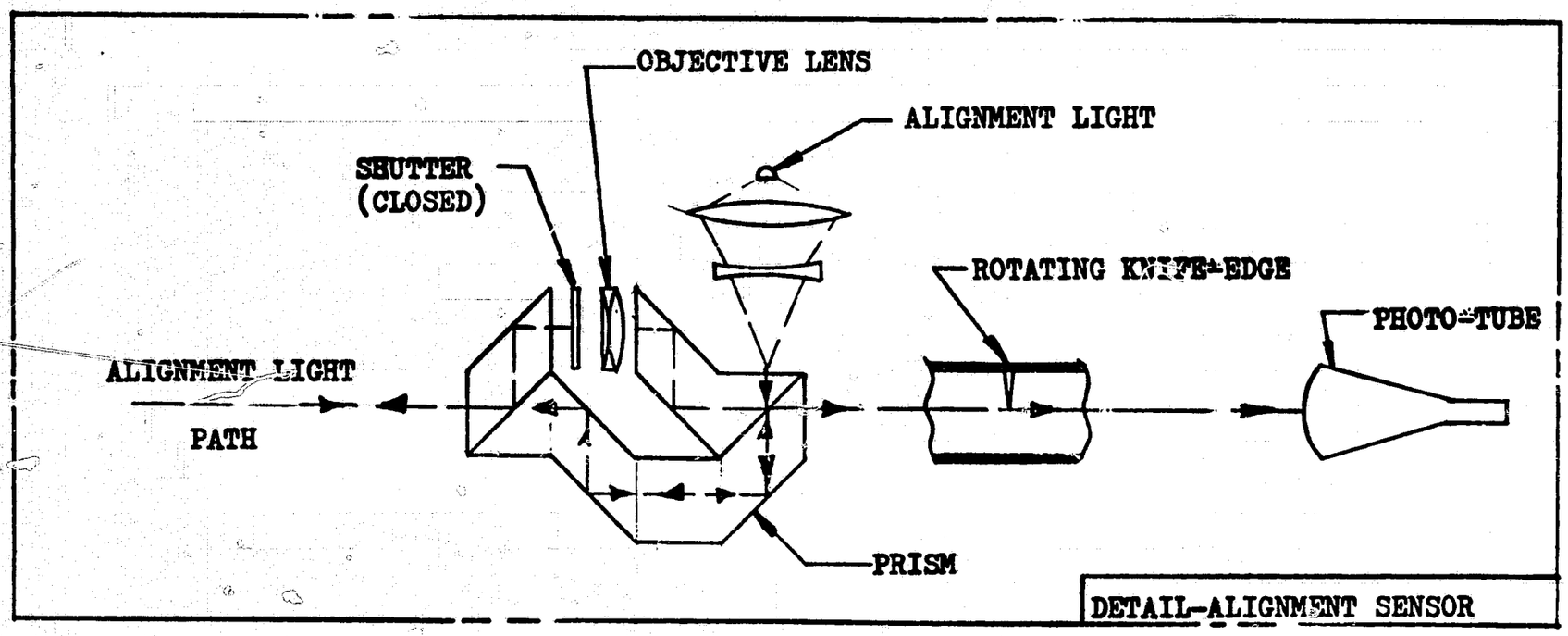

Figure 25. Alignment System - Tilt Alignment Mode

will be simulated using small mirrors whose sizes correspond to that portion of the photoheliograph mirrors which actually are involved in the alignment sensing process.

Focus sensing will be accomplished by measuring the mid-range and high-frequency content of the photoheliograph video signal. The telescope image will contain spatial frequencies whose amplitude is the product of the spatial frequency of the scene being observed (target) and the MTF of the optical system. The video camera, of course, converts the spatial frequency of the image into temporal frequency of the video signal. If the video signal is passed through a bandpass filter and rectified, the resultant d. c. level gives a measure of the amplitude of the temporal frequencies within the bandpass. This can be related directly to the amplitude (modulation) of the corresponding spatial frequencies within the spatial bandpass. Thus, if the modulation of spatial frequencies in the target stays constant during the period of measurement, any change in d. c. level of the rectified signal represents a change in the MTF over the bandpass being sampled. By changing the position of the cameras and monitoring the filtered and rectified video signal, it will be possible to determine the camera position which gives best focus (highest d. c. level).

While the alignment and focusing techniques are currently designed to use the astronaut "in-the-loop," complete automation of the techniques can be accomplished by the addition of suitable logic circuits. The techniques, when automated, are applicable to unmanned spacecraft operation.

REFERENCES

1. A. E. Conrady, Applied Optics and Optics Design (Dover Publications, Inc., New York) 1957, pp. 136-7. (Original publication date - 1929.)

2. E. L. O'Neill, Introduction to Statistical Optics (Addison-Wesley Publishing Co., Reading, Mass.) 1963, p. 88.

3. W. J. Smith, Modern Optical Engineering (McGraw-Hill Book Co., New York) 1966, p. 318.

4. A. E. Conrady, op. cit., p. 139.

5. A. E. Conrady, op. cit., p. 138.

APPENDIX A

THE STREHL RATIO

The Strehl ratio is defined (Ref. 1) as the ratio of light intensity at the peak of the diffraction pattern of an aberrated image to that at the peak of an aberration-free image. This is illustrated in Figure A-1. The value of the Strehl ratio can also be determined if the modulation transfer function (MTF) of the optical system is known. This is done by computing the volume under the three-dimensional MTF of an aberrated system and dividing by the volume under the MTF of an aberration-free system of the same numerical aperture (Refs. 1 and 2).

The utility of the Strehl ratio lies in the fact that it is a single-valued parameter by which the performance of an optical system can be specified. For optical systems whose performance is 1/2-wave or better, it offers, by virtue of its definition, a visualization of the energy distribution in the diffraction pattern of a point image (point-spread function). For performance poorer than 1/2 wave (i.e., two Rayleigh limits), the diameter of the diffraction pattern expands (Ref. 3) and the height of the peak of the pattern no longer gives a good approximation of the volume (energy) in the Airy disk.

The Strehl ratio does not provide as much information about the imaging characteristics of an optical system as does the MTF; that is, it does not give the transfer function of the system as a function of spatial frequency. In this regard it is limited. However, unless the spatial frequency spectrum of the input to the optical system is known, the MTF offers little useful information. If one considers the input to have equal amplitudes at all frequencies, then the output of the optical system will be determined by the MTF alone, and the Strehl ratio, computed on the basis of MTF volumes, provides a good figure of merit for the optical performance.

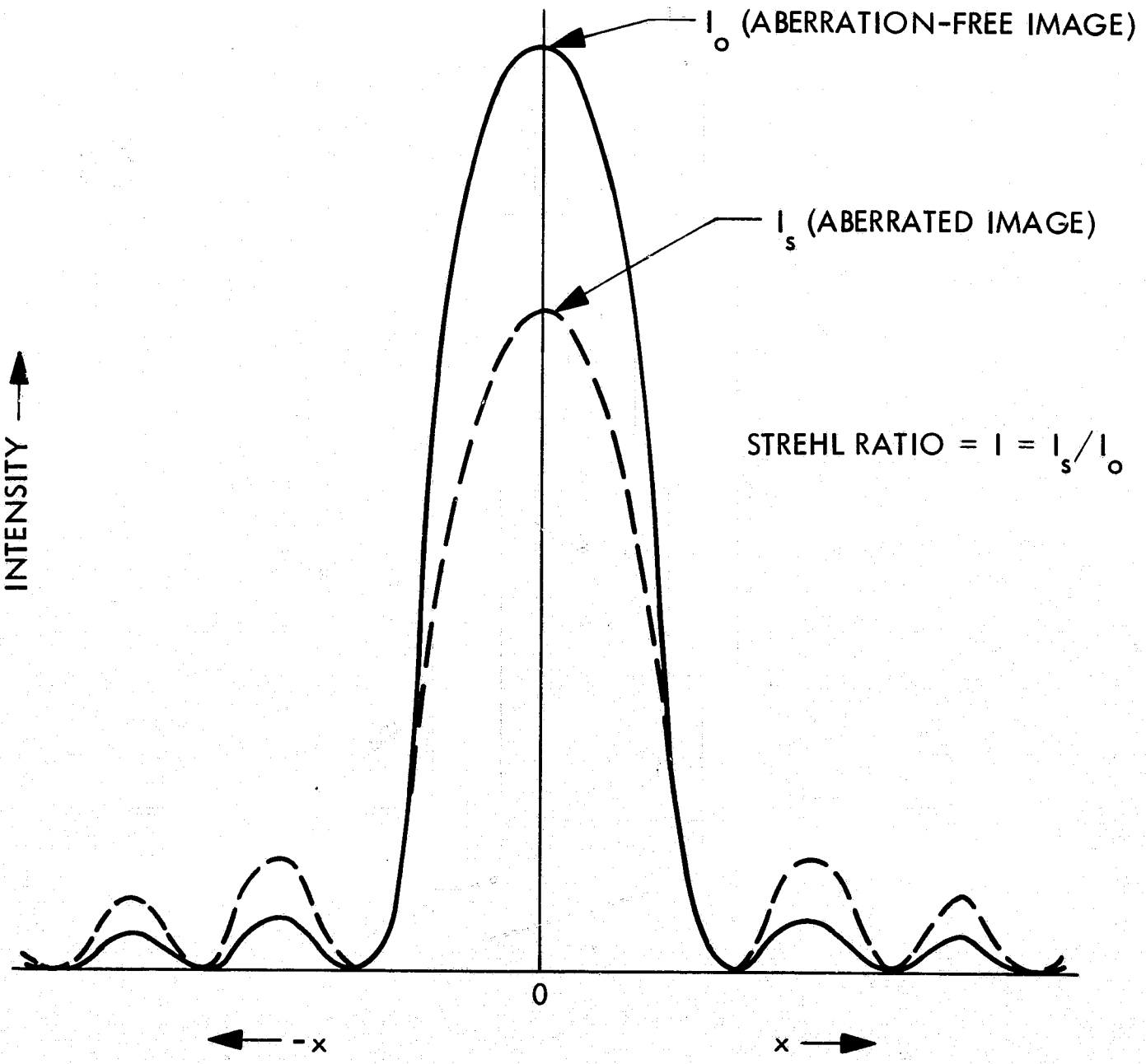

Figure A-1. Strehl Ratio

REFERENCES

1. W. J. Smith, Modern Optical Engineering (McGraw-Hill Book Co., New York) 1966, p. 311.

2. E. L. O'Neill, Introduction to Statistical Optics (Addison-Wesley Publishing Co., Reading, Mass.) 1963, p. 88.

3. A. E. Conrady, Applied Optics and Optics Design (Dover Publications, Inc., New York) 1957, p. 139.

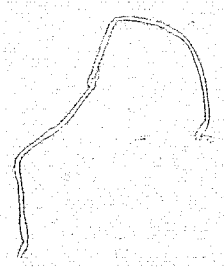

APPENDIX B

OBSCURATION AT THE FIRST DIAGONAL FLAT

In Figure B-1, two rays (a) are shown passing through the holes in the center of the heat-stop mirror and the first diagonal flat, hereafter called the flat. These rays define the outer limits of the cone of rays from the primary mirror which pass through the center of the prime focus image. The hole in the heat-stop mirror has a projected diameter $\underline{b}$ in the prime-focus image plane. The direction of any rays in the plane of the figure passing from the edge of the primary mirror through the aperture in the heat-stop mirror will be within a small angle ϕ of the direction shown for rays (a). The angle ϕ is given approximately by

$$\phi = (b/2F_p) \cos^2 \alpha$$

where F_p = primary mirror focal length = 250 cm. Now, b = 0.36 cm and $\alpha = 7.4°$; therefore, ϕ is approximately 2.5 arc minutes. Since this angle is so small, we may say that the maximum diameter of the total cone of rays passing through the heat-stop aperture is very closely given by $\underline{b}$ plus the diameter of the cone of rays defined by rays (a). Thus, the projected maximum diameter of the hole required in the flat mirror to clear the bundle of rays passing through the center of the prime-focus image is $\underline{L} + \underline{b}$. The dimension $\underline{L} + \underline{b}$ is the projection of the major axis of the quasi-elliptical hole in the flat onto the incident beam coming from the secondary mirror. Thus, $\underline{L} + \underline{b}$ represents the maximum effective obscuration dimension of the hole. This effective obscuration may be larger (in percentage of beam occulted) than that caused by the secondary mirror cage on the beam incident on the primary mirror; therefore, it is necessary to analyze the nature of this effective obscuration. Since $\underline{b}$ is a constant, we need only to investigate $\underline{L}$. $\underline{L}$ is a function of S, α, and θ. The first two parameters are constants; therefore, we shall investigate $\underline{L}$ as a function of θ. We note that

$$L = (x + \Delta x_1) + (x - \Delta x_2) = 2x + \Delta x_1 - \Delta x_2 \qquad (1)$$

Now,

$$x = d \tan \alpha \tag{2}$$

where α = constant determined by primary mirror focal ratio.

The variable d is given by

$$d = S/\cos(\theta/2) = S \sec(\theta/2) \tag{3}$$

where S is a constant established from mechanical considerations.
Therefore,

$$x = (S \tan \alpha) \sec(\theta/2) = K \sec(\theta/2) \tag{4}$$

where $K = S \tan \alpha$ = constant.
We may now write

$$L = 2K \sec(\theta/2) + \Delta x_1 - \Delta x_2 \tag{5}$$

From Figure B-1 we see that

$$\Delta x_1 = u_1 \sin \alpha \tag{6}$$

We solve for u_1 by using the Law of Sines,

$$\frac{u_1}{\sin(\theta/2)} = \frac{x}{\sin \beta}$$

Since,

$$\beta = \pi/2 - (\alpha + \theta/2)$$

$$\sin \beta = \sin[\pi/2 - (\alpha + \theta/2)] = \cos(\alpha + \theta/2)$$

Therefore,

$$u_1 = x \sin (\theta/2) \sec (\alpha + \theta/2) \tag{7}$$

Combining Equations (4) and (7) we have

$$u_1 = K \sec (\theta/2) \sin (\theta/2) \sec (\alpha + \theta/2)$$

$$u_1 = K \tan (\theta/2) \sec (\alpha + \theta/2) \tag{8}$$

and

$$\Delta x_1 = K \sin \alpha \tan (\theta/2) \sec (\alpha + \theta/2)$$

In solving for Δx_2 we note that

$$\Delta x_2 = u_2 \sin \alpha \tag{9}$$

and

$$\frac{u_2}{\sin (\theta/2)} = \frac{x}{\sin (\alpha + \gamma)} \tag{10}$$

From

$$\gamma = \pi/2 - \theta/2$$

we can write

$$\sin \gamma = \cos (\theta/2)$$

$$\cos \gamma = \sin (\theta/2)$$

and

$$\sin (\alpha + \gamma) = \sin \alpha \cos \gamma + \cos \alpha \sin \gamma$$

$$= \sin \alpha \sin (\theta/2) + \cos \alpha \cos (\theta/2)$$

$$= \cos (\alpha - \theta/2)$$

Therefore,

$$u_2 = x \sin(\theta/2) \sec(\alpha - \theta/2)$$

and, substituting from Equation (4),

$$u_2 = K \tan(\theta/2) \sec(\alpha - \theta/2)$$

Thus,

$$\Delta x_2 = K \sin\alpha \tan(\theta/2) \sec(\alpha - \theta/2)$$

We may now re-write Equation (1) as

$$L = 2K \sec(\theta/2) + K \sin\alpha \tan(\theta/2) \sec(\alpha + \theta/2)$$
$$- K \sin\alpha \tan(\theta/2) \sec(\alpha - \theta/2)$$

from which

$$\boxed{L/K = 2 \sec(\theta/2) + \sin\alpha \tan(\theta/2) \left[\sec(\alpha + \theta/2) - \sec(\alpha - \theta/2)\right]}$$

where $K = S \tan\alpha$.

It is shown that $L + b$, the maximum effective obscuration, increases with increasing $\sec(\theta/2)$, $\tan(\theta/2)$, and $\sec(\alpha + \theta/2)$ and decreases with an increase in $\sec(\alpha - \theta/2)$. Now the angle $\theta/2$ will always be less than $\pi/2$; therefore, $\sec(\theta/2)$ and $\tan(\theta/2)$ will increase with increasing θ. Further, from Figure B-2, we see that, for $\alpha < 0$, $\sec(\alpha + \theta/2)$ is always greater than $\sec(\alpha - \theta/2)$ and that the difference,

$$\sec(\alpha + \theta/2) - \sec(\alpha - \theta/2)$$

increases with θ. The exception to the above is the case where $(\alpha + \theta/2) > \pi/2$. However, this is not a practical case since, for an f/3.85 primary mirror, α is approximately 7 degrees and $\theta/2$, due to practical considerations, is limited to values in the range of 10-40 degrees.

A plot of $\underline{L}$ vs θ is given in Figure B-3. For this figure, we assume $s = 2.1$ cm and $\alpha = 7.5°$. It is seen that the slope of the curve starts getting steep at approximately $\theta = 60$ degrees.

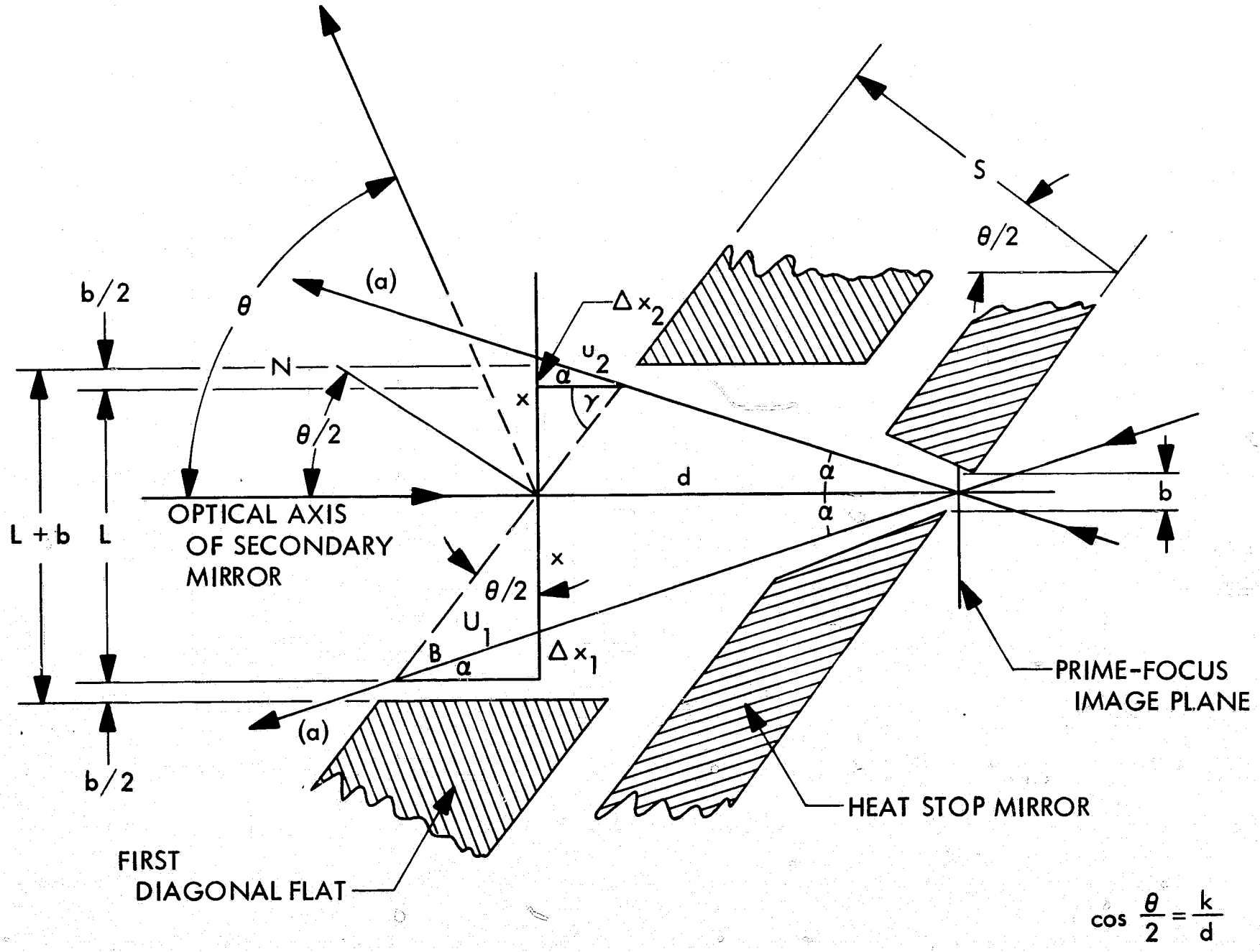

Figure B-1. Geometry at Heat-Stop and First-Diagonal Mirror Planes

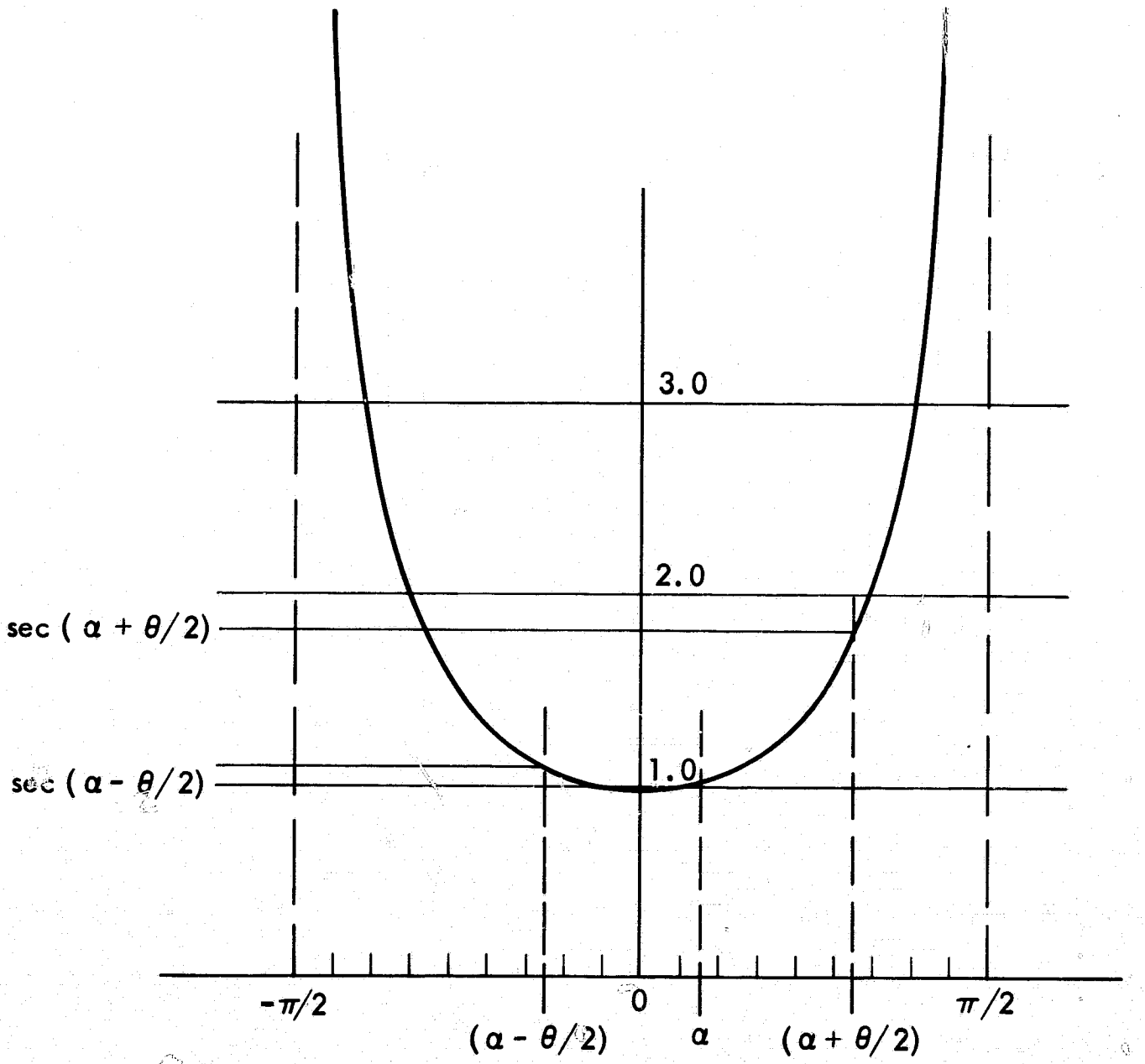

Figure B-2. Sec (α ± θ/2)

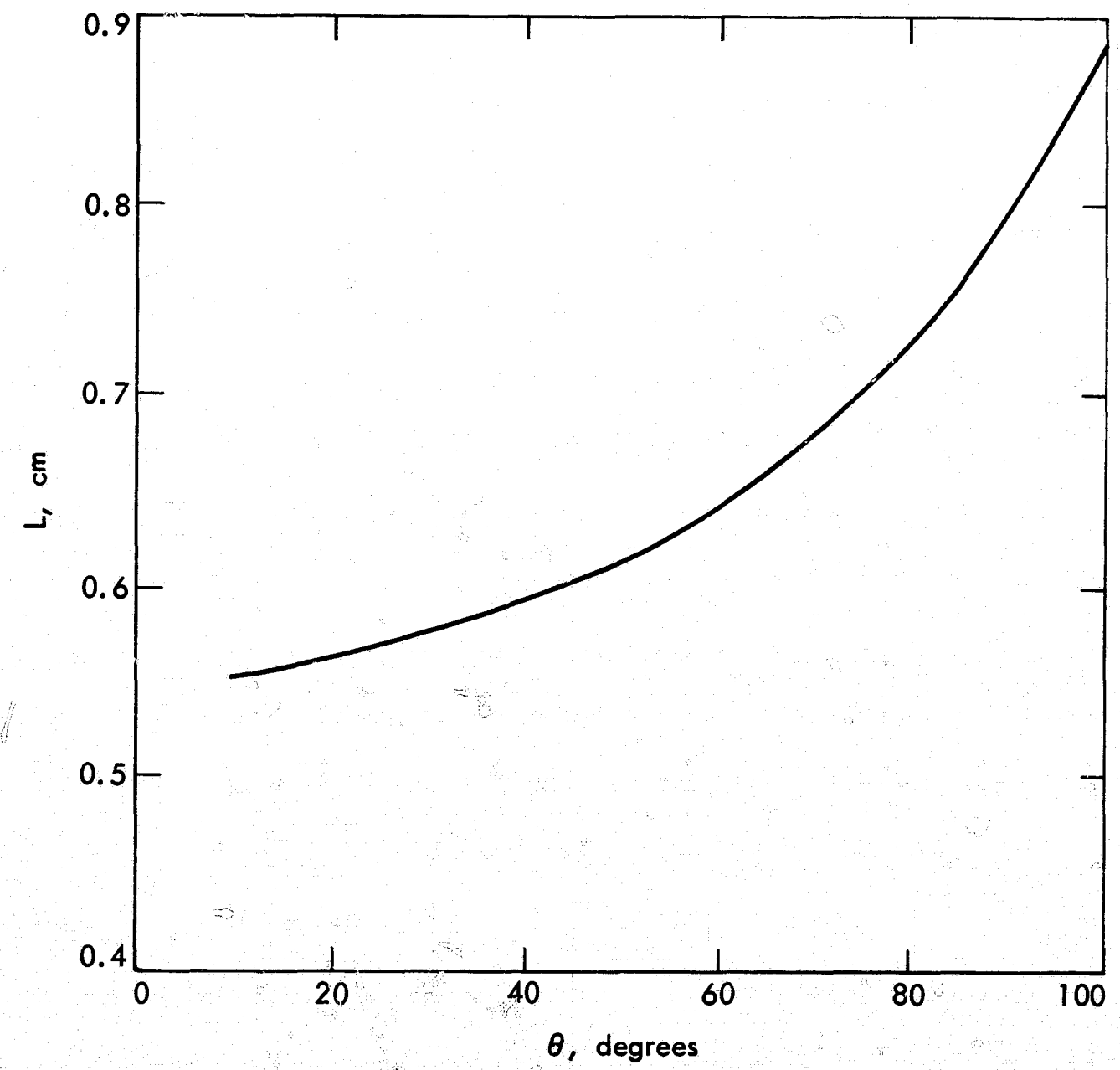

Figure B-3. Plot of L vs θ

APPENDIX C

DEFINITION AND METHOD OF CALCULATION OF THE 1/2 OPD

The optical path difference (OPD) is the difference in optical path length that various rays experience as they converge on a point. Since length, by definition, is measured between two points, we must define two points between which the optical path length is measured. The points are 1) the image point on which the rays are converging and 2) the point of intersection of the ray and a surface. This surface often is, but is not necessarily constrained to, the exit pupil of the system. The surface may be a mathematical surface rather than a real surface.

Consider the case of parallel rays falling upon a parabolic mirror (Fig. C-1). These rays will be focused at a point P lying at the focus of the mirror. The plane A-A in object space represents a surface which defines a possible wavefront for the incoming rays. For purpose of illustration, consider the optical path length of rays 1 and 2 from the surface A-A to the point P. The optical path length from surface A-A to A'-A' is identical for both rays. Likewise, the path length from the point P to the spherical reference surface is the same for both rays. Now, if the total path length is to be the same for both rays, then

$$a + b = c$$

The function of a parabolic mirror is that of providing the above equality. If the equality is not satisfied, the imaging a point P will be degraded. Should the parabola be distorted, we have the equality

$$a + b = c \pm OPD$$

In Figure C-2, the relation of OPD to surface distortion is illustrated. Since the ray has to make a double pass between the missing segment of parabolic surface and the distorted surface, the total OPD is twice the amount of the distortion. Or,

$$\text{surface distortion} = 1/2\ OPD$$

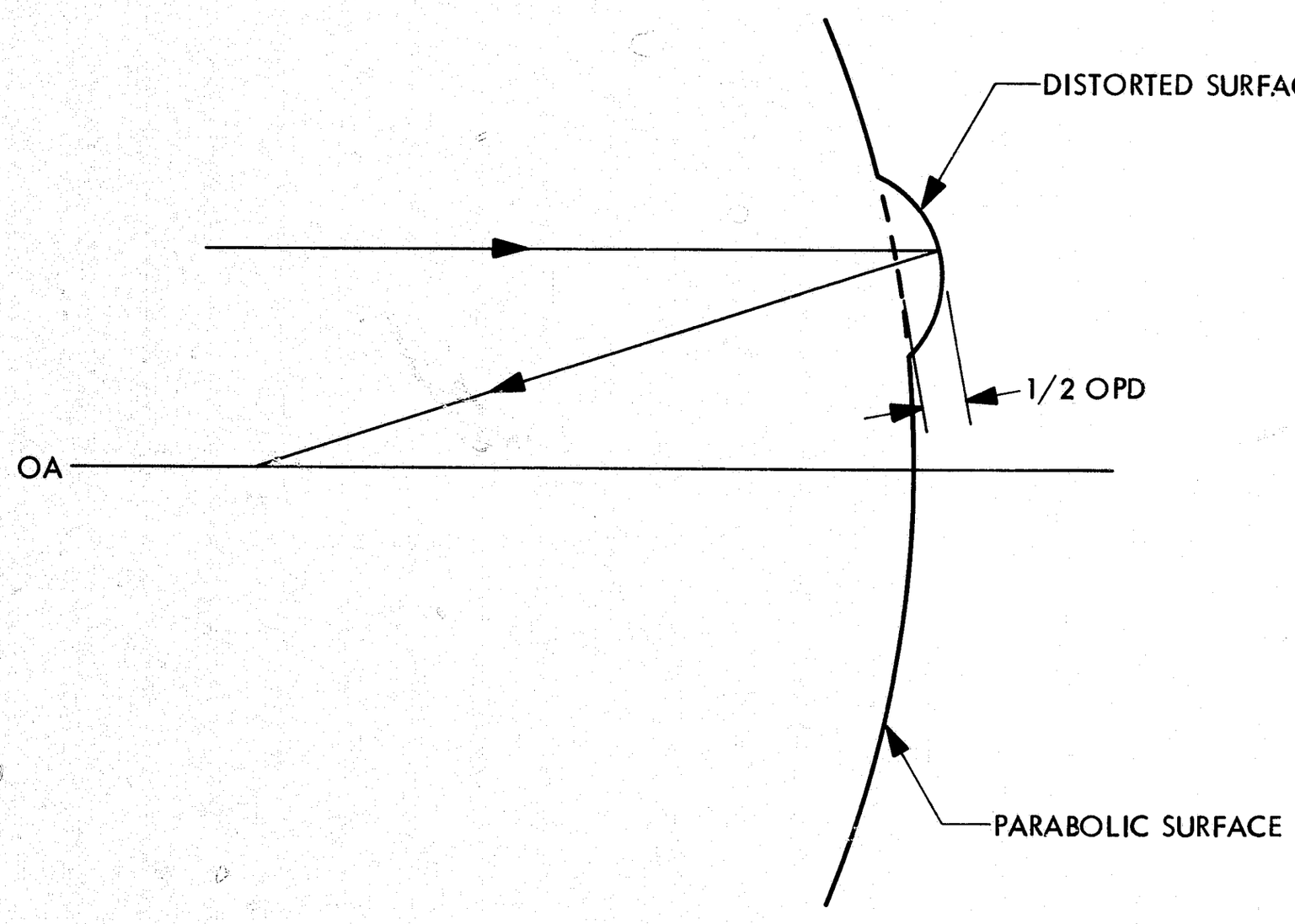

Figure C-1. Imaging With a Parabolic Mirror

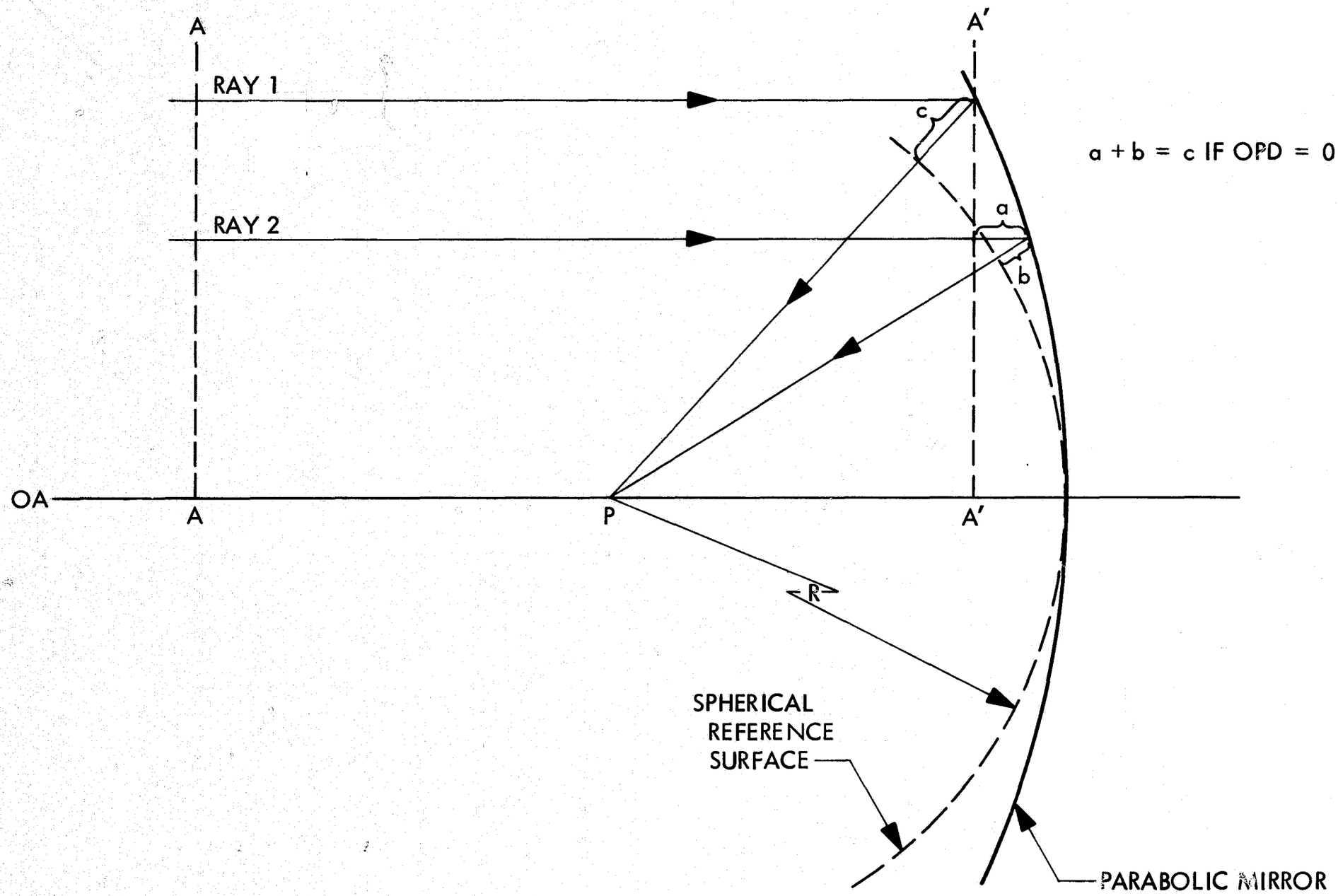

Figure C-2. Relation of OPD to Surface Distortion

Because of the angles involved, the above relation is only an approximation. However, the angles are generally small, and the approximation is sufficiently accurate for analyses.

To calculate the 1/2 OPD the following analysis was used. First, a mathematical parabola of 250-cm focal length was derived. The equation for this is

$$y = x^2/4f = 0.00254000002x^2 \text{ in.}; f = 98.425196 \text{ in.}$$

The computer distortion data, Δy, were listed for selected x radii. The error in distortion (Δy_o) at $x = 0$ was forced to zero by making $\Delta y = 0$ at $x = 0$ (see Fig. C-3). The reduced errors, $\Delta y - \Delta y_o$, were computed for all values of x. The new surface of revolution was described mathematically by letting $y'' = y + (\Delta y - \Delta y_o)$. To determine how closely the new curve, y'', approximated a new parabola (thus a new optical surface of satisfactory imaging characteristics), a new mathematical parabola (y') was generated, choosing a focal length (f') based on the $y + (\Delta y - \Delta y_o)$ value found at maximum radius x of 12.79 inches (32.5 cm) from the center of the mirror. It was found through experience that this focal length gave the least error (difference along the y axis) between the new parabola (y') and the y'' curve. The sum of the maximum positive and negative deviation between the two curves (y' - y'') will give the 1/2 OPD.

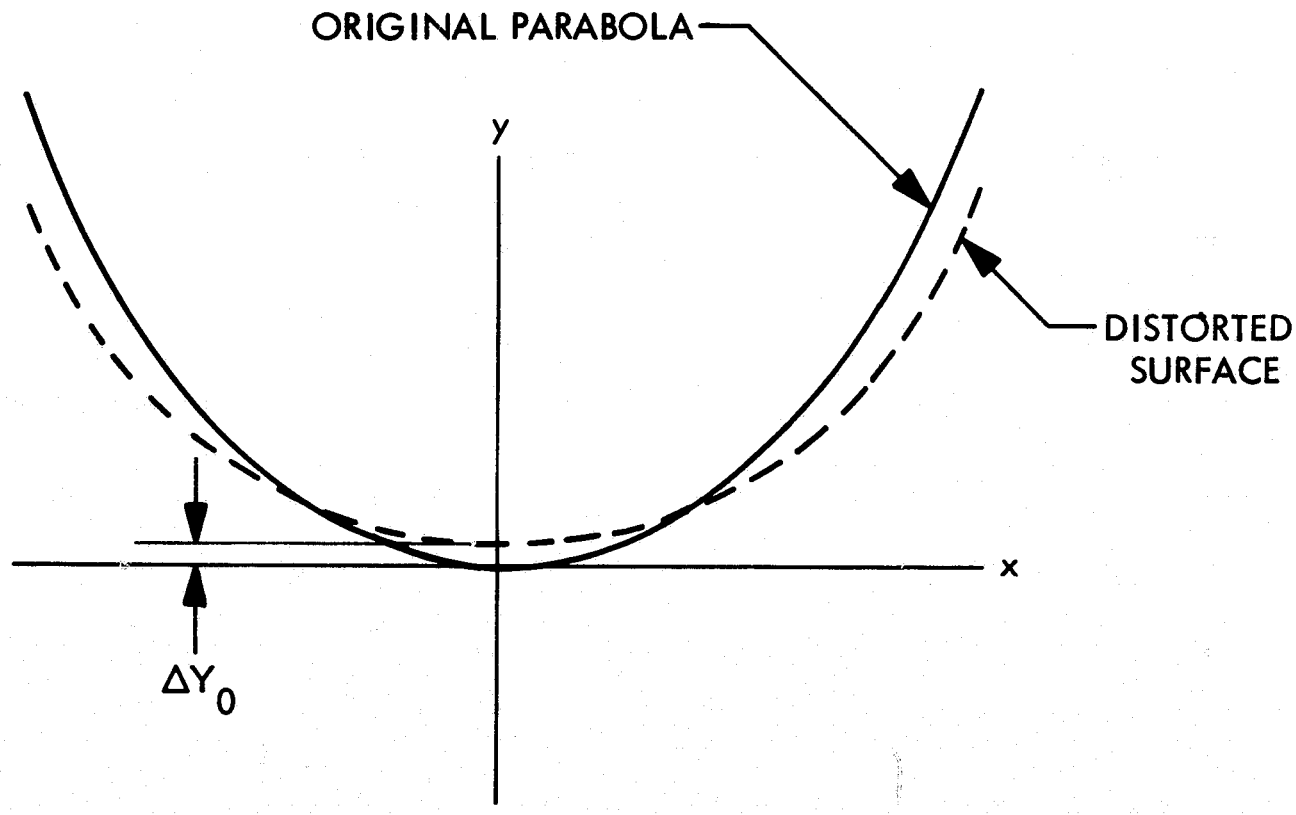

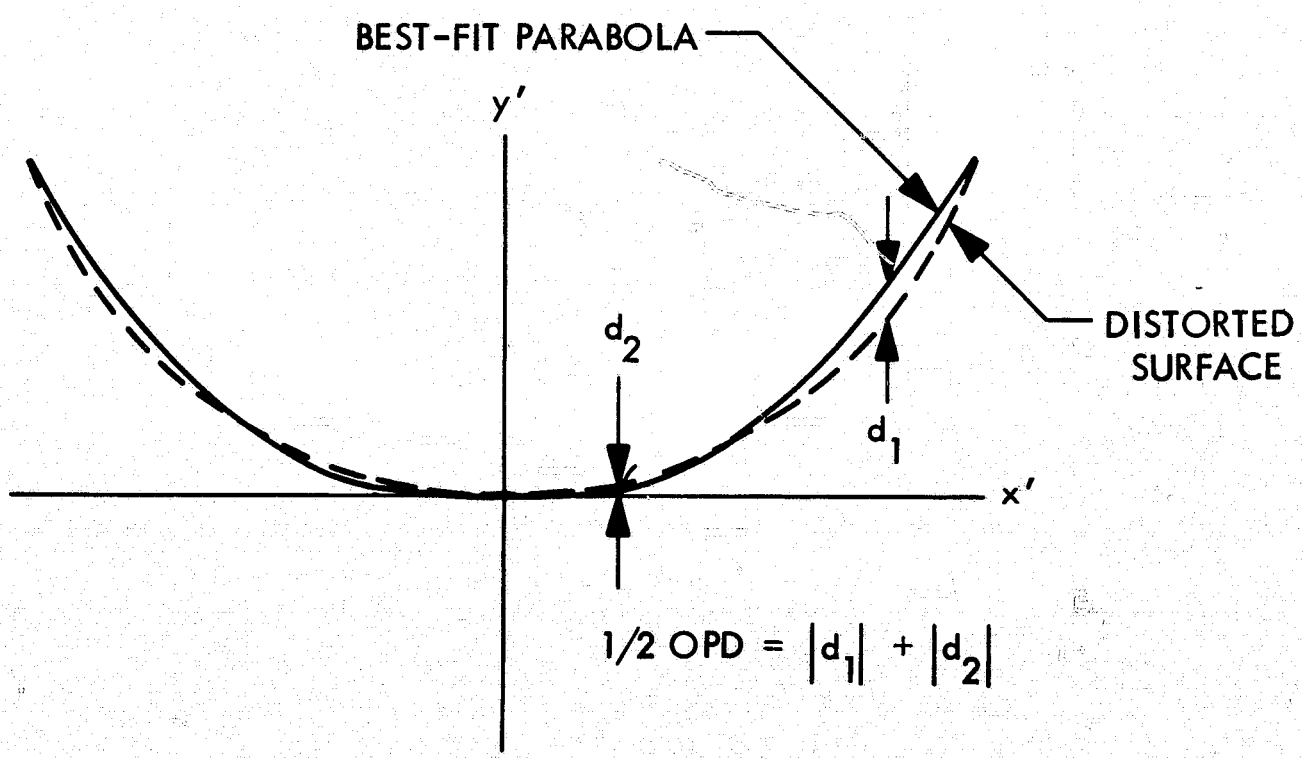

Figure C-3. Calculation of 1/2 OPD

APPENDIX D

IMAGE SMEAR IN THE PHOTOHELIOGRAPH

Inasmuch as the photoheliograph will not be supported by a platform infinitely stable with respect to the sun, it is necessary to investigate the effect of platform motion on the image quality. Since platform angular motion relative to the sun causes image motion in the focal plane, we will here consider the image degradation process of image motion and relate this to platform motion. Finally, the exposure time required to reduce the image degradation to tolerable limits will be considered.

Consider a photometric trace across several bright areas in the image, as illustrated in Figure D-1. For purpose of illustration, three bright areas of size x/2 are separated by a distance also equal to x/2. The photometric trace along the line A-A' is shown in the bottom curve: it is merely a two-valued step function with spatial periodicity equal to x. Let us suppose at some time later another photometric trace is taken along line A-A', but that in the meanwhile, the image has moved with respect to the coordinate system by a distance kx. The second photometric trace will have a spatial phase shift with respect to the first trace by a factor $2\pi\, kx/x$, as shown in Figure D-2.

If a photographic exposure had been made with the image occupying the two positions shown in Figures D-1 and D-2 for equal lengths of time, the exposure on the film would have a spatial distribution along line A-A' equal to the summation of the two photometric traces. This is illustrated in Figure D-3. In this case, where k = 0.25, the resultant exposure (trace 1 + trace 2) still shows 100% modulation. It will be of interest to investigate the effect of k on the modulation, M. The method of simple analysis is shown in Figure D-4. In the upper portion of the figure, the position in the image plane of three objects are indicated by the location of the dark horizontal bars. These bars are shown moving across the image plane by increments of 0.1 kx as we read downward, row by row. This is to represent evenly-spaced time samples of an image moving across the focal plane at constant velocity. The value of k for each row and the time of sampling, t_n, are shown listed to the left of each row.

In the bottom part of the figure, integrated (summed) photometric traces across the image are shown. The first trace, labeled t_1, is the photometric trace at time t_1. The second trace, labeled $t_1 + t_2$, is the summation of traces taken at times t_1 and t_2. It is seen that the second trace approximates the distribution of energy across the image during an exposure time of $t_2 - t_1$. The trace labeled $t_1 + \ldots + t_6$, for example, gives the approximate integrated exposure distribution for the exposure time interval $t_6 - t_1$. To the right of each trace is shown the modulation factor, M, for each trace, where the modulation is defined the same as the classical definition for contrast (see Figure D-5). The modulation factor values from Figure D-4 are plotted as a function of k in Figure D-6. It should be remembered that k is defined in Figure D-2 as the fraction of the spatial displacement period (x) that the image has moved during the exposure time. In Figure D-6, we note that M = 0 when k = 0.9 although, intuitively, we would expect M to be zero when k = 1.0. This apparent discrepancy results from the fact that we have been determining dM/dk where the lim k = 0.1, rather than for the case of lim $k \longrightarrow 0$. It is fairly easy to rationalize that as lim $k \longrightarrow 0$, the first minimum on the curve of M vs k will approach the value k = 1.0, as shown in Figure D-7.

Thus, we see that if, during the open shutter time, the image moves with constant velocity a distance equal to the periodic spacing of the image detail, the detail will be completely "washed out."

Following the method given by Robert N. Wolfe and Robert L. Lamberts in "The Effect of Image Motion on Resolving Power," Photographic Engineering, Vol. 6, No. 4, pp. 270-74, we can draw a curve to help us predict the effect of image motion on the resolving power of the ATM photoheliograph. Such a curve is shown in Figure D-8. The horizontal line RP_c is the static resolution of the camera with no image motion. For the f/50 Gregorian design, RP_c = 33 line-pair/mm. The slanting line RP_m is the locus of the points where the modulation goes to zero due to image motion, and is derived from consideration of Figures 4 and 7. For example, this line has a value of 10 ln-pr/mm when image motion is equal to 0.10 mm during the exposure; 100 ln-pr/mm when

image motion is 0.01 mm, etc. The curved line is a plot of the resultant resolution, RP, defined by

$$RP = \frac{1}{\frac{1}{RP_c} + \frac{1}{RP_m}} \qquad (1)$$

Experimental data taken by Wolfe and Lamberts agree well with an RP plot based on the above equation.

If the ATM photoheliograph experiences image motion of 0.001 mm (1 micron) during exposure, the resolution will drop from 33 ln-pr/mm to 32 ln-pr/mm according to Figure D-8. This is a 3% loss in resolution. Should the image motion be 0.010 mm, the resolution drops to 24.8 ln-pr/mm -- a 25% loss.

Since the image motion in the film plane can be expressed in terms of focal length, exposure time, and pitch or yaw rate (roll will be treated later), we can plot percentage loss of resolution against exposure time for a given pitch or yaw rate and focal length. The focal length of the f/50 Gregorian is 3.25×10^4 mm. The pitch and yaw jitter rates for the ATM are presently quoted as 1 arc-sec/sec. Thus the image displacement during exposure time is given by

$$dx = f(d\phi/dt)t$$

$$= 3.25 \times 10^4 \text{ mm} \left(\frac{1 \text{ arc-sec}}{\text{sec}} \times \frac{1 \text{ radian}}{2.06 \times 10^5 \text{ arc-sec}} \right) t$$

$$= 1.58 \times 10^{-1} \frac{\text{mm}}{\text{sec}} (t) \qquad (2)$$

The Table D-1 is derived from calculations based on Equations (1) and (2). The dx values obtained from Equation (2) for various exposure times become the $1/RP_m$ values for Equation (1). The value for RP_c is the resolution of the telescope and camera; i.e., 33 line-pair/mm (it is assumed that the sensor does not degrade the system resolution significantly). The percentage loss of resolution is defined as $100\ (RP_c - RP)/RP_c$.

Table D-1. Loss of Resolution as a Function of Exposure Time in the Presence of Yaw and Pitch Jitter

Exposure Time t (sec)	Image Displacement dx (mm)	System Resolution RP (ln-pr/mm)	Percentage Loss of Resolution
0.001	1.58×10^{-4}	32.8	0.51
0.003	4.74×10^{-4}	32.5	1.54
0.005	7.90×10^{-4}	32.2	2.54
0.010	1.58×10^{-3}	31.4	4.93
0.030	4.74×10^{-3}	28.5	13.5
0.050	7.90×10^{-3}	26.2	20.7
0.100	1.58×10^{-2}	21.7	34.3
0.300	4.74×10^{-2}	12.9	61.0
0.500	7.90×10^{-2}	9.15	72.2

The percentage loss of resolution is plotted against exposure time in Figure D-9. It is seen that if a 10% loss in resolution is permissible, an exposure time up to 24 milliseconds may be used. If only 5% loss is to be allowed, exposure times will have to be no longer than 10 milliseconds. It must be remembered that this is for a jitter rate in pitch and yaw of 1 arc-sec/sec. The allowable exposure time varies inversely as the jitter rate.

The effect of roll rate must be evaluated in a different manner. Since the roll axis and the optical axis are essentially parallel, the linear smear of the image will be greatest at the corners of the film format. The distance from the optical axis to the corner of the frame is 15 mm; therefore, the linear smear can be expressed as

$$dx = 15 \text{ mm } (d\theta/dt)\, t \qquad (3)$$

where

$d\theta/dt$ = roll jitter rate = 1 arc-min/sec = 0.00029 radian/sec

t = exposure time.

This may be written as

$$dx = 15 \text{ mm } (2.9 \times 10^{-4} \text{ radian/sec})\, t$$

$$= 4.35 \times 10^{-3} \, (t) \text{ mm/sec}$$

Note that the effect of roll rate is dependent of focal length.

The loss of resolution resulting from roll, pitch, and yaw rates is plotted on Figure D-9. In the exposure range of interest (i.e., that permissible under conditions of yaw and pitch jitter), the loss due to roll jitter is less than one percent and will be undetectable. Roll jitter rate will not be a problem unless the rate is increased by an order of magnitude or unless the yaw and pitch jitter rates are decreased by an order of magnitude, in which case longer exposure times might be used.

In terms of loss of angular resolution, the effects of image motion and exposure time are summarized in Table D-2.

Table D-2. Loss of Angular Resolution Due to Image Motion

Exposure Time (seconds)	Resolution (arc seconds)
0	0.193
0.025	0.219
0.050	0.242
0.075	0.269
0.100	0.292
(Note: for pitch and yaw jitter rates of 1 arc-sec/sec)	

A 0.025-second exposure time yields an 11 percent loss of resolution under the condition of maximum jitter rate. If possible, exposure times should be limited to the 0.025-second level.

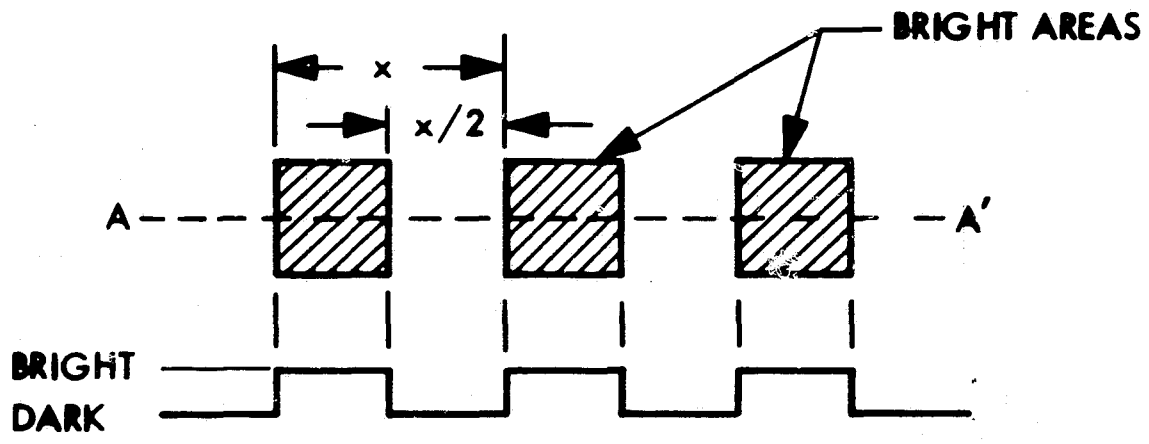

Figure D-1. Photometric Trace of Periodic Image

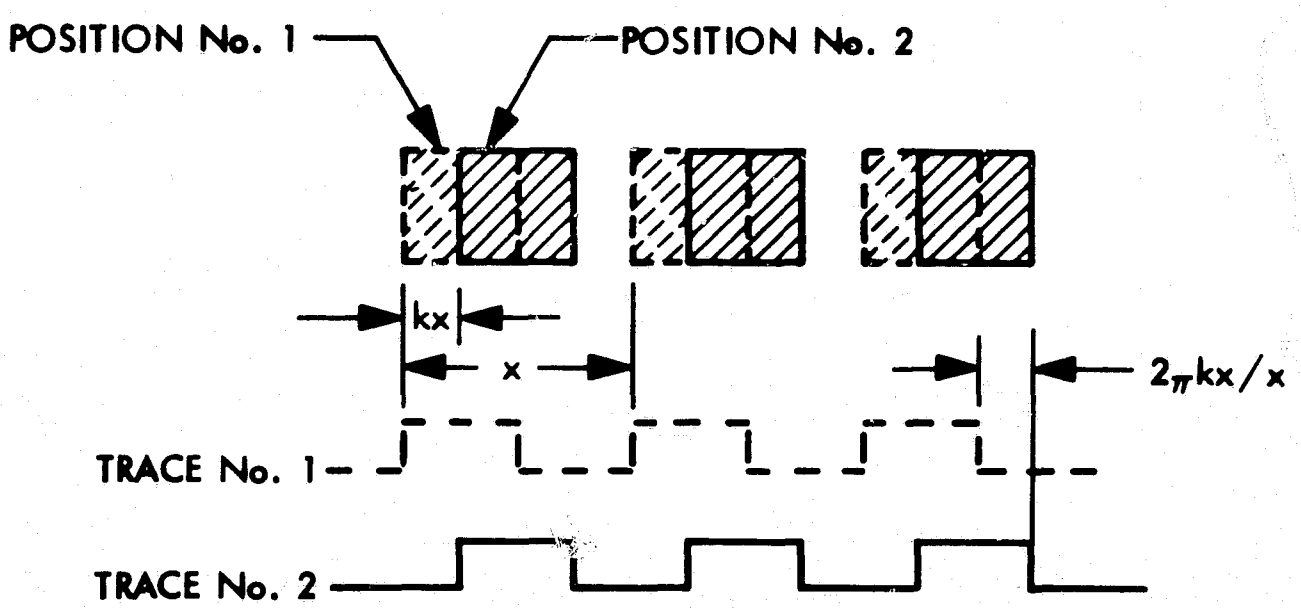

Figure D-2. Photometric Traces of Moving Periodic Image

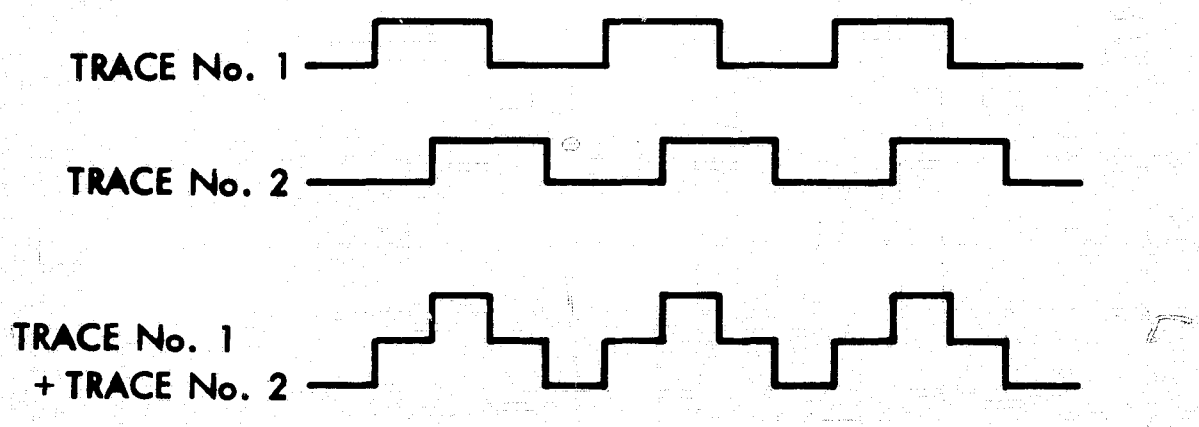

Figure D-3. Summation of Two Traces Taken During Exposure, for k = 0.25

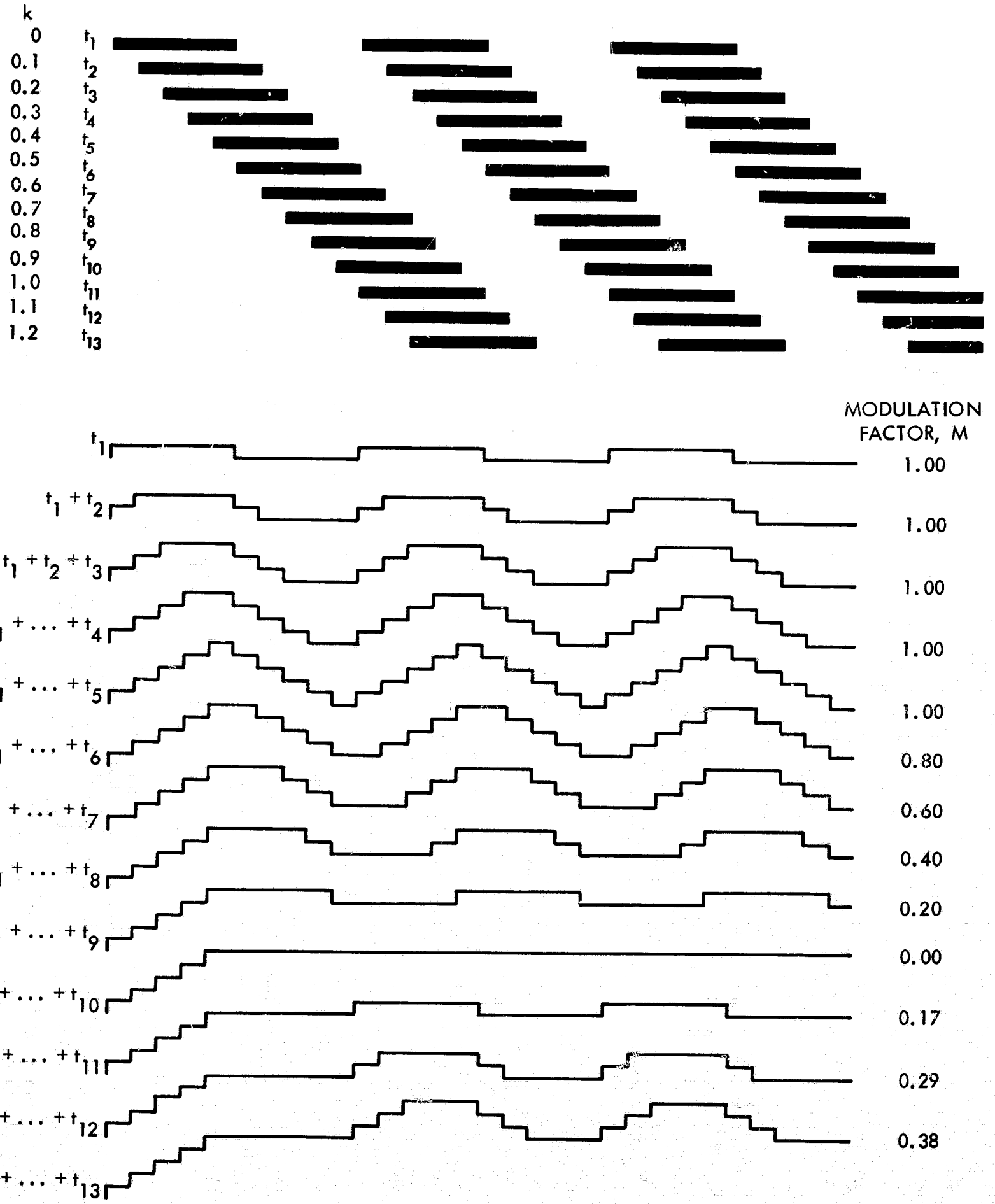

Figure D-4. Modulation of Summed Traces for Various Values of k

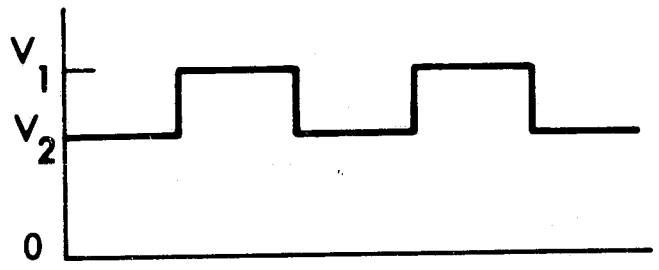

M = MODULATION FACTOR = $(V_1 - V_2)/V_1$

Figure D-5. Definition of Modulation Factor (Contrast)

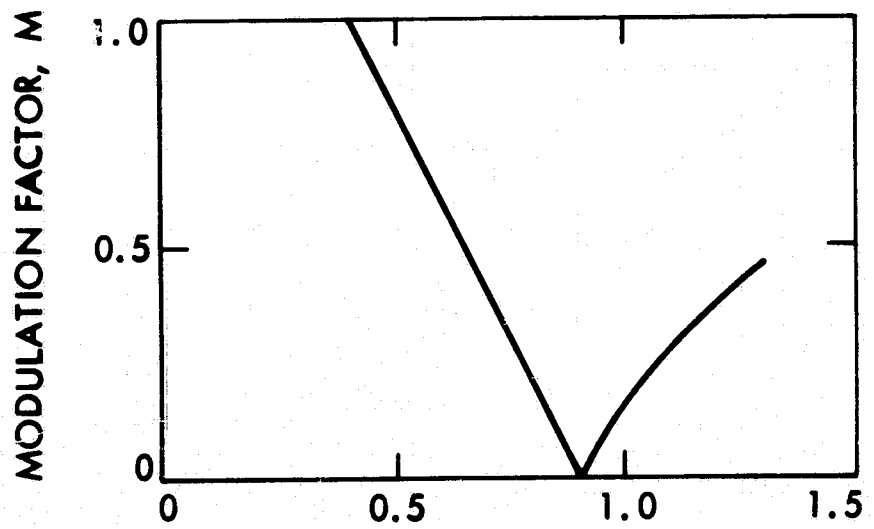

Figure D-6. Modulation Factor vs k, for lim k = 0.1

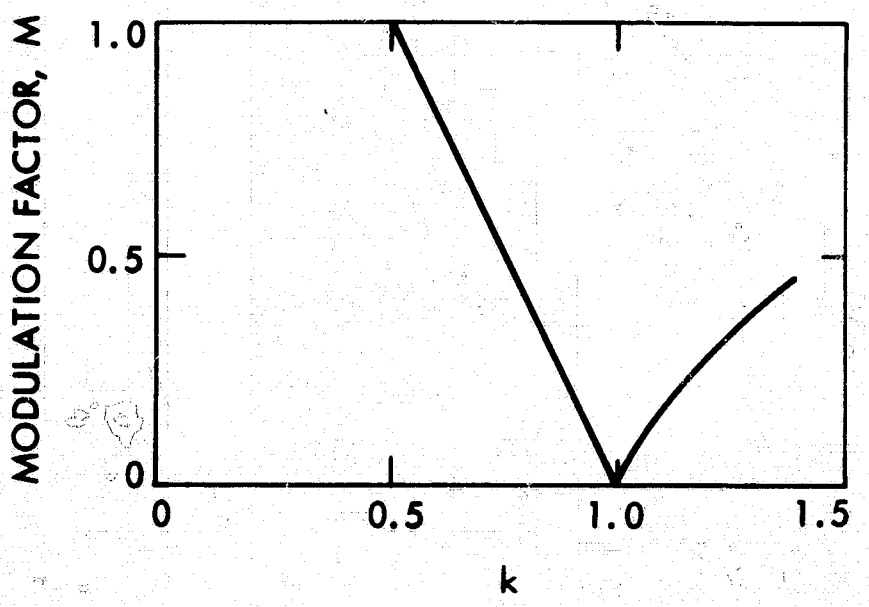

Figure D-7. Modulation Factor vs k, for lim k→0

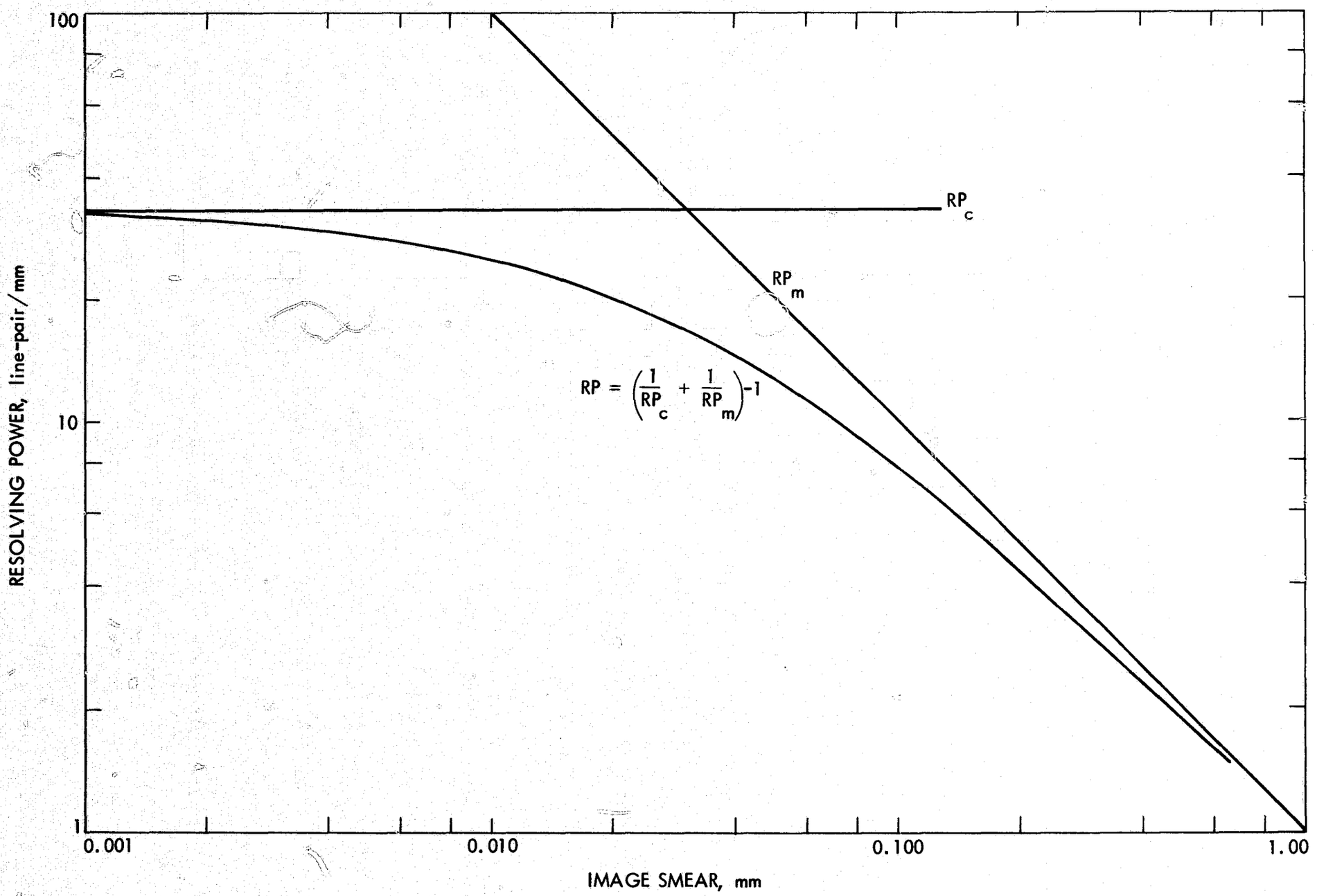

Figure D-8. Plot of Resolving Power vs Image Smear

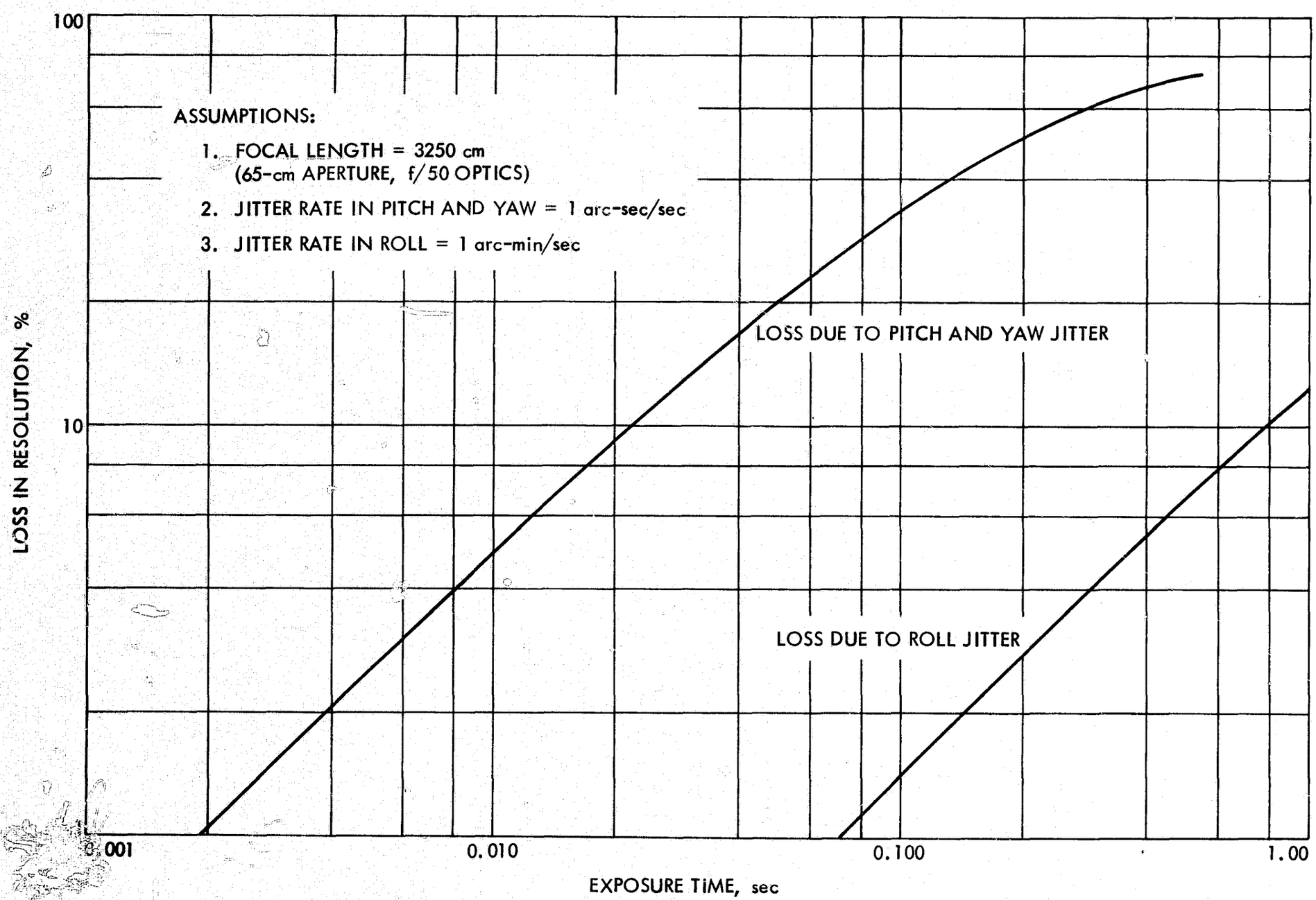

Figure D-9. Resolution Loss vs Exposure Time in the Presence of Jitter

APPENDIX E

OPTICAL SURFACE TOLERANCES FOR DIFFRACTION-LIMITED OPTICS

At the present time many significant advances are taking place in the field of optics. New optical terms are appearing in the literature and are often misused. A good example is the term "diffraction-limited optical system." A diffraction-limited optical system can only exist in theory, not in reality. (There is one exception to this rule: the pin-hole camera.) A diffraction-limited optical system implies that the limiting factor on performance is diffraction itself; i.e., the presence of an aperture. To achieve this condition, the lens must have perfectly shaped components made of perfect materials existing in perfect alignment. All real optical systems (excepting the pin-hole camera), therefore, must be less than diffraction limited. In spite of this, optics users and optics manufacturers continually talk of diffraction-limited optical systems. What then is meant by this term?

Two definitions representing extremes are given below:

1. A diffraction-limited optical system is one in which the first three Seidel aberrations (spherical aberration, coma, and astigmatism) and the color aberrations are smaller in magnitude than the diameter of the first dark ring in the Airy pattern (diameter of the diffraction blur circle)

   where

   $$\text{blur circle diameter} = 2.44\ \lambda/D$$

   and

   D = diameter of optical system aperture.

2. A diffraction-limited optical system yields a perfectly spherical wavefront in image space for any point source in object space.

The second definition is a true definition of a diffraction-limited optical system. It assumes that the spherical or plane wavefront which impinges upon the entrance pupil of the system will leave the exit pupil with precisely the spherical shape intended by the optical designer through his choice of surface shapes

and indices of refraction. This is, of course, an idealized case which neglects entirely the problem of manufacture.

The first definition given above is very loose and can be applied to nearly any stopped-down hand camera. This is true since the diffraction blur circle diameter increases as the lens aperture decreased and the size of Seidel and chromatic aberrations decrease with lens aperture. A common camera lens may thus become diffraction limited at perhaps F/11 or F/16. An example of this is shown for a thin lens of 50-mm focal length in Figure E-1. Note that the field of view specified on the figure is quite small (5.7° = 0.1 radian). If the lens were corrected for astigmatism, as any good camera lens would be, a similar analysis could be shown for a much larger field.

Neither of the definitions given above say anything directly about the accuracy of manufacture and support of the optical elements although the second definition implies that manufacture, support, and design are all perfect. A working definition of a diffraction-limited optical system must take into account the physical condition of the optical elements as well as their design. For reflecting telescopes, only optical element surface irregularities (errors) need be considered. For refracting elements, one must also consider the variations in homogeneity (index of refraction) of the transparent media.

Two types of wavefront distortion may be analyzed: gross, systematic distortions and small-scale, random distortions. These are explained in an oversimplified manner in Figure E-2. Assume that spherical wavefronts are converging on point f in Figure E-2a, but that we wish to investigate the image at point p (case of a de-focused image). The dashed curved lines indicate the curvature the wavefronts must have in order to properly converge and form a point image at p. The difference, δ, along the dashed radial lines is the wavefront distortion (or error) as seen from point p for marginal rays. As drawn, the wavefront error is seen to decrease as we approach paraxial rays. (It is obvious that the figure could have been drawn so that the maximum wavefront error was on the axis and the error at the marginal rays equal to zero. Thus, we should not assume that wavefront errors do not exist on axis. This is entirely a matter of definition.) The wavefront in Figure E-2a is not irregular in shape, but is not spherical as seen from point p. Only waves that are spherical as seen from point p can converge on p to form an aberration-free image.

Irregular wavefronts such as shown in Figure E-2b converge on many points not necessarily on axis. The distortions of randomly irregular wavefronts may be called statistical distortions, since their contribution to the image must be handled statistically.

One of the most popular methods of optical system evaluation is the use of either theoretical or experimental techniques to determine the modulation transfer function (MTF) of the system. This technique is very informative in regard to the information content of extended images; however, it does not offer a direct visualization of the image. Such visualization, for point images at least, is offered by the method of image evaluation popular in Western European theoretical treatises, the Strehl ratio. This ratio is defined as follows:

$$\text{Strehl ratio} = I = \frac{\text{intensity at the principal maximum of image}}{\text{intensity at the principal maximum of aberration-free image}}$$

and is illustrated in Figure E-3. For a "perfect lens," the Strehl ratio is unity. When the wavefront errors are less than $\lambda/4.45$, the Strehl ratio can be computed from the equation (Ref. 1)

$$I = (1 - 2\pi^2 E/\lambda^2)^2 \qquad (1)$$

where

λ = wavelength of light

E = variance of the wavefront errors

The variance, E, is the statistical term related to the variation of the wavefront from a mean spherical wavefront. By definition,

$$E = \sigma^2 \qquad (2)$$

where σ = standard deviation of the distortions from the mean spherical wavefront. With respect to the magnitudes of the wavefront errors, δ_i, the variance may be expressed in either of the familiar forms

$$E = \overline{(\delta_i^2)} - \overline{(\delta)}^2 \qquad (3)$$

or,

$$E = \frac{1}{N}\sum_i \left[\delta_i^2 - (\bar{\delta})^2\right] \tag{4}$$

where

N = number of distortions.

Based on the Rayleigh Criteria that a gross wavefront error of $\lambda/4$ affects the quality of the image very little, Marechal and Francon (Ref. 2) have derived the criteria for small-scale statistical errors.

$$E \leq \lambda^2/180 \tag{5}$$

If we substitute $\lambda^2/180$ for E in equation (1), a minimum acceptable Strehl ratio of 0.793 is obtained. Note that this tolerance criteria gives a maximum value for the standard deviation (one-sigma) of the wavefront distortions of

$$\sigma = (E)^{1/2} = \lambda/13.4 \tag{6}$$

On this basis, a diffraction-limited mirror must have a surface whose random surface irregularities have a standard deviation of no more than $\lambda/26.8$.

If more than one mirror is used in series in an optical system, better surface accuracies are required. When a wavefront passes through or is reflected from several optical components, the random errors add statistically so that the final wavefront distortion is given by (Ref. 3):

$$E_f = \sigma_f^2 = n\sigma_i^2 \tag{7}$$

$$\sigma_i = (n)^{-1/2}\,\sigma_f \tag{8}$$

where n = number of optical components in series, and σ_i = standard deviation of wavefront error produced by each element. Thus we see that for a two-mirror system, the random wavefront distortion allowable for each mirror is $\lambda/13.4(2)^{1/2} = \lambda/19$, and for a four-mirror system, $\lambda/13.4(2) = \lambda/27$. The random surface error allowable for each mirror is just half of the wavefront distortion allowable. For a two-mirror system, this is $\lambda/38$; and for the

four-mirror system, $\lambda/54$. It should be remembered that these surface tolerance values are for small-scale, random disturbances in the mirror surface. Large-scale random distortions cannot be analyzed by the foregoing mathematics since the statistical terms "standard deviation" and "variance" must deal with fairly large sample numbers to have valid interpretation. The term "large-scale distortions" refers to distortions each of which cover a significant percentage (say, greater than 10%) of the surface area. Naturally, there cannot be a large sample number of such distortions per surface area.

Plots of the Strehl ratio as a function of small-scale surface irregularities are given in Figure E-4 for one-, two-, three-, and four-mirror systems. It has been assumed that the standard deviation of the surface errors are the same for all mirror surfaces in plotting these curves. The Strehl ratio as a function of mirror surface error for systematic (gross) wavefront errors is also plotted for comparison.

In analyzing the effects of gross, systematic wavefront errors such as shown in Figure E-2a, we may make use of the concept of Optical Path difference (OPD) which is the equivalent of the length σ (magnitude of the wavefront error). The OPD is generally specified in terms of fractional wavelengths or in terms of Rayleigh limits. One Rayleigh limit is equal to $\lambda/4$ in OPD. Table E-1 gives the energy distribution of a point image as a function of OPD (Ref. 4).

Table E-1. Energy Distribution as a Function of Optical Path Difference

Optical Path Difference		Percent of Energy In	
Rayleigh limits	Fractional Wavelengths	Central Disc	Rings
0	0	84	16
1/4	$\lambda/16$	83	17
1/2	$\lambda/8$	80	20
1	$\lambda/4$	68	32

For the perfect lens or mirror system (OPD = 0), only 84% of the energy transmitted or reflected is contained in the central (Airy) disc of a point image and the remaining 16% is distributed in the diffraction rings surrounding the central disc. An optical system with OPD = $\lambda/8$ has 80% of the transmitted energy in the central disc. The degradation of this system compared to a perfect lens is 4 parts in 84 parts, or 4.8%. On the other hand, if the OPD is equal to one Rayleigh limit ($\lambda/4$), the degradation is 16 parts in 84, or 19%. The data from the preceding table are plotted in Figure E-5. Also plotted is the degradation as a function of OPD compared to the performance of a perfect lens. The amount of degradation that can be tolerated is a subjective matter. It appears, intuitively, that a 5% degradation should be tolerable on the basis of the fact that it would appear to be essentially imperceptible. Thus, a gross wavefront error of $\lambda/8$ should be tolerable in the image space of an optical system.

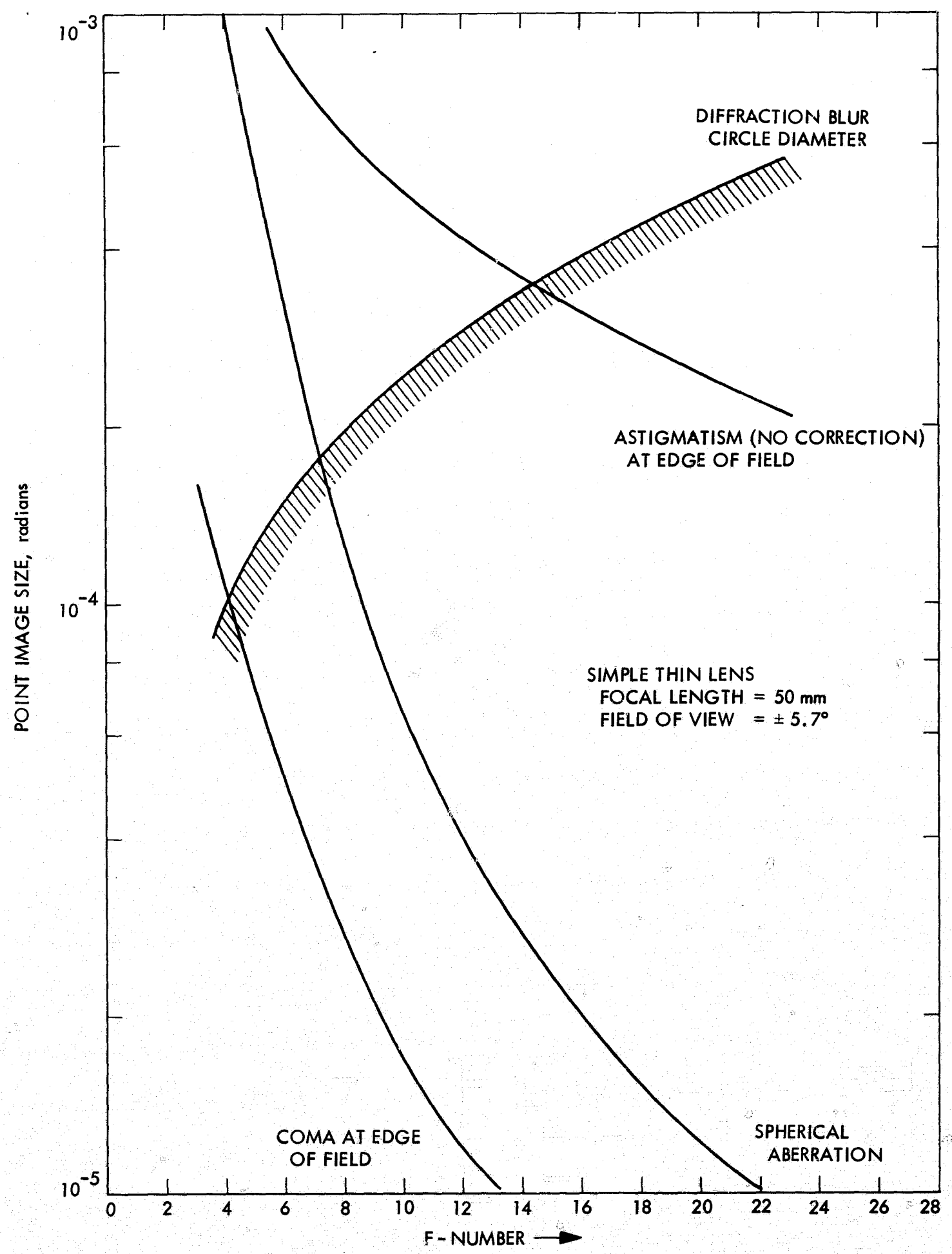

Figure E-1. Aberrations of a Simple Lens

a

GROSS, SYSTEMATIC DISTORTION

b

FINE-SCALE, RANDOM DISTORTIONS

Figure E-2. Wavefront Distortions

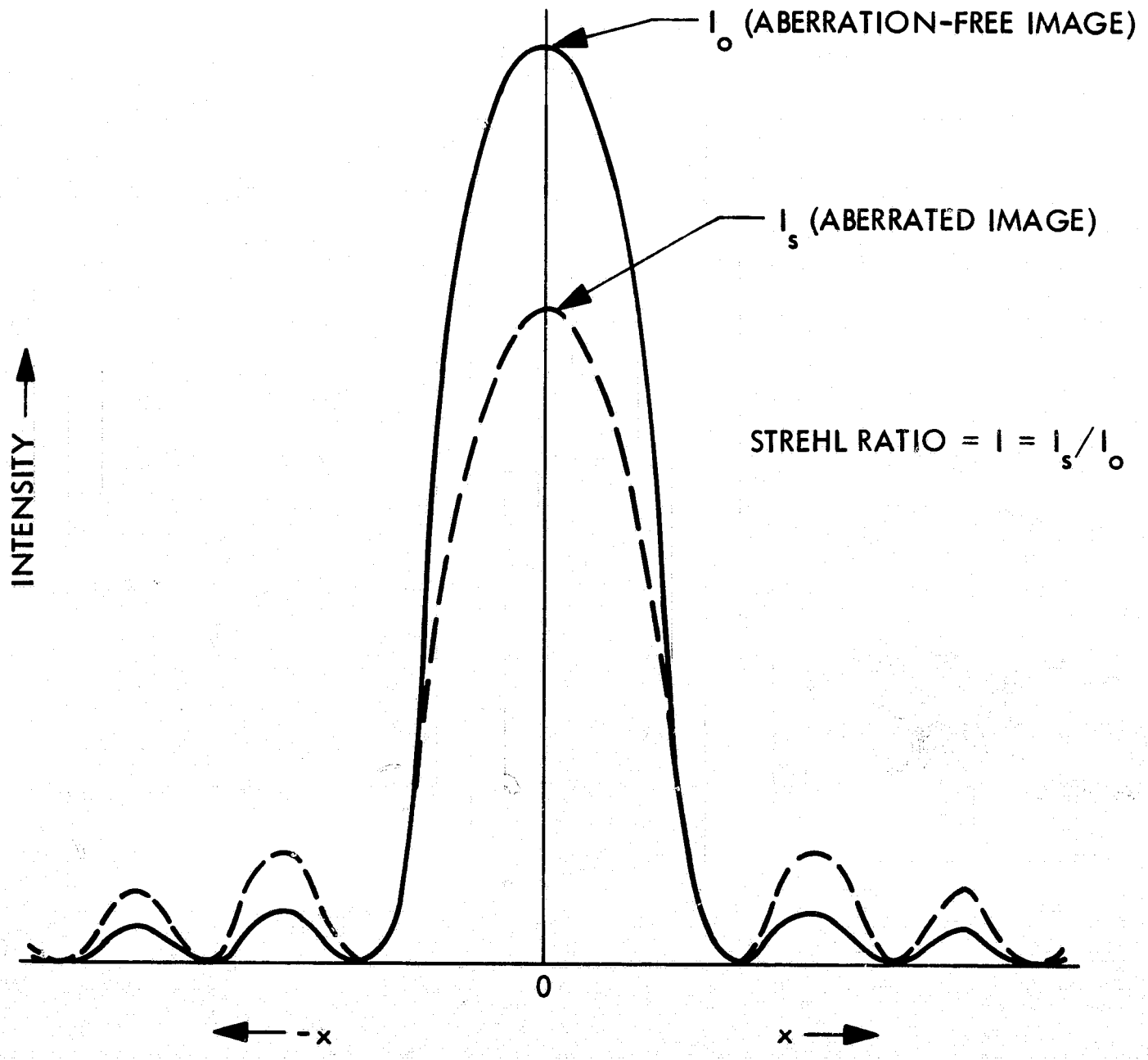

Figure E-3. Strehl Ratio, I

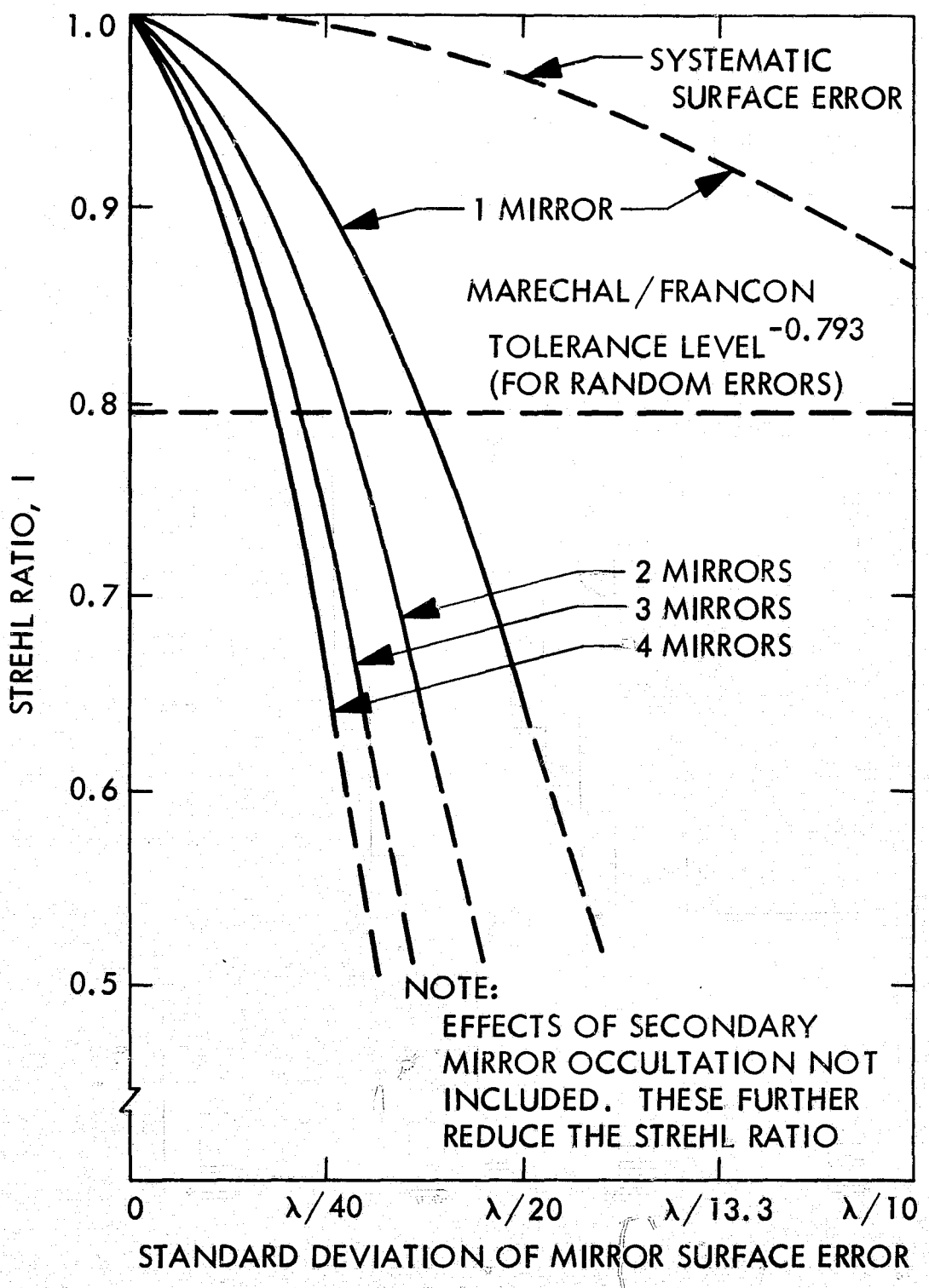

Figure E-4. Strehl Ratio as a Function of Random Small-Scale Surface Irregularities

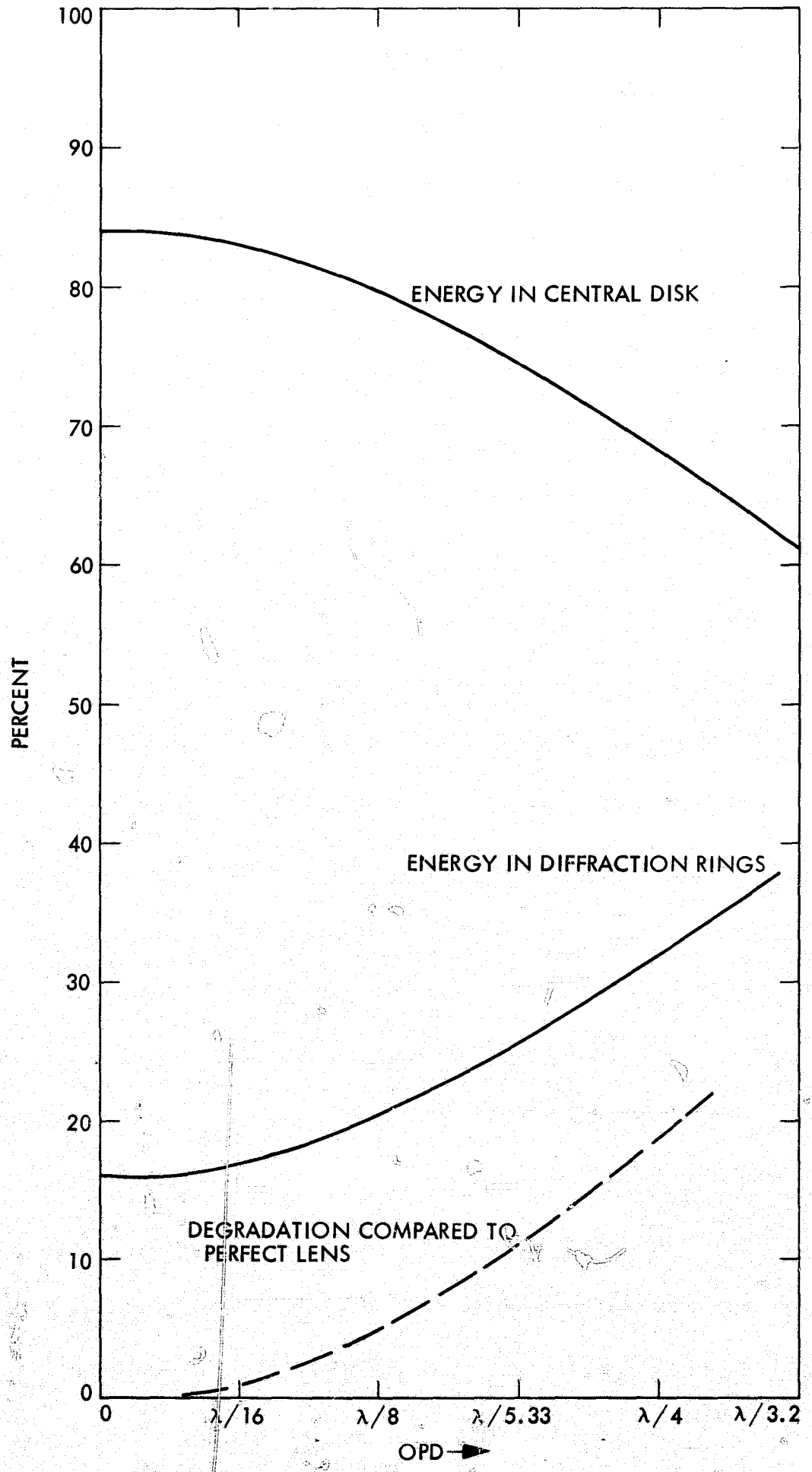

Figure E-5. Energy Distribution in Diffraction Pattern as a Function of OPD

REFERENCES

1. H. H. Hopkins, "The Use of Diffraction-based Criteria of Image Quality in Automatic Optical Design," Optica Acta, 13, 343-369, 1966.

2. A. Marechal and M. Francon, Diffraction, Structure des Images (Editions de le Rev. d'Opt., Paris) 1960, p. 108.

3. E. Bright Wilson, An Introduction to Scientific Research (McGraw-Hill Book Co., New York) 1952, p. 253.

4. Warren J. Smith, Modern Optical Engineering (McGraw-Hill Book Co., New York) 1966, p. 298.